



SKYSURF: Constraints on Zodiacal Light and Extragalactic Background Light through Panchromatic HST All-sky Surface-brightness Measurements. I. Survey Overview and Methods

Rogier A. Windhorst¹, Timothy Carleton¹, Rosalia O'Brien¹, Seth H. Cohen¹, Delondrae Carter¹, Rolf Jansen¹, Scott Tompkins¹, Richard G. Arendt⁹, Sarah Caddy³, Norman Grogin⁴, Anton Koekemoer⁴, John MacKenty⁴, Stefano Casertano⁴, Luke J. M. Davies⁵, Simon P. Driver⁶, Eli Dwek², Alexander Kashlinsky², Scott J. Kenyon⁷, Nathan Miles⁴, Nor Pirzkal⁴, Aaron Robotham⁶, Russell Ryan⁴, Haley Abate¹, Hanga Andras-Letanovszky⁸, Jessica Berkheimer¹, John Chambers¹, Connor Gelb¹, Zak Goisman¹, Daniel Henningsen¹, Isabela Huckabee¹, Darby Kramer¹, Teerthal Patel¹, Rushabh Pawnikar¹, Ewan Pringle¹, Ci'mone Rogers¹, Steven Sherman¹, Andi Swirbul¹, and Kaitlin Webber¹

¹ School of Earth and Space Exploration, Arizona State University, Tempe, AZ 85287-1404, USA; Rogier.Windhorst@asu.edu

² NASA Goddard Space Flight Center, Greenbelt, MD 21771, USA

³ Macquarie University, Sydney, NSW 2109, Australia

⁴ Space Telescope Science Institute, 3700 San Martin Drive, Baltimore, MD 21210, USA

⁵ The University of Western Australia, M468, 35 Stirling Highway, Crawley, WA 6009, Australia

⁶ International Centre for Radio Astronomy Research (ICRAR) and the International Space Centre (ISC), The University of Western Australia, M468, 35 Stirling Highway, Crawley, WA 6009, Australia

⁷ Smithsonian Astrophysical Observatory, 60 Garden Street, Cambridge, MA 02138, USA

⁸ Steward Observatory, University of Arizona, Tucson, AZ 85721-0065, USA

⁹ UMBC/CRESST2, NASA Goddard Space Flight Center, Greenbelt, MD 21771, USA

Received 2022 May 13; revised 2022 July 2; accepted 2022 July 18; published 2022 September 15

Abstract

We give an overview and describe the rationale, methods, and testing of the Hubble Space Telescope (HST) Archival Legacy project “SKYSURF.” SKYSURF uses HST’s unique capability as an absolute photometer to measure the $\sim 0.2\text{--}1.7\ \mu\text{m}$ sky-surface brightness (sky-SB) from 249,861 WFPC2, ACS, and WFC3 exposures in ~ 1400 independent HST fields. SKYSURF’s panchromatic data set is designed to constrain the discrete and diffuse UV to near-IR sky components: Zodiacal Light (ZL), Kuiper Belt Objects (KBOs), Diffuse Galactic Light (DGL), and the discrete plus diffuse Extragalactic Background Light (EBL). We outline SKYSURF’s methods to: (1) measure sky-SB levels between detected objects; (2) measure the discrete EBL, most of which comes from $AB \approx 17\text{--}22$ mag galaxies; and (3) estimate how much truly diffuse light may exist. Simulations of HST WFC3/IR images with known sky values and gradients, realistic cosmic ray (CR) distributions, and star plus galaxy counts were processed with nine different algorithms to measure the “Lowest Estimated Sky-SB” (LES) in each image between the discrete objects. The best algorithms recover the LES values within 0.2% when there are no image gradients, and within 0.2%–0.4% when there are 5%–10% gradients. We provide a proof of concept of our methods from the WFC3/IR F125W images, where any residual diffuse light that HST sees in excess of zodiacal model predictions does *not* depend on the total object flux that each image contains. This enables us to present our first SKYSURF results on diffuse light in Carleton et al.

Unified Astronomy Thesaurus concepts: [Hubble Space Telescope \(761\)](#); [zodiacal cloud \(1845\)](#); [Cosmic background radiation \(317\)](#); [Galaxy counts \(588\)](#); [Star counts \(1568\)](#)

1. Introduction

The Hubble Space Telescope (HST) was designed in the 1960 s and 1970 s to observe very faint objects at UV to near-IR wavelengths above the Earth’s atmosphere (e.g., Smith et al. 1993). HST’s ability to observe outside the Earth’s atmosphere has resulted in very significant gains over ground-based telescopes in four main areas, namely the ability to: (1) observe in the vacuum ultraviolet; (2) observe with very stable, repeatable, and narrow Point-Spread Functions (PSFs); (3) observe against very dark foregrounds and backgrounds; and (4) perform precision point-source photometry at (very) high time resolution. As a consequence, HST also has the unique ability to accurately measure the surface brightness of foregrounds or backgrounds on

timescales of decades. It is precisely this rather unused capability of HST that project “SKYSURF” will focus on in this paper: measuring the sky-surface brightness (sky-SB) in all eligible HST Archival images and analyzing the results to constrain astronomical foregrounds or backgrounds.

As of 2022 April 24, HST has been in orbit for over 32 yr. After successful correction of the spherical aberration in its primary mirror in 1993 December, HST has produced an unprecedented wealth of high-quality data that have fundamentally changed our understanding of the universe. The HST Archive¹⁰ presently contains more than 1.5 million exposures from both its imagers and spectrographs. By design, HST studies frequently targeted faint stars or faint galaxies, but HST has also produced very dramatic results on, e.g., planetary and solar system objects, exoplanets around nearby stars, Galactic star formation regions, nearby galaxies, massive black holes in

galaxies, and distant quasars. Of particular relevance for project SKYSURF are HST’s most-used wide field-of-view (FOV) cameras: the Advanced Camera for Surveys/Wide Field Channel (ACS/WFC), Wide Field Planetary Camera 2 (WFPC2), and Wide Field Camera 3 (WFC3/UVIS and WFC3/IR).

During the early days of HST before and just after the first Space Shuttle Servicing Mission (SM1), and before the Hubble Deep Field (HDF) project (Williams et al. 1996), HST images were not dithered at the subpixel level (e.g., Windhorst et al. 1992, 1994b), because at that time it was not clear that deliberate image offsets could be done with the required subpixel accuracy. With the introduction of the deep HDF imaging data set (Williams et al. 1996), it was shown that subpixel accuracy dithering could, in fact, be done, and indeed resulted in much better-sampled image PSFs and correspondingly increased image depth over the zodiacal foreground compared to nondithered images (see, e.g., Driver et al. 1995; Odewahn et al. 1996; Windhorst et al. 1998). Since 1995, a properly dithered HST imaging data set in a given filter has been traditionally processed using “drizzling” techniques, as described by, e.g., Fruchter & Hook (2002), Lauer (1999), Koekemoer et al. (2011), Grogin et al. (2011), and Koekemoer et al. (2013).

Since 1995, the standard HST drizzling process traditionally removed the sky-foreground levels by subtracting a surface fit to the image with the discrete objects masked out, hence setting the image sky-SB values to zero. While the original and subtracted sky-SB value may have been preserved in the reduced image FITS headers, the image sky values are often not kept in the subsequent data products, nor is the information about sky-SB gradients that were removed from the images during the drizzling process. Most HST users have thus subtracted their image sky-SB values since 1995. This mode of operation is, in general, not an issue, and in fact, it is the desired way of proceeding, because the vast majority of HST targets have been point sources or nearly point-like sources, and the users’ intended interest has usually been the (almost point-like) faint object flux at certain wavelengths over the local sky foreground. Hence, removing the sky-SB and its gradient during the drizzling process has been, for almost all purposes, a necessary step. However, for SKYSURF, we need to *precisely preserve and measure* the sky-SB in all eligible HST images on timescales of decades, which we describe below. This paper will therefore summarize the diffuse astronomical foregrounds and backgrounds that one may expect in the HST images (Section 2), as well as the instrumental foregrounds that need to be identified, subtracted, or discarded (see Sections 3–4 and Carleton et al. 2022a, referred to as SKYSURF–2 throughout), before these astronomical foregrounds and backgrounds can be assessed.

Many of the procedures and methods in this paper are by necessity *nonconventional*, even after 32 yr of Hubble Space Telescope use, as explained above. SKYSURF will reprocess most of the HST images acquired since 1994 on servers provided by Amazon Web Services (AWS). As a result, we simply cannot plan to repeat this process many times. Hence, the focus of this first SKYSURF overview paper is to publish our survey rationale and methods early. This will allow the community to comment on our methods as early as possible and give our SKYSURF team the opportunity to improve upon those methods before they are all executed on AWS.

Our paper is organized as shown in the Table of Contents, where the (sub-)section headings list all the steps needed to justify (Section 2), define and organize (Section 3), and calibrate and reprocess (Section 4.1) the SKYSURF database, with close attention to systematics that may affect the sky-SB levels in HST images (Sections 4.1.1–4.8). This includes methods that are anchored in simulations to measure the object-free sky-SB, a sky-SB preserving implementation of the drizzle algorithm, the flagging of images with orbital stray light, and our methods to do star–galaxy separation and make panchromatic discrete object catalogs. We discuss our findings in Section 5 and summarize our conclusions in Section 6. Appendices give details on the HST orbital parameters and stray light (A), the specific requirements for SKYSURF’s image drizzling and removal of images with artifacts or large extended objects (B), and SKYSURF’s procedures to make object catalogs and perform star–galaxy separation and Galactic extinction corrections (C). In SKYSURF–2, we estimate the sky-SB in all individual WFC3/IR exposures in the F125W, F140W, and F160W filters, make corrections for the WFC3/IR thermal dark signal, present our first constraints on diffuse light at 1.25–1.6 μm , and summarize our main results thus far.

The various astronomical foregrounds and backgrounds that exist in the SKYSURF images are discussed in more detail in Section 2. They form the core reason for carrying out the SKYSURF project. In summary, they are the following. The Zodiacal Light (ZL) is the main foreground in most HST images, and SKYSURF will measure it in Section 4.2, and model it in SKYSURF–2 as well as possible with the available tools. All stars in our galaxy (except the Sun) and all other galaxies are beyond the InterPlanetary Dust Cloud, so the ZL is thus always referred to as a “foreground.” The Diffuse Galactic Light is caused by scattered starlight in our galaxy, and can be a background (to nearby stars) or a foreground (to more distant stars and all external galaxies; see Appendix C.2). Most objects in an average moderately deep (AB \lesssim 25–26 mag) HST image are faint galaxies close to the peak in the cosmic star formation history at $z \lesssim 2$ (e.g., Madau & Dickinson 2014). Most of the Extragalactic Background Light (EBL) therefore comes from distant galaxies and AGN (Sections 2.3, 4.7, and SKYSURF–2), and is thus referred to as a “background.” Before SKYSURF can quantify and model these astronomical foregrounds and backgrounds, it needs to address the main contaminants, which are residual detector systematics (Section 4.1), orbital phase-dependent stray light from the Earth, Sun, and/or Moon (Section 4.3), and the WFC3/IR thermal dark signal SKYSURF–2.

Throughout this work, we use Planck cosmology (Planck Collaboration et al. 2016): $H_0 = 66.9 \pm 0.9 \text{ km s}^{-1} \text{ Mpc}^{-1}$, matter density parameter $\Omega_m = 0.32 \pm 0.03$, and vacuum energy density $\Omega_\Lambda = 0.68 \pm 0.03$, resulting in a Hubble time of 13.8 Gyr. When quoting magnitudes, our fluxes are all in AB-magnitudes (hereafter AB-mag), and our surface brightness (SB) values are in AB-mag arcsec $^{-2}$ (Oke & Gunn 1983) or MJy sr $^{-1}$, using flux densities $F_\nu = 10^{-0.40(\text{AB}-8.90 \text{ mag})}$ in Jy. Sky-SB values can be converted to units of nW m $^{-2}$ sr $^{-1}$ by multiplying the MJy sr $^{-1}$ units by $10^{-11}(c/\lambda_c)$, where λ_c is the filter central wavelength. Further details on the flux density scales used are given in Figure 1 and Section 4.1.5.

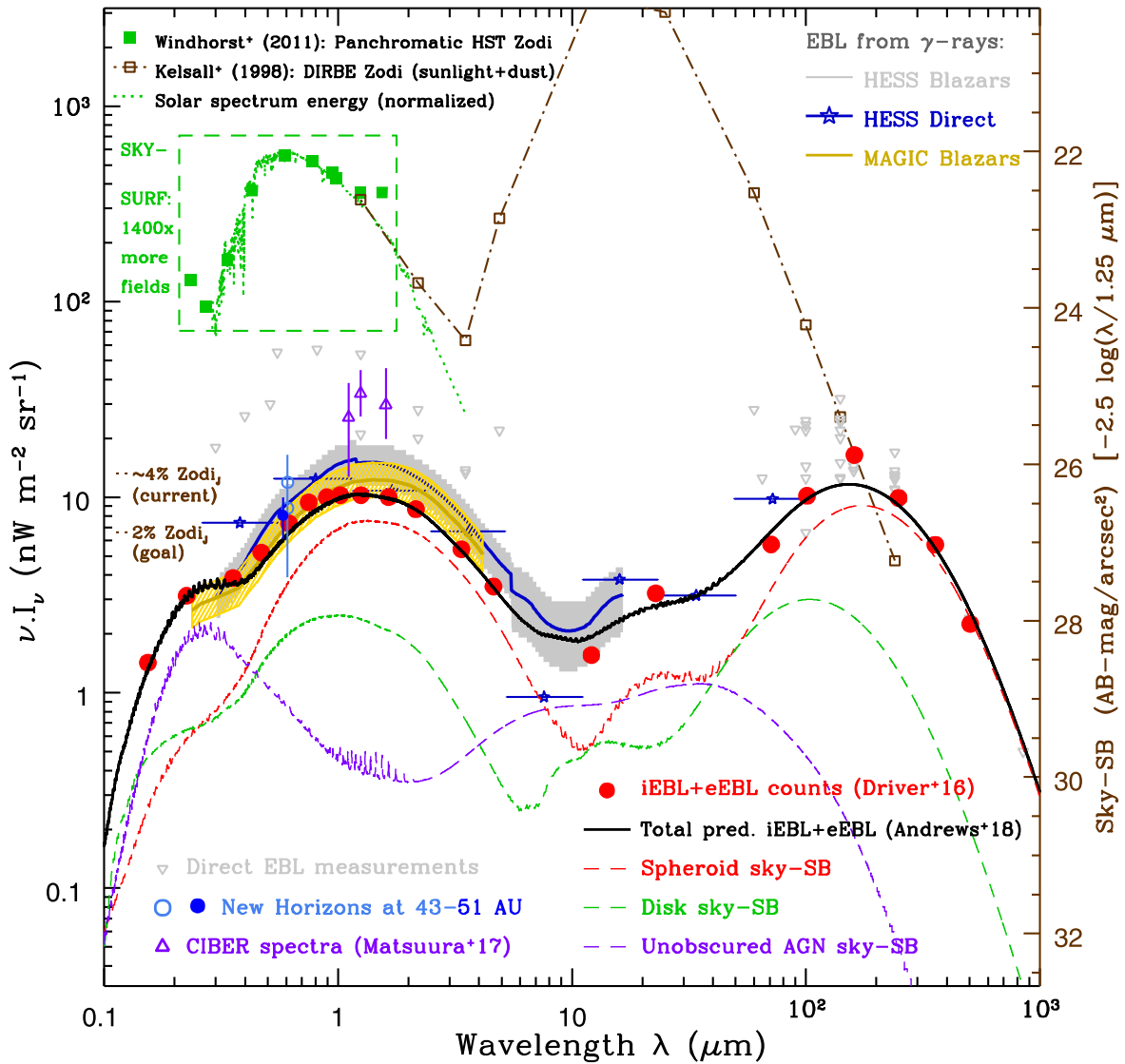


Figure 1. Summary of astrophysical foreground and background energy relevant to SKYSURF. The left scale indicates the total energy νI_ν in $\text{nW m}^{-2} \text{sr}^{-1}$, and the right scale the corresponding sky-SB in $\text{AB-mag arcsec}^{-2}$ at $1.25 \mu\text{m}$ (which can be scaled to other wavelengths as indicated). The discrete measurements of D16 from integrated and extrapolated galaxy counts (iEBL+eEBL; red-filled circles) and other published data are shown (Section 2). Gray triangles indicate total EBL measurements that require accurate modeling of DGL and ZL, and are $\sim 3\text{--}5\times$ higher than the discrete iEBL+eEBL, leaving room for a substantial *diffuse light component*. Green squares are panchromatic HST sky-SB measurements compared to the Solar spectrum. (The 0.23 and $1.6 \mu\text{m}$ filters shown did not get LOW-SKY; see Sections 2 and 4.3). Brown squares indicate the COBE/DIRBE data and the zodiacal dust model of Kelsall et al. (1998). The gray and orange wedges and blue stars are γ -ray blazar EBL constraints from the HESS and MAGIC TeV experiments. The black line is the sum of the Andrews et al. (2018) EBL models for star formation in spheroids (red), disks (green), and unobscured AGN (purple). The purple triangles are the Matsuura et al. (2017) CIBER spectral 1.1 and $1.6 \mu\text{m}$ estimates of diffuse light in excess of the Kelsall et al. (1998) model prediction, as well as the Sano et al. (2020) $1.25 \mu\text{m}$ estimate, where the iEBL+eEBL has also been subtracted. The light and dark blue circles with error bars at $0.608 \mu\text{m}$ are the Lauer et al. (2021, 2022) diffuse light estimates obtained via New Horizons at $43\text{--}51 \text{ au}$. SKYSURF’s currently achieved calibration+zero-point accuracy in the $1.25\text{--}1.6 \mu\text{m}$ HST sky-SB estimates is $\lesssim 4\%$ of the zodiacal sky-SB (Table 5), as indicated. Our goal is a $\sim 2\%$ accurate sky-SB model across the sky at $0.2\text{--}1.7 \mu\text{m}$ wavelengths, to address the discrepancy between the total EBL and the *discrete* iEBL+eEBL. In SKYSURF-2, we discuss SKYSURF’s resulting upper limits for the *diffuse light* in detail.

2. SKYSURF Goals in the Context of Astronomical Foregrounds and Backgrounds

For the sake of clarity, we will make a distinction between *diffuse foregrounds* and *diffuse backgrounds*. In the following subsections and SKYSURF-2, we define and summarize the physical phenomena from which these diffuse foregrounds and backgrounds arise, as they form the core of the SKYSURF project. SKYSURF has two main science goals:

- (1) *SKYSURF-SB*: Measure the panchromatic HST ACS, WFPC2, and WFC3 sky-SB—free of discrete object flux—across the celestial sphere, and derive the best possible constraints for the Zodiacal Light (ZL), Diffuse Galactic Light (DGL), and the Extragalactic Background Light (EBL); and
- (2) *SKYSURF-Sources*: Measure the panchromatic integrated background from *discrete object catalogs* (Galactic stars, galaxies) across the sky, and derive independent measurements over $\gtrsim 1400$ representative HST fields far enough apart in the

sky to average over the effects of cosmic variance more accurately than existing HST surveys alone can do.

2.1. The UV–Near-IR Zodiacal Foreground

Much of the area surveyed with HST cameras consists of relatively empty sky surrounding targets of interest for which the observations were made. At wavelengths of 0.6–1.25 μm , over 95% of the photons in the HST Archive come from the ZL in the InterPlanetary Dust (IPD) cloud, i.e., from distances less than 5 au. This fraction is illustrated by the ratio of a typical ZL spectrum (green squares and green dotted line in Figure 1) to the *discrete* EBL integral (red circles plus black model in Figure 1; see also Section 2.3). These photons are precisely the sky-SB photons present in nearly all HST images between the discrete objects that are of interest to our SKYSURF study. These sky photons come primarily from the ZL foreground, which is caused by sunlight scattered by dust and small particles in the IPD at distances $r \lesssim 3\text{--}5$ au, or from even closer light sources such as earthshine or geocoronal emission, scattered light in the Optical Telescope Assembly (OTA) or thermal foregrounds in the camera detectors, as discussed in Section 4 and SKYSURF–2. Constraints on ZL are obtainable from the HST Archive, yet no precise all-sky panchromatic measurements of the HST sky-SB exist. Ground-based telescopes are *unable* to make absolute measurements of the ZL, due to atmospheric absorption, OH lines, air glow, and light pollution, unless very special measures are taken (e.g., Leinert et al. 1998; Bernstein et al. 2002). Located above the Earth’s atmosphere, HST thus has the unique and rather unexplored capability to serve as an *absolute photometer* for low surface brightness foreground and background measurements in the 0.2–1.7 μm range on timescales of decades.

2.2. Discrete HST Objects: Stars and Galaxies

Other than planetary and other moving targets, the main science interest in HST images has, in general, been stellar objects and galaxies from the brightest observable stars and star-forming (SF) regions in our own galaxy and nearby galaxies to the faintest galaxies visible in the deepest HST images, such as the Hubble UltraDeep Field (HUDF; see, e.g., Beckwith et al. 2006). Stellar objects here will include Quasi-Stellar Objects (QSOs) or (weak) Active Galactic Nuclei (AGN). By selection, the large majority of objects observed in the HST Archive are nearly point-like objects. This is, of course, because HST was designed to observe faint objects at UV to red or near-IR wavelengths outside the Earth’s atmosphere (Section 1), and faint objects tend to be compact (the effects of SB selection on the HST catalog completeness are discussed in Section 4.7; see also Windhorst et al. 2008, 2021).

To date, the Hubble Legacy Archive (HLA)¹¹ contains over 1.5 million HST observations, and the Hubble Source Catalog (HSC)¹² contains at least 3.7 million objects. Following the detailed description of Budavári & Lubow (2012) and Whitmore et al. (2016), the HLC Version 1 object catalogs are derived from subsets of the WFPC2, ACS/WFC, WFC3/UVIS, and WFC3/IR `SourceExtractor` source lists from the HLA data release version 10 (DR10). This process

incorporates cross-matching and relative astrometry of overlapping images, to minimize offsets between closely aligned sources in different images. After correction for such offsets, the astrometric residuals of cross-matched sources are significantly reduced, with median errors less than 8 m.a.s. The absolute astrometry of the HLA is anchored into Gaia DR1, Pan-STARRS, the Sloan Digital Sky Survey (SDSS), and 2MASS.

The HLA and HLC are an outstanding permanent legacy of HST’s 30⁺ yr record. SKYSURF’s main goal is not to replicate the extensive work that the HLA and HLC have done to create its object catalogs. Instead, SKYSURF focuses on the 249,861 ACS/WFC, WFPC2, WFC3/UVIS, and IR images that are, in principle, suitable for SKYSURF’s main sky-SB science goals, as discussed in Sections 2.5–4. Of these images, 220,657 have exposure times $t_{\text{exp}} \geq 200$ s and are also eligible for drizzling, panchromatic object catalogs, and object counts, as discussed in Sections 4.5–4.6 and Appendices B–C. Using the WFC3/IR F125W filter as the fiducial wavelength in this paper, two aspects are essential for SKYSURF:

(1) The Galactic star counts have very flat slopes, while the galaxy counts have much steeper count slopes, and they cross over with about equal surface densities at average Galactic latitudes around $AB \simeq 18$ mag at 1.25 μm (e.g., Windhorst et al. 2011; see also our Section 4.7 and figures therein).

(2) The galaxy counts change from nonconverging to converging slopes in the range $17 \lesssim AB \lesssim 22$ mag with only a mild dependence on wavelength (Windhorst et al. 2011; Driver et al. 2016a). Therefore, while the vast majority of objects detected in HST images of average ($\lesssim 1\text{--}2$ orbits) depth are moderately faint ($AB \lesssim 26$ mag) galaxies, most of the *total energy* emitted by discrete objects at UV–optical–near-IR wavelengths is produced by those galaxies already detected in *single-exposure* HST images (Driver et al. 2016a, Sections 2.3 and 4.7 here).

The consequences of these two facts for SKYSURF are rather profound: to accurately measure both the integrated discrete galaxy counts *and* the sky-SB from all SKYSURF images, we must have: (a) very accurate star–galaxy separation procedures, especially at brighter fluxes ($AB \lesssim 18$ mag) where stars dominate the object counts; and (b) very accurate procedures to grow the light profiles of all detectable stars and galaxies, especially those with $17 \lesssim AB \lesssim 22$ mag, where most of the EBL is produced, *and* remove their discrete object light from the images before the best estimates of the ZL and EBL can be made. Hence, SKYSURF must measure and account for the light from all discrete objects from 220,657 HST images in a manner that differs from that adopted for the HLA/HSC, as described below. For this, we will use the star–galaxy separation methods of Windhorst et al. (2011), which on shallow HST images are generally robust to $AB \lesssim 25\text{--}26$ mag (Section 4.7).

2.3. Integrated and Extrapolated Extragalactic Background Light from Discrete Objects (iEBL+eEBL)

The Extragalactic Background Light is defined as the flux received from all sources of photon production since recombination at far-UV ($\lambda \gtrsim 0.1$ μm) to far-IR ($\lambda \lesssim 1000$ μm) wavelengths (e.g., McVittie & Wyatt 1959; Partridge & Peebles 1967a, 1967b; Hauser & Dwek 2001; Kashlinsky 2005; Lagache et al. 2005; Finke et al. 2010; Domínguez et al. 2011; Dwek & Krennrich 2013; Khaire & Srianand 2015; Driver et al. 2016a;

¹¹ <http://hla.stsci.edu>

¹² <http://archive.stsci.edu/hst/hsc/>

Koushan et al. 2021; Saldana-Lopez et al. 2021). That is, the EBL reflects the energy production of the universe from $z \simeq 1090$ until today and consists mainly of light from stars, AGN, and reprocessed light from dust, with some contribution from material heated by accretion (e.g., Alexander et al. 2005; Jauzac et al. 2011; Andrews et al. 2018). The EBL observed today thus results from the cosmic star formation history, AGN activity (i.e., accretion onto supermassive black holes), and the evolution of cosmic dust over the past ~ 13.5 billion years. The EBL can be divided into two roughly equal components: one covering the UV–near-IR (0.1–8 μm ; the Cosmic Optical Background, or COB) and one covering the mid–far-IR (8–1000 μm ; the Cosmic Infrared Background, or CIB; Dwek et al. 1998; Kashlinsky & Odenwald 2000; Andrews et al. 2018; Figure 1 here).

With the advent of space-based and ground-based facilities, deep fields have been obtained across the entire far-UV to far-IR wavelength range. For instance, Driver et al. (2016a) and Koushan et al. (2021) combined recent wide and deep panchromatic galaxy counts from the Galaxy And Mass Assembly survey (GAMA; Driver et al. 2011; Hopkins et al. 2013; Liske et al. 2015; Driver et al. 2016b), COSMOS/G10 (Davies et al. 2015; Andrews et al. 2017), the HST Early Release Science field (ERS; Windhorst et al. 2011), and Ultra-Violet Ultra-Deep Fields (UVUDF; Teplitz et al. 2013; Rafelski et al. 2015), plus near-, mid-, and far-IR data sets from ESO, Spitzer, and Herschel. To estimate the EBL from discrete objects, great care was taken in each data set to produce object catalogs, total fluxes, and object counts across a broad wavelength range.

Figure 2 gives an example of this process as relevant for the current SKYSURF analysis. Figure 2(a) shows the galaxy counts in the J -band or F125W filter from the above data sets. Figure 2(b) shows these galaxy counts *normalized* to the converging magnitude slope of $\gamma = 0.40$ (Driver et al. 2016a), which yields the EBL energy contribution $\rho_f \delta m$ from each 0.5 mag-wide flux interval. Earlier examples of the integrated galaxy counts and the resulting EBL are given by, e.g., Madau & Pozzetti (2000), Hopwood et al. (2010), Xu et al. (2005), Totani et al. (2001), Dole et al. (2006), Keenan et al. (2010), Berta et al. (2011), and Béthermin et al. (2012), as summarized in Driver et al. (2016a) and Koushan et al. (2021). The galaxy contribution to the integrated light is bounded because the faint galaxy count slope falls well below the critical value for convergence (i.e., $\gamma = \delta \log N / \delta m < 0.4$).

This *integral* over the discrete galaxy counts converging down to the detection limit is referred to as the “iEBL,” and the *extrapolated* converging integral of the discrete galaxy counts beyond the detection limit as the “eEBL” (Figure 2bd). The *discrete* EBL is defined as the sum of the iEBL and eEBL, which is indicated by the red-filled circles in Figure 1. The *discrete* EBL is distinct from the *diffuse* EBL, which is defined in Section 2.4.

Driver et al. (2016a) and Koushan et al. (2021) used Monte Carlo spline fits to extrapolate the observed discrete galaxy counts to beyond the detection limits of the deepest available images, which provided a range in allowed extrapolated slopes and corresponding uncertainties in the resulting eEBL. These simulations are consistent with the range in faint-end power-law slopes of the galaxy luminosity function over the relevant redshift range (e.g., Ilbert et al. 2005; Hathi et al. 2010; Windhorst et al. 2021), and result in eEBL integrals that, in general, converge very quickly for $AB \gtrsim 26$ mag (Figure 2(b)).

The integrated discrete iEBL as extrapolated with the eEBL in Figure 2(d) is thus an estimate of the *discrete* EBL that comes from galaxies. In Section 4.7, we will correct the discrete eEBL for the fraction of fainter objects *known* to exist in deeper HST images that are missing due to SB-incompleteness effects in the shallower SKYSURF images. Figure 1 also shows the three-component EBL model prediction of Andrews et al. (2018) that links spheroid formation dominating at high redshift to later disk formation and (unobscured) AGN, as well as reprocessing of UV photons by dust. The model predictions of, e.g., Cowley et al. (2019) match these iEBL+eEBL measurements.

Figure 2(d) shows that the *brightest* 25% of the discrete iEBL comes from galaxies brighter than $J_{AB} \simeq 17.36$ mag, while the *faintest* 25% is due to galaxies fainter than $J_{AB} \simeq 22.01$ mag. The interquartile range of $17.36 \lesssim J_{AB} \lesssim 22.01$ mag—indicated by the blue boxes in Figures 2(a)–(b), and by the corresponding blue wedges in the figures of Section 4.7—accounts for the *middle* 50% of the discrete J -band iEBL and is due to galaxies with a median redshift $z \lesssim 1$. Thus, most of the discrete iEBL flux comes from moderately faint galaxies already detected in short SKYSURF exposures at $AB \lesssim 26$ mag, where the change in count slope occurs at all UV–optical–near-IR wavelengths.

2.4. Diffuse Extragalactic Background Light (dEBL)

The total EBL is defined as the sum of the integrated and extrapolated discrete EBL of Section 2.3 and any *diffuse* EBL component that may exist:

$$\text{Total EBL} = (\text{iEBL} + \text{eEBL}) + \text{dEBL} \equiv \text{eIGL} + \text{dEBL} \quad (1)$$

Figure 1 compares the *discrete* EBL (iEBL+eEBL) of Driver et al. (2016b), which they define as “eIGL,” from the far-UV to the far-IR to various *total* EBL estimates or upper limits as reviewed by Dwek & Krennrich (2013) and Ashby et al. (2015). Many of these methods estimate the total EBL directly; these direct estimates are plotted as gray triangles (e.g., Puget et al. 1996; Dwek & Arendt 1998; Fixsen et al. 1998; Hauser et al. 1998; Lagache et al. 1999; Cambrésy et al. 2001; Bernstein et al. 2002; Matsumoto et al. 2005; Dole et al. 2006; Bernstein 2007; Matsumoto et al. 2011). More recent work that constrained the absolute EBL level can be found in, e.g., Matsuura et al. (2011) for the far-IR CIB through AKARI measurements, in Tsumura et al. (2013), Matsuura et al. (2017), and Sano et al. (2020) for NIREBL constraints, and in Kawara et al. (2017) and Mattila et al. (2017) for optical EBL constraints. Figure 1 also shows the New Horizons constraints on diffuse light observed at ~ 4.7 –51 au from the Sun (Zemcov et al. 2017; Lauer et al. 2021, 2022), where the ZL contribution is much smaller.

In the far-IR, the discrete EBL agrees fairly well with the directly measured CIB (Béthermin et al. 2012; Magnelli et al. 2013), but Figure 1 shows a significant optical–near-IR discrepancy between the iEBL+eEBL data (red-filled circles) and the total EBL estimates (gray triangles). This difference amounts to as much as a factor of ~ 3 –5, and is often attributed to a possible component of *diffuse* Extragalactic Background Light (dEBL). We note that earlier groups plotted the *total* EBL signal (i.e., before the iEBL+eEBL was subtracted) in figures like Figure 1, while more recent work *did* subtract the iEBL +eEBL from their data, either by modeling and subtracting it

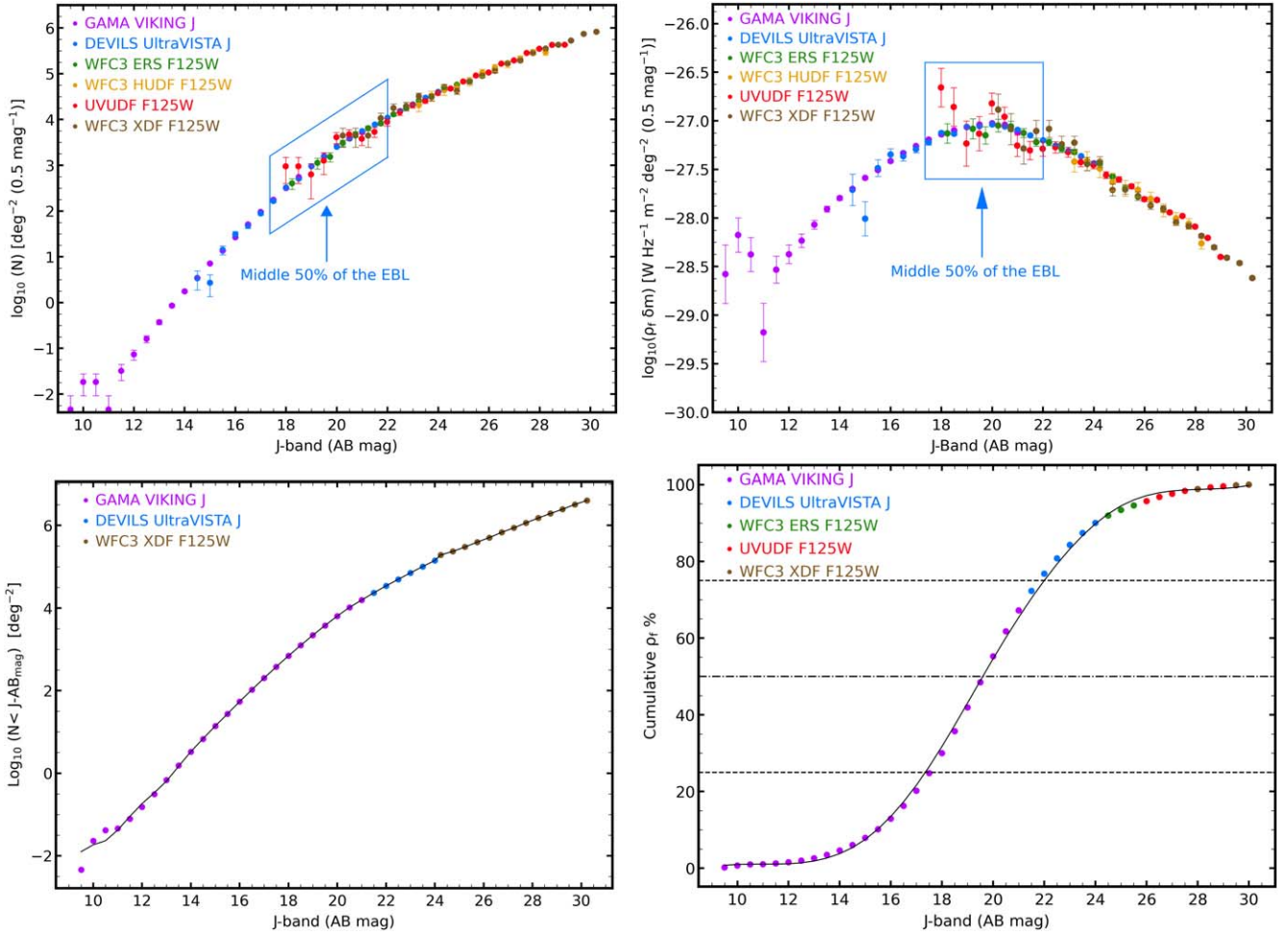


Figure 2. (a) Top Left: differential galaxy counts in the J -band or WFC3/IR F125W filter. Combined ground-based + HST-surveys cover $10 \lesssim AB \lesssim 30$ mag (Driver et al. 2016a). The galaxy counts start to reach a converging slope ($\gamma < 0.40$) over the general flux range of $AB \gtrsim 17$ –22 mag, and over a similar magnitude interval for the other filters between 0.2 and 1.7 μm (Windhorst et al. 2011). (b) Top Right: differential J -band counts of panel (a) normalized to the $\gamma = 0.40$ slope, yielding the EBL energy contribution $\rho_f \delta m$ from each 0.5 mag-wide flux interval in units of $\text{W}/\text{Hz}/\text{m}^2/\text{deg}^2$. The converging sky integral constitutes the integrated iEBL. Cosmic Variance (CV) inside a single HST WFC3/IR FOV can be $\gtrsim 30\%$. SKYSURF will average the panchromatic galaxy counts over ~ 1400 usable independent HST fields, reducing CV errors in the iEBL to $\sim 3\%$ (Section 2.5.2). (c) Bottom Left: integral galaxy counts in the J -band filter, obtained by integrating panel (a). The integral galaxy counts are used to calculate the natural confusion limit that partially limits catalog completeness in Figure 10, as discussed in Section 4.7. (d) Bottom Right: integrated 1.25 μm EBL contribution from panel (b). The black curves in panels (c) and (d) indicate cubic polynomial fits. The *brightest* 25% of the discrete EBL level is reached at $J_{AB} \lesssim 17.36$ mag, while the *middle 50%* of the EBL level peaks at $J_{AB} = 19.60$ mag, and the *faintest* 25% of the EBL level occurs at $J_{AB} \gtrsim 22.01$ mag. The interquartile range or middle 50% of the discrete J -band EBL thus comes from galaxies as bright as $17.36 \lesssim J_{AB} \lesssim 22.01$ mag, which have a median redshift $z \lesssim 1$. The interquartile range is indicated by the blue boxes in panel (a)–(b), and by the corresponding blue wedges in Figures 10–11.

directly (e.g., Lauer et al. 2021, 2022) or by using CIBER spectra including the Ca-triplet to estimate and subtracting the zodiacal foreground (e.g., Matsuura et al. 2017; Korngut et al. 2022). Hence, their Zodi+iEBL+eEBL subtracted diffuse light values have been plotted in Figure 1. Our HST SKYSURF analysis in Sections 3–4 already automatically subtracts from the diffuse light signal: a) almost all the starlight, and b) $\gtrsim 95\%$ of the *discrete* EBL integral from objects detected in the HST images with $AB \lesssim 26.5$ mag; and c) estimates and subtracts the undetected eEBL integral for $AB \gtrsim 26.5$ mag, which is $\lesssim 5\%$ of the total *discrete* EBL in Carleton et al. (2022a). Hence, our SKYSURF results will be directly comparable to these most recent results. We return to this point in Section 5.

HESS/MAGIC γ -ray blazar studies (e.g., Dwek & Krennrich 2013; H.E.S.S. Collaboration et al. 2013; Biteau & Williams 2015; Lorentz et al. 2015; Fermi-LAT Collaboration et al. 2018; gray and orange wedges in Figure 1) provide independent constraints to the total EBL from deviations of the blazar TeV spectra from a power law, which is explained by

pair production involving γ -ray and EBL photons. Desai et al. (2019) and the HAWC Collaboration (2022) similarly find low numbers based on GeV–TeV from Fermi-LAT and HAWC, respectively. Hence, γ -ray blazar studies would imply a lower level of dEBL than these direct studies that constrain the total EBL.

Direct estimates of the true level of dEBL rely on a robust subtraction of three other sources of light: ZL, DGL, and the iEBL+eEBL (Hauser & Dwek 2001; Mattila 2006). SKYSURF is designed to investigate this apparent discrepancy between the total EBL signal and the discrete iEBL+eEBL. If real, this rather large discrepancy could be caused by a number of systematic errors that may result in larger foregrounds. In order of increasing distance from the HST instrument A/D converters, these are:

1. Uncorrected systematics in the HST sky-SB measurements, e.g., detector systematics (Section 4.1) or thermal dark signal (SKYSURF-2);

2. Close sources of stray light (e.g., earthshine or scattered sunlight; Section 4.3);
3. Systematic deviations from, or missing components in, the ZL model (SKYSURF-2);
4. Systematic deviations from and uncertainties in the DGL model (see references in SKYSURF-2);
5. Contributions by Intra-galaxy Halo Light (IHL) or (undetected) low-SB galaxies (SKYSURF-2); and
6. Diffuse light from reionization (e.g., Windhorst et al. 2018).

Because we do not know the true cause of this discrepancy in Figure 1, we will hereafter refer to light sources not accounted for by HST systematics, identifiable stray light, the ZL and DGL models, or the discrete EBL more generally, as “diffuse light” and not as “dEBL.” Further details on possible sources of diffuse light are given in SKYSURF-2.

In summary, most of the *discrete* EBL comes from moderately faint galaxies at $17 \lesssim AB \lesssim 22$ mag in the redshift range $0.5 \lesssim z \lesssim 2$. The true level and source of any diffuse light are as yet unclear. SKYSURF is designed to help reconcile the total EBL measurements with the integrated and extrapolated EBL (Figures 1–2), and to investigate how much room may be left for a truly diffuse light component, whatever its nature.

2.5. SKYSURF’s High-level Project Outline

SKYSURF has two main science parts, and two essential supporting parts, as illustrated in the colored columns and rows in Figure 3. Here, we briefly highlight both science parts, with details discussed in Sections 3–4.

2.5.1. SKYSURF-SB: All-sky Constraints for ZL and DGL

As indicated by the orange columns in Figure 3, SKYSURF will estimate the *absolute* sky-SB at $0.2\text{--}1.7\ \mu\text{m}$ using the methods of Section 4. From 249,861 ACS+WFC3 images in the Archive, we select those with the lowest contamination due to earthshine, Sun and Moon. The measured SB values sample the entire sky and can be modeled as:

$$\begin{aligned} \text{SB}(\lambda, l^{\text{Ecl}}, b^{\text{Ecl}}, l^{\text{II}}, b^{\text{II}}, t, \text{SA}, T) \\ = \text{TD}(\lambda, T) + \text{SL}(\lambda, t) + \text{ZL}(\lambda, l^{\text{Ecl}}, b^{\text{Ecl}}, t, \text{SA}) \\ + \text{DGL}(\lambda, l^{\text{II}}, b^{\text{II}}) + \text{EBL}(\lambda). \end{aligned} \quad (2)$$

Here, ZL(t) and DGL can be fit simultaneously on scales of degrees as a function of wavelength, ecliptic coordinates ($l^{\text{Ecl}}, b^{\text{Ecl}}$), Galactic coordinates ($l^{\text{II}}, b^{\text{II}}$), time of the year (t) or Modified Julian Date (MJD), and Sun Angle (SA), to match SKYSURF’s very large number of panchromatic sky-SB measurements. The time- or SA-dependence is the key factor that distinguishes the ZL from other SB components. The HST data do not sample the temporal and spatial parameter space as deeply and uniformly as the COBE/DIRBE data (e.g., Kelsall et al. 1998), but the HST sky-SB data do sample a wider range of solar elongations and cover a full calendar year (multiple times). The TD parameter on the right-hand side is the WFC3/IR thermal dark signal that depends on wavelength and HST’s ambient temperature T . This near-IR thermal component needs to be modeled and subtracted from any diffuse light signal that we observe (Section 4.1.4 and SKYSURF-2). The SL parameter indicates the stray light that the HST telescope + instruments receive from the Earth, the Sun, and the Moon,

which we attempt to minimize using the methods in Section 4.3 and SKYSURF-2 when assessing our constraints on the ZL, DGL, and EBL. The SL depends on wavelength and time or orbital phase, which determine the angles to the Earth’s limb, Sun, and Moon (Section 4.3).

In SKYSURF-2, we will identify any large differences between the HST sky-SB measurements and existing ZL models, which is most straightforwardly done at wavelengths $\lambda \simeq 1.25\text{--}1.6\ \mu\text{m}$ as a function of ecliptic latitude b^{Ecl} . A major goal of SKYSURF is to update the ZL models to cover the full $0.2\text{--}1.7\ \mu\text{m}$ wavelength range observed by SKYSURF, and the range of ($l^{\text{Ecl}}, b^{\text{Ecl}}$) and SA values sampled by HST.

2.5.2. SKYSURF Sources: Panchromatic Counts and iEBL/eEBL Averaged over Cosmic Variance

The discrete panchromatic object counting part of SKYSURF is indicated by the green columns in Figure 3, which provides discrete object catalogs, star–galaxy separation, and object counts in the main HST broadband filters across the sky. Because the normalized differential galaxy counts flatten with a converging slope for $AB \gtrsim 22$ mag (Figure 2(b)), most of the EBL energy (and its uncertainty) comes from galaxies with $AB \simeq 17\text{--}22$ mag at a median redshift $z \lesssim 1$. Their Cosmic Variance (CV) over a *single* HST FOV is $\sim 30\%\text{--}40\%$ at these redshifts (e.g., Somerville et al. 2004; Trenti & Stiavelli 2008; Moster et al. 2011; Driver et al. 2016a). SKYSURF’s goal is therefore to average the panchromatic galaxy counts over 1400 *well-separated* representative HST fields to reduce the iEBL errors from cosmic variance to $\lesssim 2\%$, or $\lesssim 4\%$ when accounting for the systematic and zero-point errors in Section 4.1.5. Even a *contiguous* HST survey region of 1400 fields (e.g., COSMOS) would still give $\sim 8\%$ CV, and such fields are not available in the 12 main broadband HST filters. Hence, SKYSURF’s *all-sky* distribution of the ~ 1400 independent HST fields in Figure 4 is *essential* to reduce CV in the resulting galaxy counts (Driver & Robotham 2010). Further details are given in Sections 3.2, 4.5, and Tompkins et al. (2022).

In what follows, we will define independent HST fields as those instrument FOVs that are far enough apart in the sky ($\gtrsim 1^\circ$) to provide faint galaxy counts that are sufficiently independent to average over CV. Figure 4 shows that there are 4858 independent HST FOVs using this definition, not all of which are usable for objects counts (Section 3.2 and Appendix B.3). As discussed in Section 3, the total number of instrument FOVs that SKYSURF has covered is $\sim 3.5\times$ larger, as many HST users have covered their targets on average by using a number of adjacent instrument FOVs.

To the typical 5σ completeness limits of $AB \lesssim 26\text{--}28$ mag of most drizzled SKYSURF images, we expect an integrated galaxy surface density of $(3\text{--}5) \times 10^5\ \text{deg}^{-2}$ (e.g., Figure 2ac). For the estimated total usable SKYSURF area of $\gtrsim 10\ \text{deg}^2$ (Section 3.2), this implies a total of $\sim (3\text{--}5) \times 10^6$ galaxies. Hence, SKYSURF will provide galaxy counts for a sample as large as the SDSS (York et al. 2000), but distributed over the whole sky and reaching ~ 5 mag deeper. Unlike SDSS, the SKYSURF discrete object sample does *not* cover a contiguous area. But because it sparsely samples the whole sky, SKYSURF’s discrete object catalogs will be well-suited to minimize cosmic variance in the galaxy counts. A key element of this SKYSURF goal is HST’s photometric stability over 11–18 yr of data (Section 4.1.5).

SKYSURF – Project Flowchart

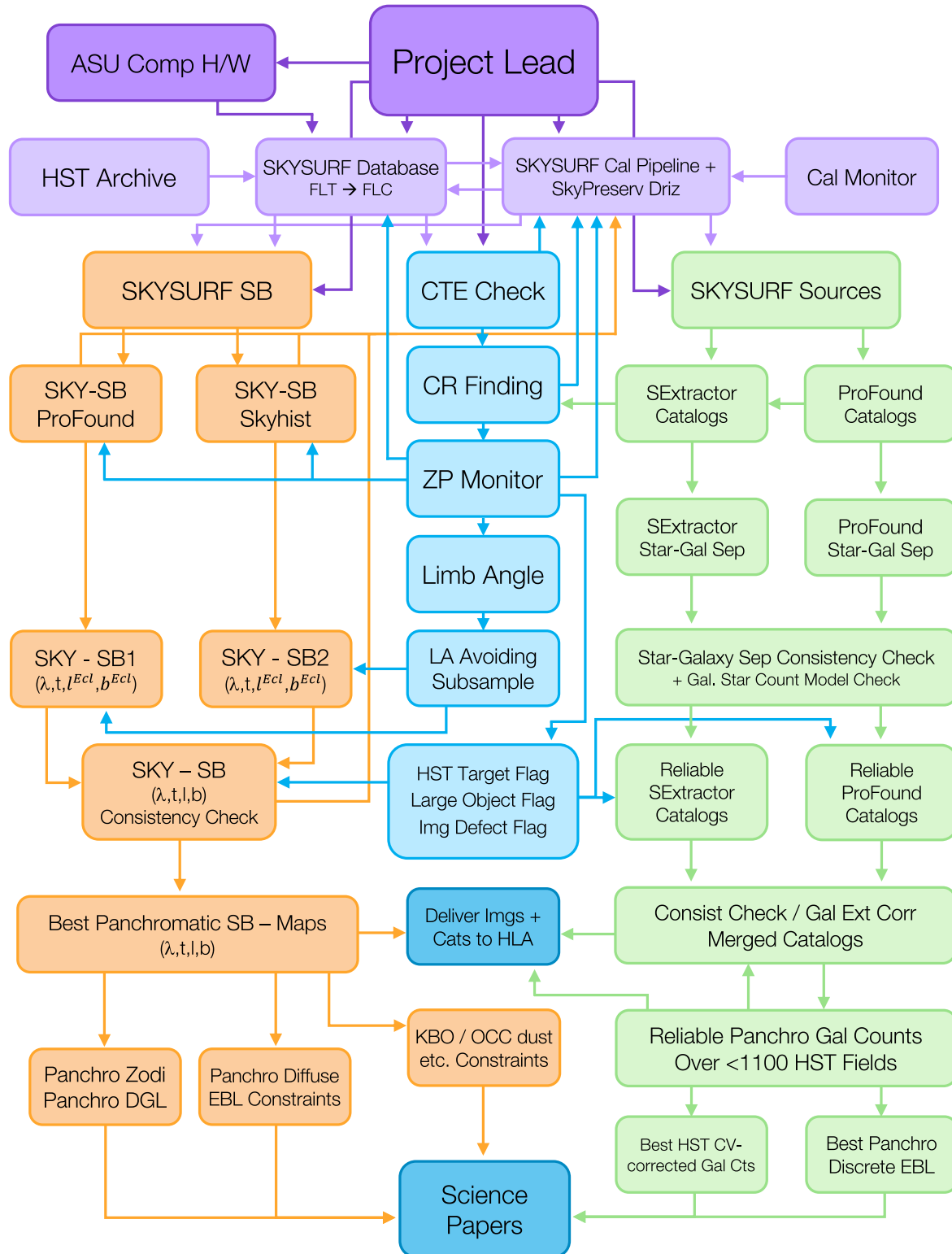


Figure 3. Flowchart for project SKYSURF. The orange columns indicate the two independent methods to do SKYSURF’s sky-SB studies, while the green columns indicate the two independent methods to perform SKYSURF’s panchromatic discrete object counts over ~1400 independent HST fields. The light purple row summarizes SKYSURF’s database building and standard processing steps. The light blue column summarizes SKYSURF’s nonstandard processing steps. “Skyhist” indicates our best percentile-clip method to estimate sky-SB values. Details are given in Sections 2.5 and 4.2.

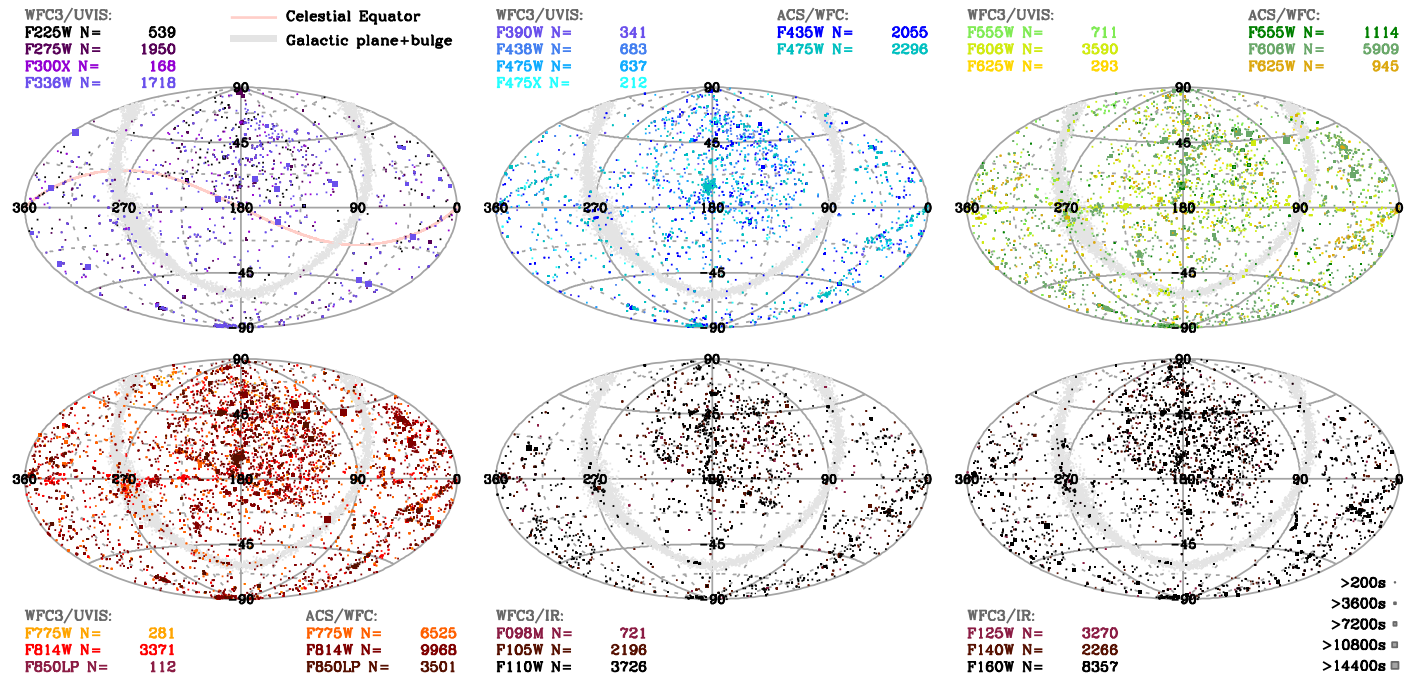


Figure 4. Aitoff equal-area projections in Ecliptic coordinates of *all* ACS/WFC and WFC3/UVIS+IR images with $t_{\text{exp}} \geq 200$ s that are publicly available as of 2019 September 23. The Galactic plane and bulge are represented by the light gray band, and the Celestial Equator is indicated by the pink curve (upper left). SKYSURF measures the absolute all-sky surface brightness $S(\lambda, t, l^{\text{Ecl}}, b^{\text{Ecl}})$ in 12 main broadband filters at $\sim 0.2\text{--}1.7 \mu\text{m}$ in wavelength from 249,861 HST Archival images in ~ 1400 independent HST fields (Equation (2) in Section 2).

2.5.3. SKYSURF Plan

Because the SKYSURF database contains 249,861 HST Archival images, it does *not*, in general, lack sufficient statistics, not even after conservative removal of large foreground targets and image defects (Appendix B.3). Instead, SKYSURF is limited by systematic errors, and for this reason, we need to carefully account for possible systematics summarized in Section 4. Hence, SKYSURF carries out each of its two main science goals—accurate panchromatic sky-SB measurements and object counts—along two main independent paths for each, indicated by the two orange and two green columns in Figure 3, with significant cross-checks. The purple rows in Figure 3 show SKYSURF’s database building and its data processing (Sections 3 and 4), while the blue column shows its specific data flagging steps (Section 4 and Appendix B.3).

3. Project SKYSURF—Database Overview

In this section, we summarize the selection of the SKYSURF instruments, filters, and exposures (Section 3.1), and the resulting SKYSURF database and total usable survey area (Section 3.2). The database considered for SKYSURF ranges from each instrument’s launch date until 2020 January, when we started building its database. Summaries of each HST instrument used in SKYSURF and their data reduction pipelines can be found in the Instrument Handbooks (IHBs), Data Handbooks (DHBs), and Instrument Science Reports (ISRs) listed on the STScI website.¹³ Specific HST instrument details relevant for SKYSURF are discussed in Section 4.1.

3.1. SKYSURF Instruments, Filters, and Exposures

HST Instruments Used: SKYSURF’s Archival data come from HST’s primary wide field imaging instruments: ACS/

WFC, WFPC2, WFC3/UVIS, and WFC3/IR. These data span more than 17 yr for ACS (2002–2020), ~ 16 yr for WFPC2 (1994–2009), and ~ 11 yr for WFC3 (2009–2020). Despite its much older detectors, broadband WFPC2 images were included in SKYSURF because they provide an earlier time baseline (1994–2009). ACS/WFC and WFC3/UVIS have higher throughput than WFPC2, but due to its much larger pixels, WFPC2’s sensitivity to SB is comparable to that of ACS/WFC and WFC3/UVIS. For many targets, WFPC2 provides broadband exposures in the common “BVI” filters (F555W, F606W, and F814W) that were later replicated in the same filters with ACS/WFC or WFC3/UVIS. Hence, we will compare the older WFPC2 sky-SB estimates for the same targets observed at the same time of the year as (i.e., at Sun angles similar to) those observed later in the *same* filters with ACS/WFC or WFC3/UVIS. This provides SKYSURF with an independent assessment of subtle instrument systematics in the sky-SB measurements and zero-point drifts over the decades. Details are given in O’Brien et al. (2022).

WFPC2, ACS/WFC, and WFC3/UVIS+IR Images Not Used in SKYSURF: We did *not* retrieve from the HST Archive all of the following ACS/WFC, WFPC2, WFC3/UVIS, and WFC3/IR image types for SKYSURF: (1) grism, narrowband, and most medium-band images; (2) images taken with quad or linear ramp filters; (3) images that use subarrays or time series; (4) images of (fast) moving targets; (5) WFC3/UVIS or WFC3/IR images that were produced by spatial scans; and (6) ACS polarization images where a polarizer is crossed with a broadband filter. This is because these images are harder to calibrate and their sky-SB would be much harder to measure, since it may not be uniform across these specialized images by their very design.

Other HST Cameras Not Used in SKYSURF: The following other HST cameras have been on board the HST spacecraft part of the last 32 yr, but are not used for SKYSURF: WF/PC-1,

¹³ <https://www.stsci.edu/hst/instrumentation>

Table 1
SKYSURF Data Summary—WFPC2

Instr/	N_{Exp}	Disk	N_{Exp}	$t_{\text{exp}}^{50\%}$	$t_{\text{exp}}^{25\%}$	$t_{\text{exp}}^{75\%}$	$t_{\text{exp}}^{50\%}$	$t_{\text{exp}}^{25\%}$	$t_{\text{exp}}^{75\%}$	50% Limit	25% Limit	75% Limit
Filter		Space		—only $t_{\text{exp}} \geq 200$ s —			—for All t_{exp} —			—for Images with All t_{exp}^a —		
		(GB)		(s)	(s)	(s)	(s)	(s)	(s)	(AB-mag)	(AB-mag)	(AB-mag)
WFPC2												
F255W	796	97.0	796	500	300	800	500	300	800	22.54	22.00	23.03
F300W	11019	97.0	10744	800	400	1000	800	400	1000	25.17	24.44	25.40
F336W	2514	22.0	2134	600	400	900	600	400	1000	24.71	24.28	25.24
F380W	89	0.8	89	600	500	1000	600	500	1000	25.16	24.98	25.67
F439W	1298	12.0	1298	500	313	700	500	313	700	24.65	24.16	24.99
F450W	5991	84.0	5988	600	400	1000	600	400	1000	25.90	25.51	26.36
F547M	611	5.3	611	400	300	600	400	300	600	25.25	24.97	25.63
F555W	6829	59.0	6457	500	350	1100	600	350	1200	26.34	25.88	26.88
F569W	44	0.37	44	800	500	1100	800	500	1100	26.37	25.97	26.62
F606W	24265	205.0	24168	600	500	1000	600	500	1000	26.63	26.49	27.00
F622W	186	1.6	186	900	600	1000	900	600	1000	26.57	26.25	26.65
F675W	1926	17.0	1822	500	400	700	500	400	700	25.90	25.71	26.17
F702W	2006	17.0	2000	700	400	1200	700	400	1200	26.47	26.03	26.86
F785LP	274	2.4	274	500	500	500	500	500	500	25.01	25.01	25.01
F791W	478	4.1	471	350	260	600	375	260	600	25.33	25.00	25.73
F814W	18759	160.0	18659	600	400	1100	600	400	1100	25.86	25.52	26.33
F850LP	1002	8.8	1002	400	400	600	400	400	600	24.17	24.17	24.57
Subtot	78087	793	76743									

Note.

^a Detection limit is the AB-magnitude for 5σ point sources at the median (50%) exposure time $t_{\text{exp}}^{50\%}$ listed. The 25% and 75% columns indicate the exposure times and corresponding 5σ point-source detection limits for the shallowest 25% and 75% of the images, respectively.

FOC, ACS/HRC and SBC, NICMOS NIC1, NIC2, NIC3, STIS/CCD, and STIS/MAMA. For WF/PC-1, this is because the instrument was in HST’s spherically aberrated beam, which affects both point-source detection and accurate SB measurements (e.g., Windhorst et al. 1992, 1994a). The ACS/HRC and SBC, FOC, NICMOS NIC1, NIC2, NIC3, STIS/CCD, and STIS/MAMA images are not used, because they cover very small FOVs and/or have rather unusual or very broadband filter sets that would be hard to compare to measurements in the standard modern filter sets present in ACS/WFC, WFPC2, or WFC3. NICMOS also has significant time-dependent dark-current levels (the “pedestal” effect) that would make dark-current subtraction and absolute sky-SB measurements rather uncertain, despite the advantage of significantly lower foregrounds in the near-IR over the other early HST instruments.

SKYSURF Pointings: The HST pointings used for SKYSURF are not completely randomly distributed across the sky (Figure 4). They are sparser in the south than in the north, with a tendency to avoid the Galactic plane ($|b_{\text{Gal}}| \lesssim 20^\circ$) and favoring the celestial equator ($\text{decl.} \simeq 0^\circ$). These biases can be due to, e.g., HST observers selecting targets from ground-based surveys in equatorial regions that can be accessed by ground-based telescopes in both hemispheres, and from the SDSS, whose footprint is clearly visible through its higher density of HST targets in Figure 4 (see Section 3.2).

SKYSURF Filters: We use the 12 main broadband filters between 0.2 and $1.7 \mu\text{m}$ (UV [F225W]–H [F160W]). Figure 4 shows that SKYSURF has 28 broadband ACS and WFC3 filters in total. Many of these filters are very similar in wavelength and may be grouped together (after small zero-point corrections and differential K-corrections; see Windhorst et al. 2011) when combining them into the panchromatic galaxy counts. All 28 filters will be used for panchromatic sky-

SB determination at their appropriate effective wavelengths (λ_{eff}), but the galaxy counts may be combined in very similar filters. Filter red leaks and blue leaks are discussed in Section 4.1.

Wide Field Planetary Camera 2 Data since 1994: The main SKYSURF filters used for WFPC2 are the F300W, F336W, F439W, F450W, F555W, F606W, F675W, F702W, F814W, and F850LP filters, plus several other less-used broadband filters summarized in Table 1.

Advanced Camera for Surveys/Wide Field Channel data since 2002: The main SKYSURF filters used for the ACS/WFC are the F435W, F475W, F555W, F606W, F775W, F814W, and F850LP filters, also broadly referred to as the ACS “BViz” filters, plus several other less-used broadband filters summarized in Table 2(a).

Wide Field Camera 3 UVIS Data since 2009: The main SKYSURF filters used for WFC3/UVIS are the vacuum UV filters F225W, F275W, F336W, and the F438W, F555W, F606W, and F814W, filters, also broadly referred to as the WFC3 “BVI” filters, plus several other less-used broadband WFC3/UVIS filters, including F775W and F850LP, summarized in Table 2(b). Where possible, these WFC3/UVIS filters are used as external checks on the ACS/WFC sky-SB values measured in the same filters on the same targets observed at similar times of the year.

Wide Field Camera 3 IR data since 2009: The main SKYSURF filters used for WFC3/IR are the F098W, F105W, F110W, F125W, F140W, and F160W filters, as summarized in Table 3, plus several other less-used medium-band or narrowband filters used for the WFC3/IR thermal dark signal calibration in SKYSURF-2.

SKYSURF Exposures and Exposure Times: We initially considered all ACS/WFC, WFPC3, WFC3/UVIS, and WFC3/

Table 2
SKYSURF Data Summary—ACS/WFC and WFC3/UVIS

Instr/ Filter	N_{Exp}	Disk Space (GB)	N_{Exp}	$t_{\text{exp}}^{50\%}$	$t_{\text{exp}}^{25\%}$	$t_{\text{exp}}^{75\%}$	$t_{\text{exp}}^{50\%}$	$t_{\text{exp}}^{25\%}$	$t_{\text{exp}}^{75\%}$	50% Limit	25% Limit	75% Limit
				—Only $t_{\text{exp}} \geq 200$ s—			—for All t_{exp} —			—for Images with All t_{exp}^a —		
				(s)	(s)	(s)	(s)	(s)	(s)	(AB-mag)	(AB-mag)	(AB-mag)
ACS/WFC												
F435W	5898	1250	5461	661	500	1200	650	440	1200	26.09	25.71	26.66
F475W	6280	1380	5417	522	370	700	470	365	674	26.12	25.89	26.46
F555W	2555	560	2317	540	385	700	520	370	697	25.88	25.55	26.15
F606W	16930	3730	15990	530	400	784	515	382	767	26.50	26.25	26.82
F625W	1839	380	1479	532	382	600	467	340	577	25.89	25.60	26.08
F775W	8953	2000	8675	510	404	716	503	400	608	25.70	25.48	25.87
F814W	30278	6710	27536	525	450	800	509	400	752	25.90	25.68	26.22
F850LP	8884	2000	8586	507	400	675	500	400	669	24.65	24.43	24.92
Subtot	81617	18010	75461									
WFC3/UVIS												
F225W	1600	280	1126	560	400	700	516	368	699	25.23	24.89	25.54
F275W	5622	920	3975	660	484	1212	528	190	800	25.24	24.20	25.65
F300X	366	61	141	609	351	869	450	100	600	25.87	24.37	26.14
F336W	4616	970	3999	645	470	820	600	408	800	25.91	25.52	26.19
F390W	1038	230	912	597	558	850	596	482	790	26.43	26.22	26.65
F438W	1851	260	1009	430	350	783	350	205	511	25.41	25.26	25.73
F475W	1977	240	905	800	400	1308	325	150	720	26.05	25.37	26.67
F475X	525	80	309	524	360	798	300	175	580	26.45	25.87	26.76
F555W	2271	350	1334	477	378	600	356	140	531	26.04	25.24	26.36
F606W	7794	1350	5484	599	400	843	425	300	700	26.37	26.11	26.71
F625W	804	100	425	515	400	700	370	180	621	25.85	25.27	26.26
F775W	688	170	279	606	400	699	320	200	507	25.23	24.90	25.56
F814W	10602	1880	6467	595	400	867	400	242	653	25.56	25.15	25.91
F850LP	330	50	192	374	364	473	349	200	379	24.42	23.87	24.49
Subtot	40084	6941	26557									

Note.

^a Detection limit is the AB-magnitude for 5σ point sources at the median (50%) exposure time $t_{\text{exp}}^{50\%}$ listed. The 25% and 75% columns indicate the exposure times and corresponding 5σ point-source detection limits for the shallowest 25% and 75% of the images, respectively.

IR exposures for SKYSURF processing, regardless of whether or not the LOW-SKY or SHADOW Special Requirements were specified by the HST observer in the Astronomers Proposal Tool (“APT”¹⁴). For sky-SB measurements, we subselect exposures of sufficient duration to allow robust estimates of the background level. For drizzling and discrete object catalog generation, we subselect images with exposure times $t_{\text{exp}} \geq 200$ s, which constitute the vast majority of images and ensure sufficient depth for our purposes. These are generally the exposures where the sky noise exceeds the read noise (except in the UV due to significant charge transfer inefficiency trails; see Section 4.1 and Appendix B.2), and so they are potentially the most useful for galaxy counts over as large of a random area as possible. As an example, the distribution of exposure times for all 6796 WFC3/IR F125W images available to SKYSURF is shown in Figure 5. The median exposure time is $t_{\text{exp}} \simeq 500$ s, where a typical F125W image reaches AB $\lesssim 26$ mag (5σ) for compact objects. In general, comparable median exposure times are found for SKYSURF’s other broadband filters listed in Tables 1–3. These tables also list the corresponding median image depths derived from the instrument exposure time calculators.

3.2. The Panchromatic SKYSURF HST Database and Total Usable Area

Number of Exposures and Retrieval: We retrieved from the HST Archive all 249,861 available images (81,617 ACS/WFC + 78,087 WFPC2 + 40,084 WFC3/UVIS + 50,073 WFC3/IR exposures), or $\gtrsim 26$ TB in total (Figure 4 and Tables 1–4). These images are all public as of 2020, and have exposure times up to one full orbit. Since processing and retrieval of such a vast amount of data posed some demands on the HST Archive, we spread ingestion over the Spring of 2020 with a typical transfer rate of ~ 175 GB per day. Complete disk copies of the SKYSURF database are kept at ASU in Arizona and at ICRAR at the University of Western Australia.

All-Sky Maps of Available Panchromatic SKYSURF Images: All-sky maps of all images eligible for SKYSURF analysis are shown in Figures 4(a)–(f). The SDSS footprint appears as the better-sampled tilted rectangle in Figure 4, since the SDSS has provided many targets for HST survey and SNAPSHOT programs, and many of those images are suitable for SKYSURF. In our all-sky sky-SB analysis, SKYSURF will appropriately weigh the uneven sampling of panchromatic sky-SB values due to this higher HST field-density inside the SDSS footprint (Equation (2)), as well as the resulting all-sky discrete object counts over ~ 1400 independent HST fields (Section 4.5 and Appendix C), as needed.

¹⁴ <https://www.stsci.edu/scientific-community/software/astronomers-proposal-tool-apt>

Table 3
SKYSURF Data Summary—WFC3/IR

Instr/	N_{Exp}	Disk	N_{Exp}	$t_{\text{exp}}^{50\%}$	$t_{\text{exp}}^{25\%}$	$t_{\text{exp}}^{75\%}$	$t_{\text{exp}}^{50\%}$	$t_{\text{exp}}^{25\%}$	$t_{\text{exp}}^{75\%}$	50% Limit	25% Limit	75% Limit
Filter		Space	—Only $t_{\text{exp}} \geq 200$ s—			—for All t_{exp} —			—for Images with All t_{exp}^a —			
		(GB)		(s)	(s)	(s)	(s)	(s)	(s)	(AB-mag)	(AB-mag)	(AB-mag)
WFC3/IR												
F098M	1158	7	1103	703	603	1003	703	553	1003	25.98	25.80	26.23
F105W	5412	33	4792	603	299	903	403	228	803	25.98	25.53	26.46
F110W	8847	54	6473	353	253	603	288	203	503	26.08	25.82	26.47
F125W	6810	39	5554	553	453	703	503	299	653	26.06	25.68	26.24
F140W	5647	35	4691	349	228	603	299	203	553	25.80	25.49	26.24
F160W	22199	140	19283	503	399	653	453	303	603	25.69	25.38	25.89
Subtot	50073	308	41896									
Total	249861	26052	220657									

Note.

^a Detection limit is the AB-magnitude for 5σ point sources at the median (50%) exposure time $t_{\text{exp}}^{50\%}$ listed. The 25% and 75% columns indicate the exposure times and corresponding 5σ point-source detection limits for the shallowest 25% and 75% of the images, respectively. The last row gives the grand total over Tables 1–3.

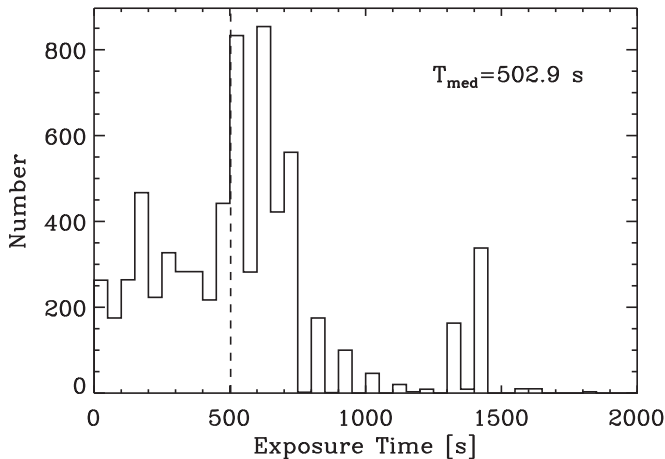


Figure 5. Exposure time distribution for all WFC3/IR F125W images available to SKYSURF. The median exposure time of the individual F125W images is $t_{\text{exp}} \simeq 500$ s. The exposure time distributions for the other WFC3/IR filters are similar. According to the WFC3 IHB (Dressel 2021) and our Figure 10, at this median 500 s depth, the individual WFC3 F125W images reach $AB \lesssim 26.0$ mag for point-source detection, so that most faint compact objects with $AB \gtrsim 26.5$ mag would have been missed in these short exposures. This detection limit somewhat affects the sky-SB estimates from these images after repeated mode-fitting or $n\sigma$ clipping to remove the detected objects, which masks the detected objects with $AB \lesssim 26.0$ mag, but does not remove the flux from nondetected objects at $AB \gtrsim 26.5$ mag.

Estimated Total Usable SKYSURF Area: Table 4 summarizes the total number of exposures per SKYSURF instrument, to estimate the maximum usable area that HST has covered with these data since 1994. Each instrument uses between one and three detectors per camera, and Col. 5 lists the total number of SKYSURF *single exposures* of the full cameras (except for WFPC2, where the PC1 data were discarded). Col. 3 lists the FOV (in arcsec) for each of the *full* camera exposures, and Col. 4 the total area per full exposure in each camera. Col. 6 lists for each camera the approximate average number of exposures per filter and the approximate average number of filters used on each HST pointing, as well as their product. Since 1994, the average HST user of WFPC2, ACS, or WFC3 has used an average of ~ 8 exposures per filter and ~ 1.8 filters per pointing. The total number of filters per FOV ranges from 1 for single-exposure SNAPshot targets to 13 for the

HUDF. Col. 7 lists the estimated number of independent HST pointings or FOVs in each full camera, which are considered to be those that are more than 1.0 FOV (or $\gtrsim 6'$) apart in their pointing centers, given the single detector FOV values in Col. 3. In Section 4.5, we discuss the definition of the drizzle footprints that determined these associations. Col. 8 lists the maximum SKYSURF area covered by each camera, which is not yet corrected for repeat visits of a given pointing with a different camera in the same filter. This will be done when the footprints and drizzling of all SKYSURF data are finished on AWS (Sections 4.5–4.6). Hence, only an upper limit to the total *unique* SKYSURF area is listed that may be usable for independent object counts across the sky.

Of the 249,861 individual exposures in the SKYSURF database, 220,657 images have $t_{\text{exp}} \geq 200$ s and are spread out over 16,822 HST pointings or FOVs across the sky (Figure 4). The 249,861 SKYSURF exposures from Tables 1–3 contain $\gtrsim 878,000$ individual detector readouts, including the 50,073 WFC3/IR exposures that we split into their individual ramp-readouts to better monitor the sky-SB versus orbital phase (Section 4.3). All 249,861 SKYSURF exposures are processed through the initial SB-measurement steps of Section 4.2, as it cannot be determined a priori whether or not they are useful for SKYSURF’s sky-SB goals. We estimate that about one-third of all these images have LOW-SKY or SHADOW flags or equivalent low background levels, such that they can constrain the ZL, DGL, or any diffuse light.

The subset of 220,657 images with $t_{\text{exp}} \geq 200$ s is used for drizzling, object catalogs, and counts, and has covered $\lesssim 32$ deg² across the sky since 1994 (Table 4). Of this total area, not all images are usable for SKYSURF background object counts, e.g., due to large targets that overflow the FOV, Galactic plane targets, or large artifacts (Appendix B.3). We estimate that about 30%–50% of these 16,822 HST FOVs, or ~ 10 deg², are in principle usable for object counts. In total, 4858 of the 16,822 HST FOVs are $\gtrsim 1^\circ$ away from the nearest-neighbor HST field. Here, we assume that angular distances $\gtrsim 1^\circ$ at $z \simeq 1$ –2—corresponding to $\gtrsim 30$ Mpc in Planck cosmology (Planck Collaboration et al. 2016)—make the galaxy counts in such fields sufficiently independent to average over CV (Driver & Robotham 2010). Of these 4858 independent FOVs, we also expect $\sim 30\%$ – 50% to survive the large-target or large-defect

Table 4
Total Number of Exposures per SKYSURF Instrument to be Drizzled, and Maximum Area Covered

SKYSURF Instrument (1)	$N_{\text{chip}}^{\text{b}}$ (2)	FOV /Chip (3)	Area/Exp (arcmin ²) (4)	N_{Exp} (5)	$N_{\text{Exp}}/\text{Filt} \times N_{\text{Filt}}/\text{Point}^{\text{c}}$ (6)	$N_{\text{FOV}}^{\text{d}}$ (7)	Max. Total Area (deg ²) ^e (8)
WFPC2 ^a	3	75" × 75"	4.69	76,743	~6.01 × 1.77 ≈ 10.61	7230	9.42
ACS/WFC	2	202" × 101"	11.33	75,461	~9.39 × 1.70 ≈ 16.00	4717	14.85
WFC3/UVIS	2	162" × 81"	7.29	26,557	~6.24 × 1.92 ≈ 11.97	2219	4.49
WFC3/IR	1	136" × 123"	4.65	41,896	~8.86 × 1.78 ≈ 15.77	2656	3.43
Total SKYSURF ^f			(7.27)	220,657	(7.74 × 1.77) ≈ (13.65)	16,822	~32

Notes.

^a The WFPC2 FOV consists of three 800² pixel CCDs (WF2–WF4), each with 0".10 pixels and a usable area of 750² pixels. Each WF CCD thus covers 1.56 arcmin² for a total WF area of 4.69 arcmin². In addition, WFPC2 has one 800² pixel CCD (PC1) with 0".046 pixels that covers 0.33 arcmin². PC1 is not used in SKYSURF, because of its higher noise per arcsec² and its larger calibration systematics.

^b Col. 2 lists the number of detectors typically used per camera, and therefore the number of detector readouts that form one exposure in a given FITS file (e.g., <https://hst-docs.stsci.edu/acsdhb/chapter-2-acs-data-structure/2-2-acs-file-structure>) and its extensions. Col. 3 lists the FOV (in arcsec) for each of the *single* detectors, and Col. 4 the total area covered by the *full* camera in each single exposure (in arcmin²).

^c Col. 5 lists the total number of SKYSURF FITS files that contain the single exposure data from each *full* camera. Col. 6 lists for each camera the approximate average number of exposures per filter and the approximate average number of filters used on each HST pointing, as well as their product.

^d Col. 7 lists the estimated number of independent HST pointings or FOVs in each camera, which are considered to be those that are more than 1.0 FOV diameter (or $\gtrsim 6'$) apart in their pointing centers. This is simply Col. 5 divided by the result of Col. 6. Section 4.5 gives details of how the independent FOVs and subsequent drizzle footprints were defined.

^e Col. 8 lists the *maximum* SKYSURF area covered by each camera, which is not yet corrected for repeat visits of a given pointing with a different camera in the same filter. This will be done when the footprints and drizzling of all SKYSURF data are finished on AWS (Sections 3.2 and 4.5–4.6).

^f The bottom row lists the full camera area weighted over all exposure files, and the average number of exposures per filter times the average number of filters used per pointing ($\langle N_{\text{Exp}}/\text{Filt} \rangle \times \langle N_{\text{Filt}}/\text{Point} \rangle$)—each weighted with the total number of exposures in each camera (Col. 5)—as well as the *maximum total* area that SKYSURF may cover.

filtering above, so we expect that ~1400 of these HST targets can be meaningfully used to reduce CV in the galaxy counts. Henceforth, we refer to these as our “~1400 independent HST fields” suitable for galaxy counts.

4. High-level SKYSURF Methods

In this section, we discuss our methods to produce both sky-SB measurements and object catalogs from SKYSURF’s images, with the details needed to assess their accuracy, reliability, and completeness across the sky. This includes the calibration methods applied, the image zero points (ZP) and ZP monitors as a function of time, our algorithms to make object-free estimates of the sky-SB, the orbital sky-SB dependence and sources of stray light, and our treatment of sky-SB gradients. Because SKYSURF’s object catalogs affect our estimates of the object-free sky-SB, we also summarize SKYSURF image drizzling strategy and drizzle footprints, as well as our star–galaxy separation method and catalog reliability and completeness.

4.1. Calibration with Best Available Calibration Files, and Other General Calibration Aspects

In this section, we summarize the standard calibration of all SKYSURF images with the best available calibration files and other calibration considerations for SKYSURF’s specific purposes. This includes any sources that *systematically add or remove* electron (e^-) signal from the image sky-SB levels, as well as the zero points and ZP monitoring over time of each HST instrument from which data are used here. This first subsection discusses the effects that all instruments have in common, while the following subsections discuss specific aspects of each individual HST instrument as they may affect SKYSURF’s sky-SB measurements.

The relative sky-SB errors induced by each of the main aspects of the calibration process below are summarized in Table 5 as a percentage of the average sky-SB levels measured, with references to the sections below where details are given. All errors are 1σ compared to the mean trends in the calibration parameters discussed in or estimated from the ISRs or IHBs cited below. In some cases, a range is given for the relative errors, which may depend on wavelength or the presence of image gradients. The bottom row of Table 5 lists the total relative error in each of the instrument sky-SB estimates, which assumes that the individual error components are independent. When an error range is listed, the largest of the percentage errors are propagated into the total error. Hence, we consider the total relative sky-SB errors to be conservative estimates.

Standard Calibration: SKYSURF calibrates each image using the latest on-orbit reference files and flux scale, including the standard bias-subtracted, dark-frame subtracted, flat-fielded images (the *_flt* files), which have also been CTE-corrected (the *_flc* files). The total of 249,861 images from Tables 1–3 were retrieved from the Mikulski Archive for Space Telescopes (MAST¹⁵) in Jan–May 2020 using the pipeline in effect as of that time period. For ACS, this is the `calacs` pipeline version 10.2.1, and for WFC3, the `calwfc3` pipeline version 3.5.0. The WFC3/UVIS images were downloaded again in early 2022, calibrated with `calwfc3` pipeline version 3.6.2 to implement the 2021 CTE corrections (Appendix B.2) and to automatically correct for the slowly time-varying filter zero points as a function of wavelength (Section 4.1.5). O’Brien et al. (2022) summarize the differences in the ACS/WFC and WFC3/UVIS detector design and the resulting subtle differences in their calibration pipelines as relevant for SKYSURF.

¹⁵ <https://archive.stsci.edu>

Table 5
Error Estimates^a in Calibration, Zero Points, Sky-SB Measurements, and Thermal Dark Signals

Source of Error	WFPC2	ACS/WFC	WFC3/UVIS	—WFC3/IR—			(Section)
				F125W	F140W	F160W	
(1)	(2)	(3)	(4)	(5)	(6)	(7)	(8)
Bias/dark-frame subtraction	~1.0%	~1.5%	~1.5%	~1.0%	~1.0%	~1.0%	4.1
Dark glow subtraction	~2%	4.1.1
Postflash subtraction	...	~1%	~1%	4.1
Global flat-field quality ^b	~1%–3%	0.6%–2.2%	~2%–3%	~0.5%–2%	~0.5%–2%	~0.5%–2%	4.1
Numerical accuracy of LES ^c	≤0.2%–0.4%	≤0.2%–0.4%	≤0.2%–0.4%	≤0.2%–0.4%	≤0.2%–0.4%	≤0.2%–0.4%	4.2.3
Photometric zero points ^d	~2%	0.5%–1%	0.5%–1%	~1.5%	~1.5%	~1.5%	4.1.5
Thermal dark signal ^e	~0.2%	~0.5%	~2.7%	4.1.4, SKYSURF-2
Total error ^f	~4.3%	~3.0%	~3.7%	~2.7%	~2.8%	~3.8%	
Sky-SB low-avg (nW/m ² /sr)	262–534	251–513	240–496	
Sky-SB error (nW/m ² /sr)	7–14	7–14	15–19	

Notes.

^a The relative errors in this table are expressed as a percentage of the average sky-SB values in the HST images, which includes the typical zodiacal sky-SB and TD levels. The bottom two rows list both the lowest and average sky-SB values plus total errors for each in units of nW m⁻² sr⁻¹ for the WFC3/IR F125W, F140W, and F160W filters, respectively (see also Figure 1 and SKYSURF-2).

^b For WFPC2, the large-scale flat-field errors in the filters F439W and redward are ≤1%, but the upper bound includes the 1% error in the contamination correction and the ~3% error in the residual CTE correction. For the less-frequently used WFPC2 UV filters, these errors can be larger.

^c Numerical accuracy of lowest estimated sky values away from detected objects (Section 4.2). The LES algorithms also avoid areas of significant persistence when estimating the sky-SB, which is not included as an extra term in the error budget.

^d For WFC3/IR, this includes the ~0.5% uncertainty in the applied detector count-rate nonlinearity correction (Section 4.1.4).

^e The errors in the estimated thermal dark signal values for the F125W, F140W, and F160W filters reflect a plausible range in HST component temperatures of $\Delta T \approx \pm 2$ K (see Table 2 in SKYSURF-2). The TD errors increase from 1.25 to 1.6 μ m, due to the increased blackbody contributions as modeled across the WFC3/IR filter set. For the darkest sky-SB values, the additive percentage TD error is about 2× larger than quoted here, resulting in the total errors for the darkest sky-SB values increasing to ~2.8%, ~2.9%, ~6.3% in the F125W, F140W, and F160W filters, respectively.

^f The total relative error is the quadratic sum of the individual relative errors in the calibration, zero points, numerical sky-SB estimates, and dark signals, assuming these are all independent. These errors are incorporated into our error budget in the tables in SKYSURF-2. The bottom row shows the errors in the lowest to average sky-SB values in the previous row, respectively.

All these calibrated images have *not* been sky-subtracted, and their calibration quality and flatness (in the absence of large bright objects; see Section 4.2) is critical for SKYSURF. The errors due to bias+dark-frame subtraction and flat-fielding are retrieved from the Instrument Handbooks and the Instrument Science Reports (ISRs). All these standard calibration errors are expressed as relative errors of the low-average sky-SB levels measured, and are summarized in the error budgets of Table 5 (Sections 4.1.6, 4.8, and SKYSURF-2). We note the following pipeline calibration details that are relevant for all of SKYSURF’s instruments below:

Geometrical Distortion Corrections (GDC): The calibrated SKYSURF images can be directly used to measure extended emission or sky-SB values before the images are drizzled. The flat-fielding process corrects each pixel’s SB for high-frequency (pixel-to-pixel) variations, and to first order for low-frequency, large-scale structures due to camera, chip, or illumination properties across the FOV. The flat-field process is thus designed to produce *_flt* files that would have constant values in all pixels if the original source had a perfectly uniform SB. However, due to the significant instrument distortion corrections in each of WFPC2, ACS, and WFC3 cameras, a Pixel Area Map (PAM) would need to be applied if one were to use the undrizzled images for *point-source photometry*, since the flat-fielding process is not explicitly designed to make point-source photometry uniform across the images. This is because instrument distortion causes some pixels to cover more area on the sky than others, so point-source photometry is location-dependent on the detectors. Once the overall sky-SB is measured on each SKYSURF image, the

drizzling process (Sections 4.5–4.6) explicitly performs the full GDCs, so that photometry on compact and extended sources will now *both* be accurate on the drizzled images. Hence, drizzling replaces the need for applying a PAM for point-source photometry.

Drizzling Pixel Scale: Drizzled images (Sections 4.5–4.6) have the proper GDC applied, and therefore give the correct photometry for both extended and point sources using the same images. The WFC3 IHB (Dressel 2021) states specifically that “In drizzled images (*_drz* files), photometry is correct for both point and extended sources.”¹⁶ In Sections 4.5–4.6, we will drizzle *all* SKYSURF images to the same pixel scale of 0.''060 pixel⁻¹, including *all single* exposures, so they may be used for discrete object finding and photometry. This will lead to some PSF undersampling of the cameras with the finest pixel scales (ACS/WFC with ~0.''05 pixel⁻¹ and WFC3/UVIS with ~0.''039 pixel⁻¹), but that is acceptable for SKYSURF’s first goal of all-sky panchromatic sky-SB measurements. It will also lead to some minor loss in point-source sensitivity for the ACS/WFC and WFC3/UVIS images, but SKYSURF has such a large dynamic range in flux and area that this will not be a limitation to its second goal of accurate all-sky panchromatic object counts from ~1400 independent HST fields (Section 2.5.2). This choice of drizzled pixel size also significantly reduces the storage requirements of SKYSURF’s final output images, as well as the AWS processing costs, as compared to smaller pixels.

¹⁶ <https://hst-docs.stsci.edu/wfc3dnhb/chapter-7-wfc3-ir-sources-of-error/7-8-ir-flat-fields>

Corrections for CCD Preflash or Postflash Levels: Charge Transfer Efficiency (CTE) degradation occurs in CCDs due to the heavy CR bombardment over time, and is especially noticeable at low sky-SB levels, and hence in all WFC3/UVIS vacuum-UV filters, as well as in all WFPC2, ACS/WFC, and WFC3/UVIS broadband filters well after each of the instruments’ Shuttle launches. When CTE effects are severe, then CTE corrections as applied in the pipeline (e.g., Anderson & Bedin 2010) may not be sufficient. Most observers will have anticipated this by adding a “preflash” level to their WFPC2 exposures, or a “postflash” to their ACS/WFC or WFC3/UVIS CCD exposures, to bring the sky-SB up to a level where the CTE traps are largely filled. Therefore, SKYSURF needs to verify whether the WFPC2 preflash and ACS/WFC and WFC3/UVIS postflash levels in the broadband filters were properly subtracted in the pipelines before reliable sky-SB measurements can be made. All preflash or postflash levels are prescribed by the observer, and the best-estimate preflash or postflash frames are subtracted in the instrument pipelines.

The WFC3/UVIS postflash frames have low-level gradients of $\lesssim 20\%$, with overall amplitudes that depend somewhat nonlinearly on the duration of the postflash level selected by the user (Biretta & Baggett 2013). These authors state that “examination of the long-term stability of the postflash LEDs shows no evidence of systematic fading over 9 months.” Biretta & Baggett (2013) find quasi-random LED brightness fluctuations with rms amplitude of $\sim 0.6\text{--}1.2\%$ (e.g., their Figure 14–16). Since CTE degradation has steadily increased over the years, the recommended postflash levels to fill in the traps have increased from $0\text{ }e^- \text{ pix}^{-1}$ in 2009 to $\gtrsim 20\text{ }e^- \text{ pix}^{-1}$ in 2020 and beyond.

Taking the F606W filter as an example, Figure 1 shows that a typical zodiacal sky-SB is $\sim 562\text{ nW m}^{-2}\text{ sr}^{-1}$ or $V\sim 22.86\text{ AB-mag arcsec}^{-2}$. With the WFC3/UVIS F606W zero point of 26.08 AB-mag (for $1.00\text{ }e^- \text{ s}^{-1}$) and $0''.0397$ pixel, this corresponds to a zodiacal sky-SB of $\sim 0.031\text{ }e^- \text{ pix}^{-1}\text{ s}^{-1}$. In an average ~ 500 sec F606W exposure, the F606W sky level then amounts to $\sim 15.3\text{ }e^- \text{ pix}^{-1}$. Hence, when an average LED postflash of $10\text{ }e^- \text{ pix}^{-1}$ gets added and subsequently subtracted in the pipeline, the above $\sim 1.2\%$ postflash subtraction error corresponds to a $\sim 0.5\%$ error (i.e., $\sim 0.12/(10+15)$) in the inferred sky-SB, with some variance around this number depending on the actual postflash level used. In the bluer WFC3/UVIS filters, the relative error due to the postflash subtraction will be larger than in F606W, but for ACS it will be somewhat smaller because of its larger $0''.05$ pixels and its ~ 0.4 mag higher throughput in the optical compared to WFC3/UVIS. We adopt $\sim 1\%$ of the average zodiacal sky-SB as the CCD postflash subtraction error in Table 5. A discussion of CTE effects on low-SB fluxes in the WFC3/UVIS UV filters—after the required postflash application and removal—is given by, e.g., Smith et al. (2018, 2020). Further details are given in Appendix B.2 and O’Brien et al. (2022).

Corrections for Detector Persistence: Bright point-like or very high SB targets (AB $\lesssim 15$ mag) in previous images may saturate and create a positive residual charge that decays exponentially with several timescales ranging from minutes to fractions of an hour, and so can persist in subsequent images with the same instrument in the same or in a different filter (e.g., Deustua et al. 2010; Long et al. 2010, 2012). A careful analysis of flat-field errors and persistence in the HUDF data by

Borlaff et al. (2019) removes these effects to SB levels of $\sim 32.5\text{ AB-mag arcsec}^{-2}$ in the WFC3/IR broadband near-IR filters. We tested for the effects of persistence in the SKYSURF’s WFC3/IR images with an average exposure time of $t_{\text{exp}} \simeq 500$ s, and concluded that the best sky-SB measuring algorithms of Section 4.2.3 are robust against the rare persistence images left in subsequent images. For discrete object catalogs (Appendix C.1), we need to remove all persistence images as flagged in the `calwf3` pipeline from the next few exposures.

Corrections for Detector Crosstalk: As summarized in, e.g., the WFC3 IHB (e.g., Deustua et al. 2010), crosstalk is a type of electronic ghosting that is common in CCD or IR detectors when two or more amplifier sections are read out by the A/D converters *simultaneously*. A bright source in one amplifier section causes a dim electronic ghosting in other amplifier section(s) at the corresponding pixels that are read out at the same time, in essence, because a spacecraft has no absolute electrical grounding. The offending signal dumps electrons into the imperfect local ground upon readout, thus reducing the signal sensed by the paired amplifier, and hence the negative sign of the crosstalk signal. This results in a bright point source (including hot pixels and CRs) or a very high-SB extended target—as read out by any detector’s A/D converter—generating an area of lower data numbers in corresponding, mirrored locations of an adjacent detector amplifier section. Crosstalk happens in both the ACS/WFC, WFC3/UVIS and WFC3/IR detectors, but not in WFPC2, because its four CCDs are read sequentially. The crosstalk amplitude is linear with the signal that gives rise to it in the adjacent amplifier section that is digitized during the same readout. During a full-frame, unbinned, four-amplifier readout, the crosstalk between WFC3/UVIS amplifier section A or C is $\sim -2 \times 10^{-4}$ of the source signal, while for a target in WFC3/UVIS amplifier section B or D, it is $\sim -7 \times 10^{-5}$ of the source signal (Vaiana & Baggett 2010; Suchkov & Baggett 2012). For WFC3/IR, crosstalk occurs between amplifiers 1 and 2, or between amplifiers 3 and 4, and amounts to $\sim -1 \times 10^{-6}$ of the source signal (note the *negative* sign of the crosstalk signal in all cases). For unsaturated sources, crosstalk thus is generally below the sky noise, but possibly still noticeable as a dim depression in the sky-SB if the cause is a large source with high SB in the adjacent amplifier section. When it occurs, crosstalk is generally identifiable and correctable to within 0.1% of the surrounding sky-SB. The most noticeable cases of crosstalk will be identified during our image flagging procedures in Section 4.2 and Appendix B.3. Further discussion of low-level systematics in the sky-SB estimates is given in O’Brien et al. (2022).

4.1.1. WFPC2

Here, we summarize the specific considerations for the WFPC2 data used in SKYSURF, with their error contributions summarized in Table 5.

WFPC2 CTE Degradation and Preflash: The WFPC2 CTE has gotten noticeably worse after 8–16 yr on-orbit, and so WFPC2 sky-SB measurements need to be done on preflashed images, which subsequently have this preflash level removed.

WFPC2-Window Dark Glow: The WFPC2 CCD “window glow” or “dark glow” is the largest source of instrumental error for WFPC2, due to low-level light from the field flattener lenses in front of the CCDs. The window glow is likely due to

irradiation of the MgF_2 in the field flattener by energetic particles (CRs), which may result in both Cherenkov radiation and fluorescence. There is therefore a correlation between the dark glow and the input cosmic ray (CR) flux with some scatter. Figure 4.6 of Biretta (2009) shows a *shallow* relation between CR-flux (= input) and Dark Glow (= output) for WFPC2 CCD WF2. The total CR-flux from the CR-only maps produced by SKYSURF can be used to predict the WFPC2 window glow. The glow is the same for CCDs WF3 and WF4, substantially higher for CCD PC1, and the lowest for CCD WF2, so we estimate the sky-SB primarily from the CCD detector WF2, and compare it to those estimated from WF3 and WF4 as a check.

According to the analytical WFPC2 dark current model in the WFPC2 IHB (Gonzaga & Biretta 2010),¹⁷ at the WFPC2 detector temperature of $T = -88^\circ \text{C}$, only about $0.5\text{--}1 \times 10^{-4} \text{ DN s}^{-1}$ of the measured dark-count rate is due to the usual dark current, while about $1\text{--}8 \times 10^{-4} \text{ DN/sec}$ comes from the glowing WFPC2 field flattener. There is also a very noticeable drop ($\sim 30\text{--}50\%$) in the dark rate within ~ 100 pixels of the edges of each WFPC2 CCD. The lowest ZL sky-SB that we measure in the WFPC2 filter F606W near the north ecliptic pole corresponds to 15 DN in 1800 s (Windhorst et al. 1994a, 1998). For an average dark glow of $0.77 \pm 0.18 \text{ DN}$ in 1800 s, the error from the dark glow subtraction does not exceed $\sim 1.2\%$ in *V*-band at the NEP and is slightly worse in *I*-band. The errors in the dark glow subtraction are smaller at lower latitudes and generally do not exceed $\sim 2\%$.

WFPC2 Stray Light: The orbit-dependent foregrounds such as earthshine produce elevated sky-SB levels as discussed and flagged in Section 4.3. In addition, earthshine propagates through the WFPC2 optical train in a way that not only elevates the sky-SB on the detector—as it does for all HST instruments—but also produces a recognizable pattern of diagonal (dark) bands across each detector caused by specifics of the WFPC2 optical train, in particular the alignment of the OTA and WFPC2 camera pupils (see, e.g., Section 11 of Biretta et al. 1995). These particular stray-light properties occur because the support struts for the repeater mirrors in WFPC2—which correct for HST’s spherical aberration—shadow HST’s secondary mirror support struts. For instance, such stray-light patterns caused by earthshine affected the F300W images taken for the Hubble Deep Field South, which were mostly taken in HST’s Continuous Viewing Zone (CVZ) during orbital “day time.” These patterns can be removed as described in, e.g., Section 3.4.2 of Casertano et al. (2000). The HST orbital phase monitoring of Section 4.3 flags and ignores such WFPC2 images affected by earthshine, as their sky-SB estimates may be affected in a way that is not correctable.

WFPC2 Decontaminations and Time-dependent UV Zero Points: Holtzman et al. (1995), McMaster & Whitmore (2002), and Casertano et al. (2000) describe calibration aspects specific to WFPC2. In orbit from 1993 December to 2009 May, the optical train of WFPC2 underwent gradual contamination, which affected its time-dependent sensitivity and zero points, especially the WFPC2 UV filters. Regular decontaminations of the WFPC2 instrument were therefore done, and the `calwfc2` pipeline applies post-contamination corrections for the time-dependent UV-filter zero points.

Further details can be found in McMaster & Whitmore (2002) and Section 5.2 of the WFPC2 Data Handbook.¹⁸

4.1.2. ACS/WFC

Here, we summarize the specific considerations for the ACS/WFC data used in SKYSURF, with their error contributions summarized in Table 5.

ACS/WFC Dark Current: The ACS/WFC dark current is $\sim 0.01 e^- \text{ pix}^{-1} \text{ s}^{-1}$ (Ryon 2022),¹⁹ and has slowly increased over time due to on-orbit detector degradation, with periodic drops due to changes in temperature setting in 2006 or the introduction of postflash in 2015, as shown in Figure 3 of Anand et al. (2022). Their Figure 3 shows that scatter in the ability to precisely determine the ACS/WFC dark-current level over the years is $\sim 0.001 e^- \text{ pix}^{-1} \text{ s}^{-1}$. Their Figure 2 shows that the ability to determine the dark-current level in an individual super-dark frame is considerably more accurate than this. For the average F606W zodiacal sky-SB level of $22.86 \text{ AB-mag arcsec}^{-2}$ (Table 2 of Windhorst et al. 2011; Figure 1 here) and the $0''.050 \text{ pixel}^{-1}$ scale of the ACS/WFC detector, $\sim 0.001 e^- \text{ pix}^{-1} \text{ s}^{-1}$ corresponds to a dark-current-induced error in the zodiacal sky-SB of $\sim 1.5\%$.

ACS/WFC Flat Fields: Cohen et al. (2020) present “LP” flats for ACS/WFC, which include corrections for both low (“L”) spatial frequency and pixel-to-pixel (“P”) flat-field variations. From their Figures 5 and 6, the errors induced by the ACS/WFC flat fields are $\sim 0.6\%\text{--}2.2\%$ of the zodiacal sky-SB for medium-length single exposures in our ACS/WFC database in Table 2(a).

ACS/WFC Fringing: Multiple reflections between the layers of a CCD detector can give rise to fringing at longer wavelengths ($\lambda \gtrsim 750\text{--}800 \text{ nm}$), where the amplitude of the fringes is a strong function of the silicon detector layer thickness and the spectral energy distribution of the light source, as discussed in the ACS IHB (Ryon 2022). The fringe pattern is stable and is removed to first order by the flat field for continuum sources (Ryon 2022).

ACS/WFC Red Stellar Halos: For ACS/WFC, we must correct sky-SB measurements in the F850LP for effects of the broad red stellar halos in the aberrated beam that may not be fully captured in the corrected beam (Appendix B.3).

4.1.3. WFC3/UVIS

Here, we summarize the specific considerations for the WFC3/UVIS data used in SKYSURF, with their error contributions summarized in Table 5.

WFC3/UVIS Flat Fields: The WFC3/UVIS global flat-field errors are $\sim 2\%\text{--}3\%$ across the detector for most WFC3/UVIS broadband filters (e.g., Rajan & Baggett 2010; Mack et al. 2015).

WFC3/UVIS Filter Red Leaks and Blue Leaks: The WFC3/UVIS filters were designed to have minimal red leaks for the bluer filters, and very small blue leaks for the redder filters. A detailed estimate of the WFC3/UVIS vacuum-UV filter red leaks is given in Figure 1(b) and Appendix B.1 of Smith et al. (2018). For the WFC3/UVIS optical broadband filters, red leaks are generally no larger than $\sim 10^{-5}\text{--}10^{-4}$ of in-band flux for a flat spectrum SED. A discussion of the effects from UV

¹⁷ <https://www.stsci.edu/hst/instrumentation/legacy/wfpc2>

¹⁸ <https://www.stsci.edu/hst/instrumentation/legacy/wfpc2> and https://www.stsci.edu/instruments/wfpc2/Wfpc2_dhb/wfpc2_ch53.html#1920857

¹⁹ <https://hst-docs.stsci.edu/acsihb>

filter pinholes on low-SB measurements is given in Appendix B.2 of Smith et al. (2018). Any UV filter pinhole would imprint a very broad red leak on the image, but because the WFC3/UVIS filters are placed at a significantly out-of-focus location in the optical train, pinhole red leak effects are generally dimmer than $AB \gtrsim 31$ mag arcsec⁻², or $\sim 1\%$ of the UV sky-SB.

WFC3/UVIS Fringing: As in the case of ACS/WFC, fringing may also affect the sky-SB in the reddest WFC3/UVIS filters, as discussed in the WFC3 IHB (Dressel 2021).²⁰

WFC3/UVIS Internal Reflections: Both WFC3/UVIS and IR can have complex internal reflections when bright stars are in the FOV (see, e.g., the figures in Section 4.2), or produce large artifacts (“dragon’s breath”) when a bright star lands exactly on the edge of the detector masks. Large artifacts or bright stars are flagged when making object catalogs (Appendices B.3 and C.1), and our code will discard these regions or images when making sky-SB estimates (Sections 4.2, 4.3, and SKYSURF-2).

4.1.4. WFC3/IR

Here, we summarize the specific considerations for the WFC3/IR data used in SKYSURF, with their error contributions summarized in Table 5. Because SKYSURF’s first science results in SKYSURF-2 come from the WFC3/IR sky-SB estimates, the known sources of systematic errors that could affect these estimates are summarized in more detail here.

WFC3/IR Blobs and Their Correction: WFC3/IR images show several small (10–15 pixel) blobs that form a stable low-level ($\sim 10\%$ – 15% on average) depression in the foreground (Pirzkal et al. 2010) affecting $\sim 1\%$ – 2% of the WFC3/IR pixels. The number of blobs has increased at a rate of $\lesssim 1$ per month, to a current total of ~ 150 blobs (Olszewski & Mack 2021). The WFC3/IR Blobs are believed to be due to “small particulate features with reduced QE” that accumulated on the WFC3 Channel Select Mechanism (CSM; Bus-house 2008). Specially constructed “Delta-flat fields” correct these features significantly, and known blobs are flagged in the data-quality arrays and ignored in our analysis, so they do not pose a significant source of error in the SB-estimating algorithms of Section 4.2.

WFC3/IR Flat Fields: The latest sky delta-flat fields have been implemented in the `calwfc3` pipeline. Figures 2 and 4 of Pirzkal et al. (2011) show that the flat-field error in WFC3/IR broadband filters is generally better than $\sim 0.5\%$ – 2% of the average zodiacal sky-SB, from the central 800^2 pixels of the detector to the edges, respectively (Mack et al. 2021). To be conservative, we adopt $\sim 2\%$ in Table 5 for the WFC3/IR flat-field-induced errors, as we cannot predict *where* in the SKYSURF images our algorithms of Section 4.2 will estimate the sky-SB values.

WFC3/IR Geometry: The WFC3/IR detector has 1014×1014 active pixels. To minimize internal reflections, the WFC3/IR detector has a $\sim 24^\circ$ tilt about its x -axis, creating an image elongation of $\sim 9\%$. The WFC3/IR detector therefore covers a rectangular $136'' \times 123''$ FOV with rectangular pixels of $0.''1341 \times 0.''1213$ on average.

WFC3/IR Filter Red Leaks and Blue Leaks: The WFC3/IR filters were also designed to have very small red leaks and blue leaks. The blue leaks are defined in the WFC3 IHB

(Dressel 2021) as the fraction of erroneous flux coming from 710 to 830 nm compared to the expected proper in-band flux. (The WFC3/IR QE curve is almost flat down to 780 nm but rapidly declines at bluer wavelengths.) Table 7.4 of the WFC3 IHB shows that, for a blackbody with $T_{\text{eff}} = 5000$ K (i.e., representing the reddened zodiacal spectrum used in SKYSURF-2), the WFC3/IR broadband filters have a blue leak of $\sim 2.4 \times 10^{-7}$ – 1.7×10^{-4} of the proper in-band flux. We verified this through numerical integration of the Solar spectrum through the full F125W filter curve available at STScI.²¹ This is an important consideration for SKYSURF, as more of the zodiacal sky-SB is generated *blueward* of the WFC3/IR filter throughput curves. The worst-case WFC3/IR blue leak is 1.7×10^{-4} of the in-band flux for the F160W filter (Dressel 2021). This is much smaller than other systematics that we encounter when measuring absolute sky-SB values in Sections 4.1.5–4.1.6, 4.3, and SKYSURF-2.

WFC3/IR—Splitting and Analyzing Exposures Using Individual Ramps: The WFC3/IR detector readouts are nondestructive, so all individual WFC3/IR exposures consist typically of 8–10 on-the-ramp subexposures, each of which are calibrated to facilitate correction for the numerous CR hits and to obtain the desired exposure depth. SKYSURF measures the sky-SB in each of the 8–10 individual WFC3/IR on-the-ramp subexposures, which enables us to better diagnose the behavior of the sky-SB (Section 4.3) and the thermal dark signal (SKYSURF-2) as a function of orbital phase. An example is shown in Figures 6(a)–(b). This process leaves some CRs in the on-the-ramp subexposures, which our robust sky-SB algorithms are designed to ignore (Section 4.3 and Appendix B.1). Only the full-ramp full-exposure WFC3/IR images that have been CR-filtered are used for SKYSURF’s object counts (Appendix C).

WFC3/IR Count-rate Nonlinearity Correction: Riess (2010) and Riess et al. (2019) discuss the changing WFC3 ZP due to its detector Count-Rate Nonlinearity (CRNL) over a very large dynamic range in flux. As a result, the WFC3/IR ZPs are slightly different for the bright calibration stars compared to faint galaxies, whose average SB is close to or below that of the zodiacal sky-SB. In all its filters, the WFC3/IR zero points are subject to CRNL of about 0.049 ± 0.005 mag (or $4.5\% \pm 0.5\%$) over the *full range* of 16 AB-mag (6.4 dex) in flux per pixel, or $\sim +0.0077 \pm 0.0008$ mag (or $\sim +0.71\% \pm 0.07\%$) over each 2.5 mag (1 dex) interval of flux per pixel. This detector CRNL is a charge-trapping problem, where up to 4.5% of the faint object and faint SB-flux are lost in detector traps, and is the opposite of persistence, which is mapped and removed as described in Section 4.1. WFC3/IR standard stars are measured in the total flux range of $12 \lesssim AB \lesssim 21$ mag, and of course cover an area about the size of the WFC3/IR PSF, which is $\gtrsim 0.0163$ arcsec². The sky-SB levels in the WFC3/IR broadband filters are on the order of 22.6–22.3 AB-mag arcsec⁻² (Table 2 of Windhorst et al. 2011; “W11”), or ~ 26.9 mag/PSF area. Hence, the SKYSURF sky-SB is measured at levels ~ 6 – 15 mag dimmer than the pixel signal of the standard stars used to determine the WFC3 zero points. We verified that the standard WFC3 pipeline `calwfc3` corrects all pixel SB levels accordingly for detector CRNL. In SKYSURF, typical sky-SB levels are corrected *upward* by $\sim [(6-15)/16] \times 4.5\% \simeq + (1.7-4.2)\%$ to match the standard star flux scale, while objects with higher SB per pixel are corrected by

²⁰ <https://hst-docs.stsci.edu/wfc3ihb>

²¹ <https://www.stsci.edu/hst/instrumentation/reference-data-for-calibration-and-tools/synphot-throughput-tables>

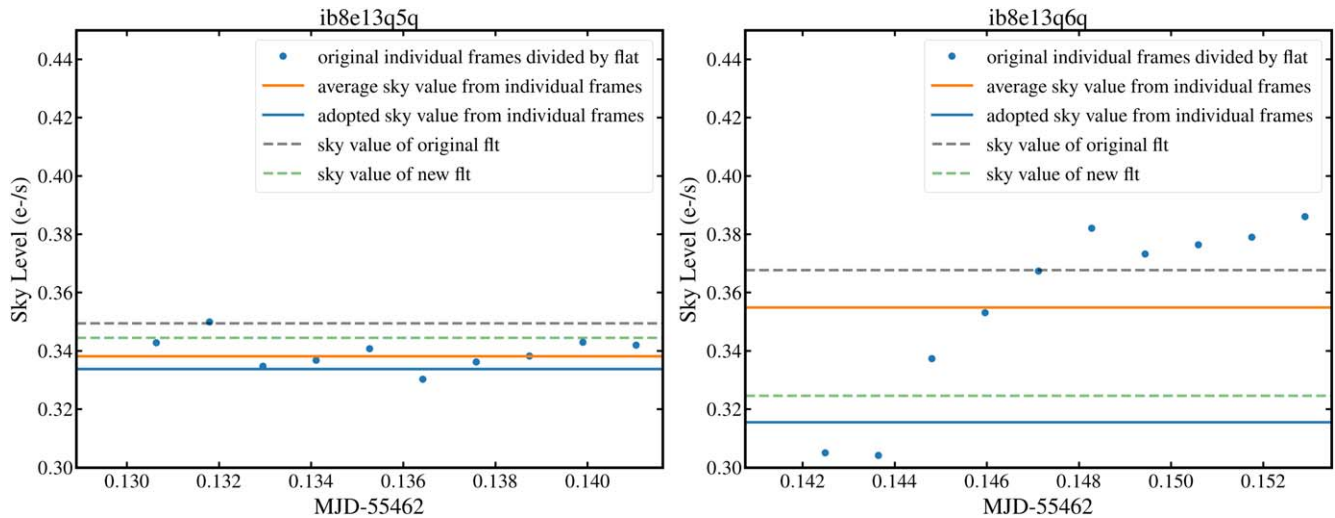


Figure 6. Sky-SB values vs. time in successive half-orbit HST WFC3/IR F125W exposures of a given high ecliptic latitude target. The file names on top indicate the WFC3/IR exposures shown. (a) Left: sky-SB values vs. time at the start of this orbit, which typically uses the darker part of the orbit, so the sky-SB values do not change much over the total exposure length. Time is expressed as the Modified Julian Date (MJD) from the HST FITS headers. The blue data points show the sky-SB values of individual WFC3/IR ramp reads. The orange line shows the exposure time-weighted average over all ramps. For WFC3/IR, we adopt the average of the three ramps with the lowest sky-SB values (blue line), excluding the initial clearing readouts, which we consider to be the more accurate estimate of the Lowest Estimated Sky-SB (LES) for that exposure (Section 4.2.2). Thus, all frames in the *_ima* file are corrected onto the blue line, and the pipeline is run on the adjusted image. The sky value of the resulting *_flt* image is shown as the green dashed line, compared with the sky value of the original *_flt* image, shown as the gray dashed line (see Section 4.3). (b) Right: WFC3/IR F125W sky-SB values vs. time at the end of a typical HST orbit. The procedures and lines are the same as in Figure 6(a), but the differences are now much larger, because in this second half-orbit WFC3/IR exposure, the sky-SB values increase significantly toward the end of the orbit, due to earthshine, resulting in the downward correction in the final adopted sky-SB value (blue line compared to the orange line). The difference between the two adopted sky-SB levels is consistent to within the error budget summarized in Table 5.

correspondingly less. Hence, SKYSURF does *not* need to make further corrections for WFC3/IR detector count-rate nonlinearity, but we do account for its $\sim 0.5\%$ uncertainty in our error budget below.

WFC3 Dark Current Monitors: The WFC3/IR Dark Current (DC) has been monitored over the years (e.g., Sunnquist et al. 2017a, 2017b, 2019). In particular, these studies show some trends in the measured WFC3/IR DC levels and structure with the four different IR detector quadrants. Also, these studies found trends of the measured WFC3/IR DC levels with telescope temperature and with HST’s of orbital phase (Sun altitude; see Section 4.3 and Appendix A.2.2) during the dark current frame observations. In O’Brien et al. (2022), we study the WFC3/IR quadrant variations in more detail, but find them, in general, to be $\lesssim 0.5\%$, i.e., smaller than most other systematic uncertainties in measuring the sky-SB values (Section 4.2), and hence not requiring additional quadrant-dependent DC corrections. Sunnquist et al. (2017b) suggest that the rms variations in dark current level are $\sim 0.0069 e^-/s$, or $\sim 1\%$ of the typical sky-SB in Figure 1, which is incorporated into the error budget of Table 5.

The fact that the WFC3/IR dark current levels appear to be a function of Sun altitude in Sunnquist et al. (2017b) prompted us to take a closer look at how much of the electronic dark current level is temperature-dependent—e.g., due to temperature variations in the detector A/D converters, as Sunnquist et al. (2017b) suggest—and how much additional thermal dark signal may be caused by HST’s temperature variations across its orbit and as a function of Sun altitude. These aspects are addressed in Section 4.3 and SKYSURF-2 as needed for the current SKYSURF results, and in more detail by Carleton et al. (2022b) and O’Brien et al. (2022), which will include a correction for temperature-dependent dark current variations using the Sunnquist et al. (2017b) prescription.

WFC3/IR Thermal Dark Signal: For the WFC3/IR channel, we need to distinguish between the WFC3/IR dark current and its thermal dark signal. The former is mostly an electronic *current* in the WFC3/IR detector that depends on the temperature of the detector and its read-out electronics, while the latter is caused by Planck blackbody *photons* generated in HST OTA, the WFC3 housing, and the WFC3/IR detector enclosures. We need to have the best possible estimates of both to analyze the sky-SB values measured in WFC3/IR images. We will throughout refer to the WFC3/IR thermal dark signal as the “TD” or “TD signal.” The WFC3/IR TD signal was predicted in Table 7.11 of the WFC3 IHB (Dressel 2012, 2016, 2021), where it is referred to as a “thermal dark current.”

The IR detector dark current is measured rather well out to the WFC3 shutter, which is a WFC3/IR filter slot filled with aluminum. The WFC3/IR TD signal is more uncertain and depends somewhat on the exact thermal history of each HST orbit. Predictions of the thermal dark signal can be made with the Python *synphot* package.²² Tables with thermal foreground levels are incorporated into the *synphot* tool, based on the observed temperatures of the HST optical and instrument components discussed in Appendix A of SKYSURF-2. In summary, our calculations of the WFC3/IR TD signal assume temperatures of the HST primary and secondary mirror of $T \simeq 287$ K, temperatures for the WFC3 pick-off mirror and the corrective optics mirrors inside WFC3 and the IR channel of $T \simeq 273$ K, and temperatures for the two outer enclosures and the one inner cold enclosure holding the WFC3/IR detector of $T \simeq 223$ –173 K, respectively.

²² <https://www.stsci.edu/hst/instrumentation/reference-data-for-calibration-and-tools/synphot-throughput-tables>

To ensure that our sky-SB measurements are properly corrected for TD signal, SKYSURF-2 will conduct sky-SB estimates measurements in the three WFC3/IR broadband filters F125W, F140W, and F160W, and correct all three for the TD signal predicted for the known ambient temperatures of the HST components. Our *synphot* analysis reveals that the predicted TD signal is strongly wavelength-dependent. For the F125W and F140W images, the vast majority of the TD signal comes from the WFC3/IR cold enclosure, and not from the two telescope mirrors plus the five optical-path mirrors inside WFC3, due to their much smaller solid angle as seen from the IR detector—and the fact that their Planck SB is still minimal at the long-wavelength cutoff of these two bluer filters. In the F160W images, the TD contribution from the seven mirrors in front of the WFC3/IR cold enclosure increases significantly. In SKYSURF-2, we will therefore consider a range of plausible TD values given the HST component temperatures discussed in their Appendix A. Depending on the temperature of these HST components, the predicted TD signal may vary by up to 30%. In the F160W filter, this corresponds to $\sim 2.7\%$ of the average sky-SB, which is folded into Table 5.

4.1.5. SKYSURF Zero Points and Zero-point Monitors

For SKYSURF, we need to know HST’s zero points (ZPs) as accurately as possible from 1994 to 2020. Photometric stability over the years is different from photometric calibration or ZP errors. We therefore consider below, in order: (1) photometric ZP definition in the context of PSF wings; (2) the actual photometric zero points; and (3) stability and drifts of photometric ZPs over the years. This is followed by a discussion of ZP specifics for each HST instrument used in SKYSURF.

(1) *Zero-point Definition and ZP Use:* For each of the HST instruments used in SKYSURF, the Data Handbooks and ISRs provide instrumental zero points for an object with a total flux of $1.000 e^- \text{ pixel}^{-1} \text{ s}^{-1}$. These ZPs are usually offered for “compact objects” within radii $r \lesssim 0''.4$, and for an “infinite radius aperture.” Because of the Encircled Energy (EE) curve of the spherically aberration-corrected PSF, the EE-values for point sources decrease from 91% at $r \lesssim 0''.4$ in the F606W filter to $\sim 84\%$ in the F125W, F140W, and F160W filters, due to HST’s broader PSFs at the longer wavelengths. Since the HST EE curves approach 100% enclosed flux for $r \lesssim 6''.0$, the “infinite radius apertures” integrate the total fluxes out to $r \lesssim 6''.0$. For details, we refer to the ISRs by, e.g., Ryan et al. (2016), Deustua et al. (2016), and Medina et al. (2022). Most faint galaxies that SKYSURF detects to $AB \lesssim 26.5$ mag in single ~ 500 sec SKYSURF exposures have half-light radii $r_e \sim 0''.2\text{--}0''.3$ (Section 4.7 and Appendix C), so their total flux is not fully captured by the “compact object” aperture ZPs at radii $r \leq 0''.4$. Hence, to obtain more accurate total magnitudes for slightly resolved faint galaxies, as well as accurate sky-SB levels in the empty image areas (Section 4.2), we will always use the ZPs for “infinite radius apertures” in SKYSURF. For the current SKYSURF study, the “infinite radius apertures” ZPs provide the best absolute sky-SB values. This assumes that, for a given sky-pixel and constant sky-SB, the HST PSF will leak as much flux into neighboring pixels as the neighboring pixels will leak into that pixel.

(2) *Photometric Zero Points:* The instrument ZPs are derived from white dwarf standard star observations, which for most filters can be done to $\sim 1\%$ accuracy (e.g., Bohlin et al. 2020).

The ACS/WFC and WFC3/UVIS and IR instrument zero points have been stable to $\sim 1\%$ – 2% (Kalirai et al. 2010; Dressel 2016, 2021; Ryon 2022) with the caveats discussed below, allowing their use as *absolute photometers*. When comparing results from very similar broadband filters in different instruments, small corrections for differences in central wavelength may need to be applied (see, e.g., Figure 2(a) here; W11, D16; and the ICRAR zero-point transformation tool (Koushan et al. 2021)²³). This is relevant when doing counts of the objects over a wide dynamic range in similar filters from different instruments. Details on the filter zero points and aperture corrections needed for faint object fluxes and faint object counts are provided by Tompkins et al. (2022).

(3) *ZP Stability and Drifts over the Years:* We need to monitor and carefully account for panchromatic WFPC2, ACS/WFC, and WFC3/UVIS and IR zero-point changes versus time, some of which may be due to modest accumulation of contaminants onto the HST optics and in each camera over 11–18 yr. This is especially true for the HST WFC3/UVIS ultraviolet filters F225W, F275W, and F336W. We discuss the relevant ZP details for each of the cameras below.

WFPC2: WFPC2’s Archival data spans over 16 yr (1994–2009) with photometric zero points stable to within $\sim 2\%$ – 3% (Holtzman et al. 1995), and $\sim 1\%$ – 2% in F439W and redward. The WFPC2 photometric zero points are taken from Table 10 of Holtzman et al. (1995), using their Equation (9). Section 5.7 and Table 5.10 of the WFPC2 Data Handbook²⁴ summarize the end-of-mission uncertainties in the WFPC2 calibration aspects and time-dependent zero-points, which are summarized in Table 5. The WFCP2 *ATODGAIN* was read from the FITS header, and the appropriate gain ratio from Holtzman et al. (1995) was applied to correct the zero points for the different CCDs to AB-magnitudes.

ACS/WFC: The STScI ACS group has monitored the ACS zero points since its 2002 Shuttle launch on Servicing Mission 3 (SM3B). True ACS zero-point changes are smaller than $\sim 1\%$ – 2% , with drifts on the order of $\sim 0.1\%$ – 0.2% per year. SKYSURF uses the ACS zero-points website,²⁵ which provides this up-to-date information as a function of observing date. We use these time-dependent functions to determine the best zero points for the observation dates for all ACS/WFC images. From the scatter in the time-dependent zero points in Figure 2 of Bohlin et al. (2020), we will conservatively take this ZP trending to be no better than $\sim 1\%$ in accuracy, which is incorporated in the error budget of Table 5.

WFC3/UVIS: STScI has also monitored the WFC3/UVIS zero-point changes since its 2009 Shuttle launch on SM4 (e.g., Deustua et al. 2016; Ryan et al. 2016; Bajaj 2019; Calamida et al. 2021). Long-term WFC3 zero-point changes can amount to $\sim 3\%$ (Ryan et al. 2016), but are in part due to definition changes in the *calwf3* pipeline. True WFC3 zero-point changes are smaller than this, with drifts on the order of $\sim 0.1\%$ – 0.2% per year (Calamida et al. 2021). SKYSURF uses the WFC3/UVIS zero-points websites,²⁶ which provide this

²³ <http://transformcalc.icrar.org>

²⁴ https://www.stsci.edu/instruments/wfpc2/Wfpc2_dhb/wfpc2_ch53.html#1920857

²⁵ <http://acszeropoints.stsci.edu>

²⁶ <https://www.stsci.edu/contents/news/wfc3-stans/wfc3-stan-issue-33-october-15>, and <https://www.stsci.edu/hst/instrumentation/wfc3/data-analysis/photometric-calibration/uv-vis-photometric-calibration>.

up-to-date information. In particular, Calamida et al. (2021) summarize well-sampled time-dependent zero-point changes for most WFC3/UVIS filters from 2009 to 2019. For the WFC3/UVIS UV filters with central wavelengths below 300 nm, the ZPs show an increase in sensitivity of $\sim +0.5\%$ yr^{-1} for the first two years, followed by a slowly declining sensitivity over time in subsequent years. All filters redward of F300X have seen a slow, nearly linear and somewhat wavelength-dependent decline in ZP sensitivity over time, with well-determined slopes that typically range between -0.1% yr^{-1} to -0.2% yr^{-1} . For example, for the most-used WFC3/UVIS F606W and F814W filters (Table 2(b)), this steady decline in ZP amounts to about -1.8% and -1.0% over 11 yr, respectively. The linear fits of the Calamida et al. (2021) zero-point drifts have rms errors of $\sim 0.5\%$, and provide the best available data on the time-dependent WFC3/UVIS zero points as of 2021. To implement these slowly time-dependent ZPs as a function of wavelength and time, we therefore downloaded the WFC3/UVIS images again in early 2022 with `calwf3` pipeline version 3.6.2 on AWS, which updated all FITS headers with the proper time-dependent ZPs. For details of this process, we refer to O’Brien et al. (2022). The resulting WFC3/UVIS ZP errors as a function of time are estimated to have a $\sim 1\%$ accuracy, as listed in Table 5.

WFC3/IR: The WFC3/IR photometric zero points have roughly remained constant to within $\sim 1.5\%$ (rms) in the 10 yr after its SM4 launch without a noticeable time-dependent decline (Figure 7 of Bajaj 2019), unlike those of WFC3/UVIS. Some of the $\sim 1.5\%$ scatter is due to residual persistence, which with proper dithering and drizzling can be further reduced (Bajaj 2019). We will therefore take the error in the WFC3/IR broadband ZPs to be $\sim 1.5\%$ in Table 5. The WFC3/IR ZPs used in the F125W, F140W, and F160W filters are 26.232, 26.450, 25.936 AB-mag, respectively, for an object with $1.000 e^- \text{pixel}^{-1} \text{s}^{-1}$.²⁷

4.1.6. Sky-SB Error Budget Thus Far

Table 5 summarizes the error budget for WFPC2, ACS/WFC, WFC3/UVIS, and WFC3/IR resulting from the considerations in Sections 4.1.1–4.1.5 and 4.2. For the WFC3/IR filters F125W and F140W, the total relative error is $\sim 2.7\%$ – 2.8% of the average sky-SB level, while for F160W it is $\sim 3.8\%$, which is indicated by the brown horizontal short-dotted line in Figure 1. The dominant sky-SB errors in Table 5 are *multiplicative* in nature, i.e., the global flat-field and photometric zero-point errors. Because of the way the flat fields and photometric zero points are created, these two main relative error sources are independent, so adding them in quadrature is justified. O’Brien et al. (2022) present a comparison between the ACS, WFC3/UVIS and WFPC2 sky-SB measurements over 26 yr (e.g., $\sim 49,000$ images in the F606W filter alone), enabling them to confirm our relative errors in Table 5 and— together with the WFC3/IR data—compare SKYSURF’s sky-SB values to panchromatic zodiacal models.

The predicted WFC3/IR thermal dark signal error is modest in the F125W and F140W filters, but increases significantly for the F160W filter SKYSURF–2, and therefore becomes a dominant *additive* error in the F160W sky-SB estimates. For

this reason, the bottom two rows of Table 5 list *both the lowest and the average* sky-SB values plus the total errors for each in units of $nW m^{-2} sr^{-1}$ for the WFC3/IR F125W, F140W, and F160W filters, respectively. For the *darkest* sky-SB values, the percentage TD error is about $2\times$ larger than the errors quoted for the *average* sky-SB values, increasing the total errors for the darkest sky-SB values to $\sim 2.8\%$, $\sim 2.9\%$, $\sim 6.3\%$ in the F125W, F140W, and F160W filters, respectively. In SKYSURF–2, we will consider *both the darkest and average sky-SB values* in these filters, and will therefore propagate the errors of Table 5 accordingly into our results. SKYSURF–2 includes a method to avoid images with significant stray light for sky-SB estimates, which will have its own error considerations.

4.2. Optimal Object-free Sky-SB Estimates in All Individual SKYSURF Exposures

A critical part of SKYSURF is measuring the sky-SB in between the discrete objects as accurately as possible. For this, we introduce in the next subsections different algorithms to estimate the sky-SB as well as possible in-between discrete objects, which are primarily faint galaxies, Galactic stars, and CRs. To test these algorithms, we check them against simulated images with *known input* sky-SB values, as well as realistic distributions of galaxies, stars, and CRs. Here, we summarize how those simulations were done, how sky-SB measurements were made with different algorithms, and how these were verified. Details of these WFC3/IR image simulations and all nine SKYSURF methods used to estimate the sky-SB are given in O’Brien et al. (2022).

4.2.1. Simulation of Images with Known Sky-SB and Realistic Cosmic-ray, Star, and Galaxy Counts

Following the observed panchromatic galaxy and star counts of Windhorst et al. (2011), we generated 784 simulated WFC3/IR F125W images with *known input* sky-SB values, and realistic surface densities and magnitude distributions of stars and galaxies. The 784 simulated images cover the range of expected sky-SB values, given the exposure time distribution in WFC3/IR F125W of Figure 5. For about half the images, we include the expected increase in sky-SB and its resulting sky gradient in typical HST exposures toward the Earth’s limb at the end of each HST orbit, as discussed in Section 4.3.

The *total* AB-magnitudes of both the imposed galaxy and star counts use the same WFC3/IR F125W AB-mag zero point as in Section 4.1.5 for an object with $1.000 e^- \text{pixel}^{-1} \text{s}^{-1}$. The simulated stellar and galaxy profiles are broadened with the WFC3 PSF, while the galaxy profiles also have the ellipticity distributions superimposed as observed for faint galaxies (Odewahn et al. 1997). Finally, the images add a *known* sky-SB and corresponding rms sky-noise level. A variety of zodiacal sky-SB levels are used with a range of sky-SB $\simeq 0.628$ – $3.14 e^- \text{pixel}^{-1} \text{s}^{-1}$ for the range of exposure times of $t_{\text{exp}} \simeq 50$ – 1300 s. Following the instrument parameters in Table 7.11 of the WFC3 IHB (Dressel 2021), the rms noise includes the sky noise of the imposed zodiacal sky level, the WFC3/IR read noise, and dark current noise. Including all of these yields a typical simulated WFC3 F125W signal of $\sim 1.1 e^- \text{pixel}^{-1} \text{s}^{-1}$, such that an average 500 s WFC3/IR exposure has a total imposed sky level of $\sim 556 e^-$ with an rms noise of ~ 23 – $24 e^-$.

²⁷ <https://www.stsci.edu/hst/instrumentation/wfc3/data-analysis/photometric-calibration>, <https://www.stsci.edu/hst/instrumentation/wfc3/data-analysis/photometric-calibration/ir-photometric-calibration>, see also <http://svo2.cab.inta-csic.es/svo/theory/fps3/index.php>

In total, 784 WFC3 images were simulated by two independent teams, one following the above analytical galaxy image description that is based on well-defined statistical properties of real WFC3 images (e.g., Windhorst et al. 2011), while the other team used *real* WFC3 galaxy parameters as observed in CANDELS and 3DHST (van der Wel et al. 2012; Skelton et al. 2014). The latter method automatically produces the observed size distribution of Section 4.7 and the observed b/a distribution of Odewahn et al. (1997), so these parameters did not need to be imposed by the second team. These images look realistic, with the exception that real HST images show galaxies that are more irregular than the exponential disk or generalized Sérsic light profiles. We validated our simulations by running the star-counts and galaxy counts on these images following the procedures described in Section 4.7 and Appendix C, and concluded that the required surface densities, count slopes, and galaxy size and b/a distributions were imposed correctly. This set of simulated WFC3/IR images with *known* input sky-SB levels was subsequently analyzed by *different* independent teams that assessed which algorithms most closely recover the *known* input sky-SB levels. This provides the proof of concept that SKYSURF can measure the sky-SB levels in between the discrete objects accurately, independent of their actual cause.

4.2.2. SKYSURF Algorithms to Obtain the Lowest Estimated Sky-SB in Each Exposure

SKYSURF’s specific goal is to measure the Lowest Estimated Sky-SB in each image that is not due to a statistical variation nor image defects, but is closest to the true sky-SB that SKYSURF intends to constrain. Throughout, we will refer to this Lowest Estimated Sky-SB level as the “LES” or the “LES method.” In object-free areas of SKYSURF images taken during the darkest part of each HST orbit, the LES level will be as close as HST can measure to the true ZL+DGL+EBL level in that direction and time of the year. This is because all contaminating signals outside the HST instruments (e.g., earthshine, scattered Sun and Moon light) add as a positive signal—only some of the instrument calibration errors in Section 4.1 could add a dim negative signal to the images. Hence, SKYSURF needs to find this LES level in each filter in each direction of the sky, accounting also for the angles of the Earth’s limb, Moon, and Sun at that time, and flagging images that may have higher stray-light values, as discussed in Section 4.3.

Several different teams developed independent sky-SB estimation methods to recover the sky-SB levels imposed in the simulated images by the two separate teams in Section 4.2.1. These sky-SB estimation teams had *no* knowledge of the actual sky-SB levels imposed by the two independent simulation teams. The only aspects of which they were made aware were that the simulated images had a plausible range of sky-SB levels and exposure times (Figure 5), surface densities of Galactic stars, galaxies with size and ellipticity (b/a) distributions, as well as CR distributions. This process can be easily expanded to include ACS/WFC, WFC3/UVIS, or WFPC2 filters and pixel scales, to check on the wavelength dependence of the reliability of our algorithms that estimate the sky-SB using the LES method.

A total of nine methods were created to estimate LES levels in each image, each taking a different approach in identifying the best algorithm to use on real SKYSURF images (Figure 7).

These methods vary in their approach: some calculate a clipped mean, while others incorporate the `PROFOUND` (Robotham et al. 2017) package, which was designed to robustly create an interpolated sky-SB map from an image. Several of the methods in Figure 7 attempt to estimate the sky-SB by taking into account that the sky-SB might vary across a single image, i.e., indicating the presence of a sky-SB gradient (Sections 4.3–4.4).

In several of the methods, SKYSURF accomplishes this by dividing each 1014×1014 pixel WFC3/IR image into a 26×26 grid of square subregions or boxes that contain 39×39 pixels each. Every box thus contains 1521 pixels, which is sufficient to make an estimate of its own sky-SB value accurate to $\sim 2.6\%$ (i.e., $1/39$) of the sky-rms value in that box if it contained no objects or image defects, that is, if the sky in that box were truly featureless and flat. Next, we implemented a procedure that excluded boxes based on their rms value or the number of pixels flagged in the data quality extension of the image, which identifies bright or faint objects or known defects in that box. The green boxes in Figure 7 represent the lowest 5% values of the *total* grid of boxes that was used to estimate the LES values in each image, i.e., those without detectable objects. We emphasize that our LES method does not look at the lowest 5% of all pixel values in each WFC3/IR image, an estimate that would certainly be biased to be well below the true image mode or peak. Instead, the LES method uses the lowest 5% of all boxes that were selected to not contain barely detectable faint objects, bright object outskirts, and/or image defects. We show in Section 4.2.3 that using this 5% threshold of all boxes with the lowest sky-SB values most accurately recovers the known input sky-SB values from the simulations in Section 4.2.1.

In SKYSURF-2, we use the best of these algorithms to estimate the LES values for all 34,400 WFC3/IR images in the F125W, F140W, and F160W images in Table 3. To check if the distribution of the green boxes in Figure 7 showed any noticeable correlation with the GDC structure across the detector, we collapsed the green boxes from all 34,400 WFC3/IR images into one 26×26 density grid. The WFC3/IR detector is on HST’s optical axis, and due to its $\sim 24^\circ$ tilt about its x -axis, its pixels each cover a somewhat rectangular area of the sky, with a $\pm 4.5\%$ GDC variation that stretches mostly along the y -axis (see, e.g., Figure B.3 of Dressel 2021). The average locations of the green boxes to estimate LES sky-SB values across 34,400 exposures showed *no* correlation with the GDC structure across the detector. Nor did they avoid the “fiducial point” in the WFC3/IR center, where the GO user is recommended to place their small targets, suggesting that the average GO observer uses WFC3/IR more as a survey instrument than for individual (large) object imaging. In summary, the green boxes in Figure 7 sample the LES values rather randomly across the detector when considering all 34,400 WFC3/IR exposures. This then justifies the sky-SB estimation in the undrizzled flat-fielded `_flt/_flc` images (Section 4.1). We will henceforth assume that the LES method estimates the lowest sky-SB in each exposure well enough to proceed.

4.2.3. Algorithm- and Scene-dependent Reliability of Recovered Input Sky-SB

Here, we summarize the main algorithmic results and discuss the best algorithms to estimate the lowest estimated sky-SB in

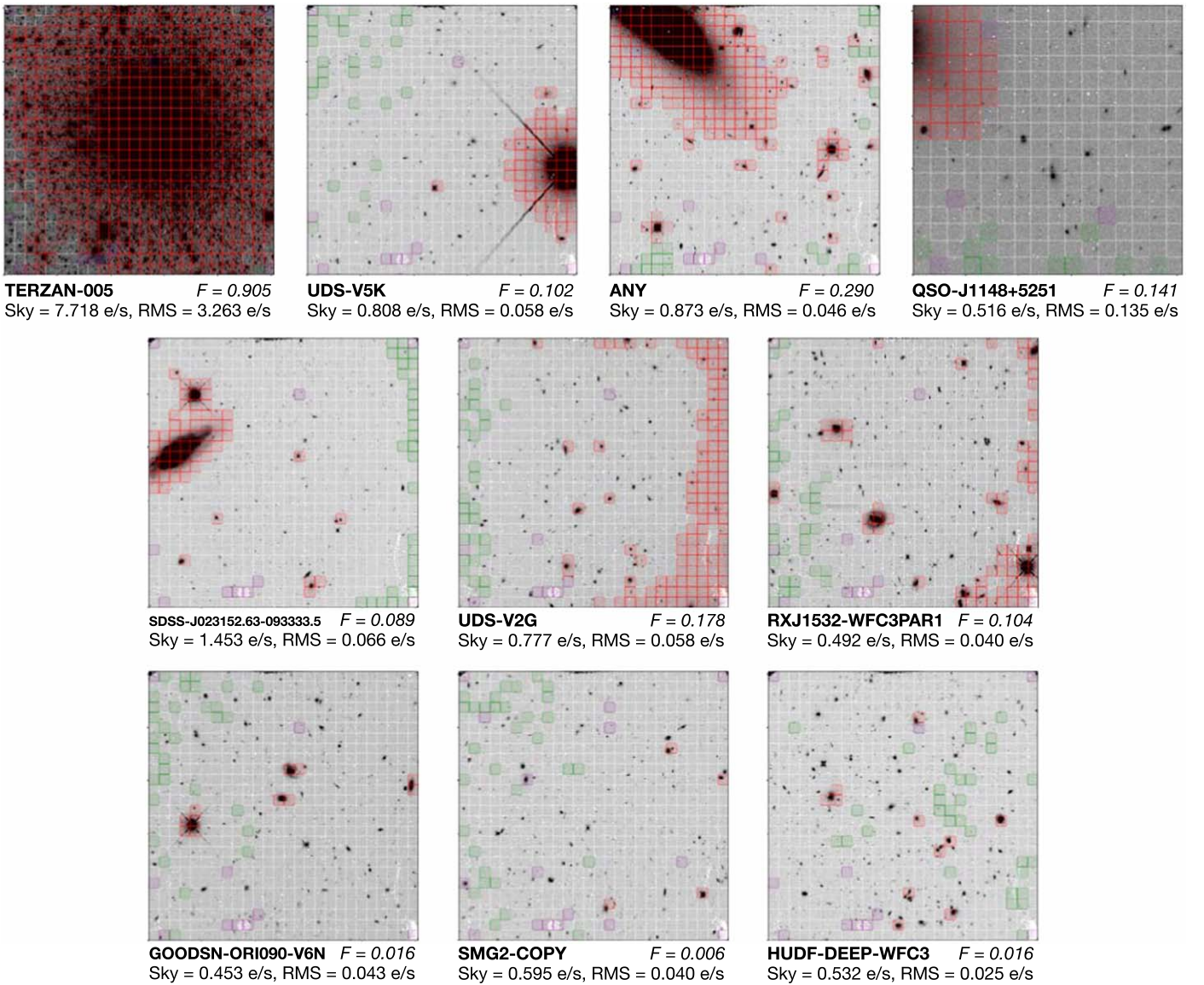


Figure 7. Examples of the robust HST sky-SB estimator (Sections 4.2.2–4.2.3) applied to a sample of WFC3/IR F125W images. Purple boxes indicate cells not used in the sky-SB determination because they contain bad pixels, and red boxes indicate cells not used because the object finder identified these cells as affected by a bright object or its outskirts. The remainder boxes are used to determine the sky-SB in each image, while green boxes represent the lowest 5% values of the boxes that were used to estimate the LES values in each image, which are defined in Section 4.2.2. The HST target name is given in each case, as well as the fraction F of total boxes flagged as red, plus the sky-SB and its rms values in the nonflagged areas. The top row shows images that are substantially covered and affected by large objects such that, at best, only the opposite image sides or image corners can be used to estimate the LES value in that image, which still may have higher sky-SB than the true ZL+DGL+EBL in that direction of the sky. The middle row shows examples of images with measurable low-level gradients. The bottom row of images shows relatively empty fields, where SKYSURF’s LES value is less biased by large discrete objects and may be closer to the ZL+DGL+EBL level, as discussed in Section 4. This robust automated sky-SB estimation algorithm for WFC3/IR is also adapted for ACS/WFC, WFC3/UVIS, and WFPC2 images, and is essential to make SKYSURF’s sky-SB estimates across the sky.

the absence and presence of sky-SB gradients. By implementing the filtered gridding method of Section 4.2.2, we are also able to indirectly detect gradients across an image. We flag and remove subregions that are brighter than the mean sky-SB level + the mean sky-SB rms level, then remove images where more than 30% of subregions are flagged as non-sky regions. We show a comparison of the results from these nine methods in Figure 8.

In the *absence* of sky gradients, panels (a) and (c) of Figure 8 show that method 3 (based on histogram fitting; yellow triangles), and methods 8 and 9 (based on ProFound-catalogs; Robotham et al. 2017, green and blue squares) generally provide measured sky-SB levels to well within 0.2%

from the known input values. In methods 8 and 9, the simulated sky-SB values are best recovered when the *lowest 5% of the sky boxes’ SB values are used as an estimator*. Method 4 (based on SourceExtractor-catalogs; purple diamonds) performs worse at sky levels with lower signal-to-noise ratios. For methods 8 and 9, the $|\text{observed} - \text{simulated}|$ difference is as small as $\sim 0.1\%$, as long as the WFC3/IR sky-noise is $\lesssim 0.24 e^- \text{pixel}^{-1} \text{s}^{-1}$ (i.e., $t_{\text{exp}} \geq 200$ sec for its broadband filters).

In retrospect, the resulting $\sim 0.1\%$ accuracy of estimating the known input sky-SB values with the best algorithms makes sense. In Section 4.2.2, we estimated that, in the best possible case of a clean flat sky over an entire image, each of the 676 boxes of 1521 pixels could estimate its sky value to an

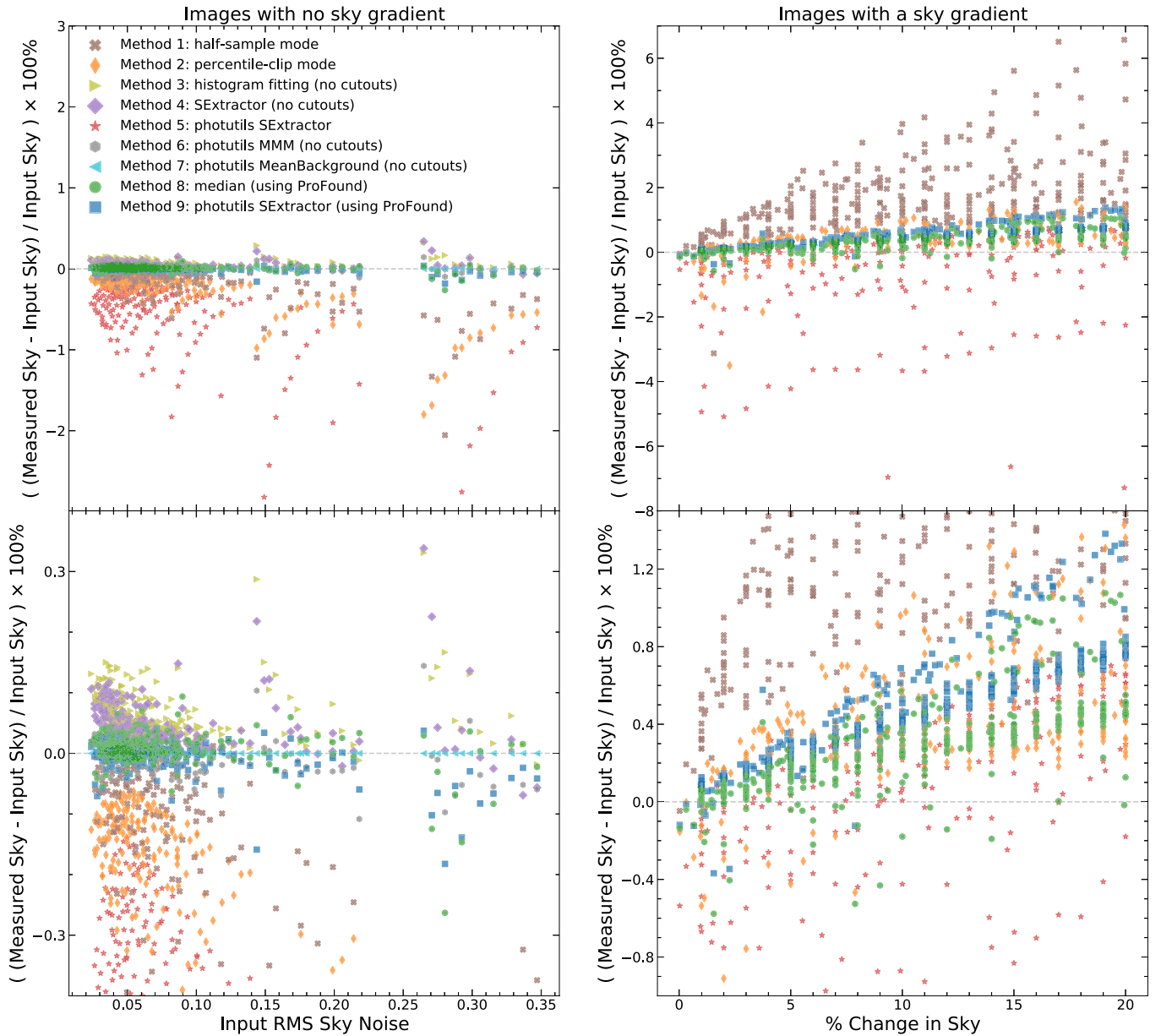


Figure 8. In the left panels, the bottom panel (c) is an enlargement of top panel (a). These panels present a systematic comparison of our nine independent sky-SB measurement methods against the known inputs from 784 simulated WFC3/IR F125W images, with known sky-SB levels and realistic CR levels, star counts, and galaxy counts superimposed. Methods 8 and 9 that are based on ProFound (green and blue-filled squares) generally provide measured sky-SB levels that differ $\lesssim 0.1\%$ – 0.2% from the known simulated input values, as long as the WFC3/IR sky noise is $\lesssim 0.24 e^- \text{pixel}^{-1} \text{s}^{-1}$, i.e., exposures with $t_{\text{exp}} \geq 200$ s in the broadband filters. In the right panels, the bottom panel (d) is an enlargement of top panel (b). These panels are similar to panels (a) and (c), but simulating images with up to 20% sky-SB gradients corner-to-corner or edge-to-edge. These simulated image gradients are in excess of any gradients expected in the zodiacal light on arcmin scales (Section 4.2.3). For images with gradients that are 5%–10% of the lowest sky-SB value, methods 8 (which uses medians based on ProFound) and 9 (Photutils using SourceExtractor and ProFound) provide measured sky-SB levels that are generally within 0.4% from the simulated input values when the gradients are $\lesssim 10\%$, and within 0.2% from the input values when the gradients are $\lesssim 5\%$ corner-to-corner or edge-to-edge across the simulated image.

accuracy of 2.6% of the sky-SB in that box. For a perfectly flat sky, these methods may thus recover the input sky-SB to no better than $2.6\% / \sqrt{676} \simeq 0.1\%$ of the input sky value. This is indeed about the best accuracy at which methods 8 and 9 recover the known input sky-SB values in Figures 8(a) and (c).

Figures 8(b)–(d) show that, in the presence of simulated sky-SB gradients that amount to 10%–20% of the lowest sky-SB value edge-to-edge, method 8 provides measured sky-SB levels generally within $\sim 0.4\%$ from the simulated input values when the gradients are $\lesssim 10\%$, and within $\sim 0.2\%$ when the imposed sky-SB gradients are $\lesssim 5\%$ edge-to-edge or corner-to-corner. These simulated image gradients are in excess of any gradients

expected in the ZL on arcmin scales. Significant gradients with amplitudes $\gtrsim 10\%$ can be caused in real HST images by: (a) stray light (Section 4.3); (b) large artifacts; or (c) large targeted objects with real astrophysical gradients (Appendix B.3). SKYSURF flags images with strong gradients or large targets or artifacts, estimates their LES values (at lower accuracy) to help diagnose these causes of stray light and stray-light gradients, and where needed, discards them for sky-SB analysis or object counts.

In conclusion, the histogram-fitting method 3 provides LES sky-SB values with the simplest algorithm available that is accurate to within $\sim 0.2\%$ in SKYSURF images *without*

gradients (Figure 8(c)), but it is not proven in the presence of strong gradients. The percentile-clip method 2 works better in the presence of gradients, but has larger errors ($\lesssim 0.3\%$) in images without gradients. Hence, in the first science analysis of SKYSURF-2, we will use method 3 and discard images with higher sky-SB levels and significant gradients. Methods 4, 8, and 9 are considerably more CPU-intensive, since they require complete SourceExtractor or ProFound object catalogs to be made in advance. Overall, method 8 can provide the most accurate LES sky-SB values to within $\sim 0.1\%$ in SKYSURF images *without gradients*, and to within $\sim 0.2\%$ – 0.4% in images with gradients that are less than 5%–10% edge-to-edge or corner-to-corner, respectively. This method will be applied to all individual SKYSURF images in O’Brien et al. (2022), which requires the entire SKYSURF database to be processed with ProFound.

4.3. Orbital Sky-SB Dependence and Possible Sources of Stray light

We define our usable sample of SKYSURF images as a function of orbital parameters that may affect the measured image sky-SB values: Limb Angle (LA), Moon Angle (MA), Sun Angle (SA), Sun altitude α_{\odot} above the Earth’s Limb, the Illuminated Earth Fraction (IEF), HST’s Roll Angle (RA), and HST’s position in the Continuous Viewing Zone (CVZ). The MA and SA are defined as the angular distance between the HST pointing direction and the center of the Moon or Sun during the exposure, respectively. Sun altitude α_{\odot} is defined as the Sun–Earth–HST angle, which determines the amount of sunlight scattered off the bright Earth that can reach the HST aperture. SKYSURF does ephemeris and visual checks to identify images that got too close to: (a) the Earth’s limb, including those taken at the bottom of the CVZ, (b) the Sun; and/or (c) the Moon. Any one of these can corrupt the sky-SB measurements, and in some cases also the SKYSURF source catalogs. Some but not all of this information is available in the HST Engineering telemetry data, i.e., the “*jit*” files that come with the raw FITS images. Where needed, we compute the parameters LA, MA, SA, and α_{\odot} for each SKYSURF exposure. Appendix A.1 gives details on how the HST orbital parameters have been calculated at any given time since its 1990 April 24 launch or its subsequent Shuttle Servicing Mission reboosts. In our current analysis, only sky-SB measurements from images with sufficient blank sky are used for the final SKYSURF analysis (Section 4.2).

A full ray-tracing of the HST stray light from first principles is beyond the scope of the SKYSURF project, and so we start with an *empirical* approach to trace the sky-SB measurements as a function of the orbital parameters LA, MA, SA, and α_{\odot} , and define the ranges in these parameters where the SB-measurements are generally not significantly enhanced above the minimum in each direction, as described in Caddy & Spitler (2021). For the 249,861 ACS+WFPC2+WFC3 images, we calculate these angles and identify the angle ranges that may have resulted in enhanced stray light levels. Such exposures may still be usable for panchromatic object counts, in which case they are used in our modified drizzled pipeline (Section 4.6).

Some examples are shown in Figures 6(a) and (b). Here, Figure 6(a) shows the WFC3/IR F125W sky-SB values of the first half-orbit exposure at the start of an orbit, which typically uses the darker orbital part, so that the sky-SB values do not

change much over the total exposure length. The blue data points show the sky-SB values of *individual WFC3/IR ramp readouts* as estimated with the best algorithms in Section 4.2.3. The orange line in Figure 6(a) shows the exposure time-weighted average over all ramps. The default calwf3 calibration procedure of this exposure uses all these values, which results in the gray dashed line as the sky-SB value of the final *_flt* file, which is biased by the ramps with the highest sky-SB. When we run this through calwf3, we find the green dashed line as the sky value of the final *_flt* file, which still does not reflect the lowest possible sky-SB value for that exposure well. For WFC3/IR, we therefore adopt the average of the *three* ramps with the lowest sky-SB values (blue line), excluding the initial clearing readouts. We consider the blue line to be the more representative value of the lowest estimated sky-SB for that exposure.

Figure 6(b) shows the WFC3 F125W sky-SB at the end of a typical HST orbit, which in this case is the second half-orbit exposure observed directly after the one shown in Figure 6(a). The procedures and lines are the same as in Figure 6(a), but the differences are now much larger because, in this second half-orbit WFC3/IR exposure, the sky-SB values increase significantly toward the end of the orbit, due to earthshine. The resulting blue line indicates the final adopted sky-SB value compared to the calwf3 average (orange line). Over the course of this orbit, the dispersion of our reprocessed *_flt* sky-SB values is smaller than the dispersion in the original *_flt* sky-SB values, so our procedure results in more consistent estimates of the lowest estimated sky-SB than the default calwf3 pipeline.

The GOODS-North data of Giavalisco et al. (2004) were used as an initial case study to investigate the sky-SB in HST images as a function of the orbital parameters, and to reduce the impact on sky-SB measurements of: (a) earthshine due to the proximity of the Earth’s limb; (b) the Sun altitude above the Earth’s limb, to minimize sunlight scattered off the bright Earth; (c) the Moon; and (d) the Sun during each exposure, to minimize their stray light. The data and model predictions are shown together with their uncertainty wedges in Figure 9. Details are given in Caddy & Spitler (2021), Caddy et al. (2022), and Appendix A.2. The ACS F850LP-filter data in GOODS-North were chosen for this study because: (1) it is the closest filter in central wavelength to the WFC3/IR filters used to present our first SKYSURF results; (2) the high ecliptic latitude ($b^{\text{Ecl}} \simeq 57^\circ$) of GOODS-North reduces the impact of true ZL variations on the analysis; and (3) its very large sample size. These data consist of sky-SB measurements from 1018 ACS F850LP images in the GOODS-North field, which is in HST’s CVZ and covers a range of Earth limb angles, Sun altitudes, Sun angles, and Moon angles recorded in the HST telemetry data. Only exposure times in the range of 240–1800 s were used for this study.

In Figures 9(a)–(d), the measured sky-SB values are colored by orbital parameters that meet the SKYSURF criteria for avoiding stray light contamination. Black points are exposures that do *not* meet our criteria, and red points are those that do. In summary, the *combined boundaries in orbital parameters that yield the darkest sky-SB values* as indicated by the red points are: (a) Earth’s LA $\gtrsim 30^\circ$ – 40° , to avoid earthshine; (b) Sun altitude above the Earth $\alpha_{\odot} \lesssim -10^\circ$ (i.e., orbital night side), to minimize sunlight scattered off the bright Earth; (c) Moon

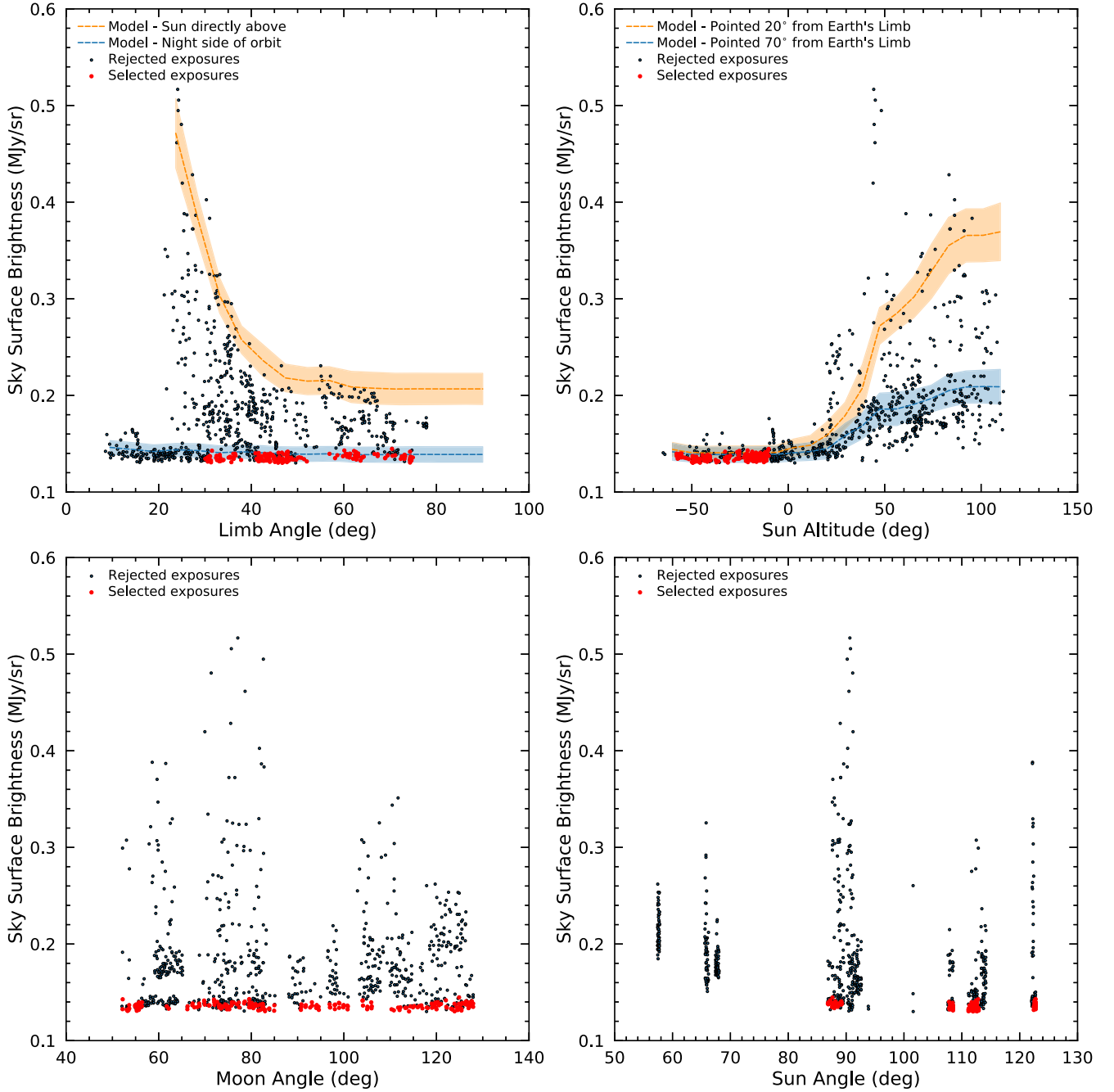


Figure 9. Combined boundaries in orbital parameters that yield the darkest sky-SB values (red points) as defined using the GOODS-North ACS F850LP data set of Section 4.3 and Appendix A.2. (a) Top Left: total sky-SB vs. Earth’s limb angle. The orange model shows the elevated sky-SB due to earthshine for Sun altitude $\alpha_{\odot} \simeq 90^{\circ}$ on the orbital day side with Sun angle fixed at $SA \sim 90^{\circ}$. A strong exponential increase is seen for $LA \lesssim 40^{\circ}$ – 45° , but even fields with $LA \lesssim 70^{\circ}$ – 80° on the day side can have an elevated sky-SB. The blue line plus uncertainty wedge indicates the Caddy & Spitler (2021) model on the night side for $\alpha_{\odot} \simeq -10^{\circ}$, and shows a marked decrease in sky-SB. (b) Top Right: sky-SB vs. Sun altitude α_{\odot} . The orange and blue models show that lower LAs result in steeper relationships for $\alpha_{\odot} \gtrsim 10^{\circ}$ – 20° . For $\alpha_{\odot} \lesssim -10^{\circ}$, the sky-SB is lowest and remains approximately constant. (c) Bottom Left: sky-SB vs. Moon angle. For $MA \gtrsim 50^{\circ}$, the Moon angle is not a major driver of stray light. (d) Bottom Right: sky-SB vs. Sun angle. The large scatter for each Sun angle cluster is primarily due to the variation in Sun altitude and limb angle for each exposure. The minimum estimated sky-SB closest to the true ZL+DGL+EBL level is reached for observations that combine: $LA \gtrsim 30^{\circ}$, $\alpha_{\odot} \lesssim -10^{\circ}$, $SA \gtrsim 80^{\circ}$, and $MA \gtrsim 50^{\circ}$ (red points).

angle $MA \gtrsim 50^{\circ}$; and (d) Sun angle $SA \gtrsim 80^{\circ}$, to avoid stray light into the HST optics, respectively.

Imposing these constraints as detailed below, the standard deviation of the GOODS-N sky-SB values is reduced from 0.055 to 0.002 MJy sr⁻¹, with an overall decrease in mean sky-SB of 0.138–0.179 MJy sr⁻¹, respectively. These selection criteria can thus minimize the impact of earthshine, Sun

altitude, Sun angle, and Moon angle on the HST’s sky-SB measurements. These limits are more extreme than those recommended by the HST Instrument Handbooks, and we impose them on all our panchromatic sky-SB estimates for ACS/WFC, WFC/UVIS and WFC/IR that subselect HST’s orbital phases with the lowest stray light (O’Brien et al. 2022). Further details on stray light resulting from the Earth’s Limb,

the Sun altitude above the bright Earth, and the Sun angle with respect to HST’s pointing direction, as well as the Moon angle, are given in Appendix A.2.

4.4. Definition and Strategy for Treatment of Sky-SB Gradients

We need to estimate and preserve the LES level in all SKYSURF images for subsequent sky-SB analysis. This is currently *not* the default option in AstroDrizzle²⁸ (Avila et al. 2015). Hence, we run AstroDrizzle on the entire SKYSURF database, with the *LES sky-SB preserved* in each sequence of observations in a given filter that was taken in the same visit. HST exposures can have low-level gradients if they were pushed too close to the Earth’s limb, or if they were taken at too small Moon angles or Sun angles. An example is given in Figure 6(b). AstroDrizzle normally removes a gradient surface before drizzling, using the `MDRIZSKY` keyword that preserves the sky, so the subtracted sky level or sky surface can be reinstated. We use `ProFound` (Robotham et al. 2017) to map low-level gradients with spline surface fits to the sky-SB in between all discrete objects detected in the SKYSURF images, preserving the spline surfaces in separate FITS files for later diagnostics. In this process, we subtract the gradient from the `ProFound` surface, but *not* the lowest reliable DC level of the sky-SB, as that is one of the key parameters SKYSURF is measuring. Details are given by Tompkins et al. (2022).

Images at low Galactic latitude ($b_{\text{II}} \lesssim 30^\circ$), or images of large bright-object targets, such as Galactic star formation regions and the outskirts of nearby galaxies, may have real astrophysical gradients in their sky-SB, due to substantial DGL. In that case, any gradient must not be removed (e.g., the top right two panels in Figure 7). This is monitored and flagged by SKYSURF (blue column in Figure 3), with feedback to the SKYSURF SB-measurements and drizzling database and input from the LA, MA, and SA monitoring in Section 4.3, to help identify which images at $|b_{\text{II}}| \lesssim 30^\circ$ may be dominated by DGL or by large bright-object targets, and not by orbital stray light.

4.5. Definition of SKYSURF Drizzle Families and Drizzle Footprints

SKYSURF drizzles *all* images to the same pixel scale of $0''.060 \text{ pixel}^{-1}$, including the single exposures, to provide proper photometry for both sky-SB measurements and discrete object catalogs (Section 4.1). This includes the latest practices in AstroDrizzle for the identification and masking of CRs and Charge Transfer Efficiency (CTE) trails as a function of image-stack depth. Appendices B and B describe the application of CR-removal and charge transfer inefficiency trail removal over *wider* apertures in the `calwf3` pipeline, which is applied to SKYSURF’s drizzling process.

To drizzle the SKYSURF database, we generated instrument +filter-specific on-sky footprints for all for 220,657 images with $t_{\text{exp}} \geq 200 \text{ s}$ (out of a total of 249,861 SKYSURF images), starting with their APT files. This allowed us to organize the SKYSURF database in preparation for the drizzling process, and to assess its total area (Section 3.2), which we need for accurate galaxy counts averaged over as many independent HST fields as possible (Section 2.5.2).

In total, there are 11,965 APT footprints to be drizzled in SKYSURF, using a linking distance of $\lesssim 6'$. Each group

contains all images in all available filters, whose centers are within $6'$ of their nearest neighbor. The most frequently observed group has 10,761 exposure files (i.e., the HUDF), while the least-frequently observed groups have only one exposure in one filter and are mostly SNAPshots. The images in each group in the same filter *and* instrument are then drizzled into separate mosaics. With an average of ~ 4 – 5 exposures per HST orbit (Figure 5 and Table 4), the SKYSURF database amounts to $\sim 55,000$ HST orbits, or the equivalent of $\gtrsim 15$ yr of HST observing time assuming an average of ~ 3600 science orbits per year. We use all 11,965 APT footprints together with SKYSURF’s initial SB-measurements to assess which images are useful for the final set of reliable sky-SB measurements, and for the final object `SourceExtractor` and `ProFound` catalogs and all-sky object counts (Appendix C). Using the same matching algorithm, the 11,965 APT footprints contain the 4858 independent fields of Section 3.2 that are more than 1° away from the nearest APT footprint.

4.6. Drizzling All SKYSURF Images in AWS with Lowest Estimated Sky-SB Preserved per Image Family

The last unconventional step critical for SKYSURF is that, when drizzling the images, we preserve the sky level into all images that AstroDrizzle normally removes. This sky level, as defined in Section 4.2, is carefully monitored by SKYSURF as a function of orbital phase for all multiple exposures in a given filter visit per target (Section 4.3).

In a first drizzle run, the `ProFound` sky-surface maps of Section 4.2 are subtracted from each image and its LES level is added back in. In the second drizzle run, all images in a given filter from the first run have their own LES value subtracted, followed by adding to each image the lowest LES value from that visit that went into the mosaic. Hence, each mosaic is drizzled while reinstating the lowest sky-SB value from that visit (Sections 4.2–4.3). In the case of WFC3/IR—where we have more detector reads per exposure in a given visit—the average over the lowest three sky-SB values from that exposure gets reinstated to represent its sky-SB. The justification for this procedure is given in Figures 6 and 9, and Section 4.3. In all cases, the subtracted `ProFound` sky surface maps and the reinstated constant sky-SB levels are preserved as FITS files or in the FITS header, respectively, so future users can apply them differently for other purposes. Mosaic weight maps are also created in this process, to preserve the information on the signal-to-noise ratio in each mosaic pixel that follows from the sky-SB levels in the original images that were drizzled.

We use Amazon Web Services²⁹ for mass cloud computations without transferring all data files whenever possible, since the entire HST Archival database resides in AWS and is being kept up-to-date there by STScI. We use AWS to run our modified ACS and WFC3 pipelines on the HST Archival data until the end product is as reliable as it can be. Most of the code is Python, which works well in AWS. AWS can run code or pipelines in Python, R, or C⁺⁺. A few SKYSURF tasks originally developed under a FORTRAN or IRAF environment do not run on AWS, and are instead run on the SKYSURF servers at our home institutions.

On AWS, we can reprocess the HST ACS/WFC and WFC3/UVIS and IR Archive within a few months at modest costs for each iteration. We do this for the entire SKYSURF

²⁸ <https://hst-docs.stsci.edu/drizzpac/chapter-5-drizzlepac-software-package/5-2-astrodrizzle-the-new-drizzle-workhorse>

²⁹ <https://aws.amazon.com/>

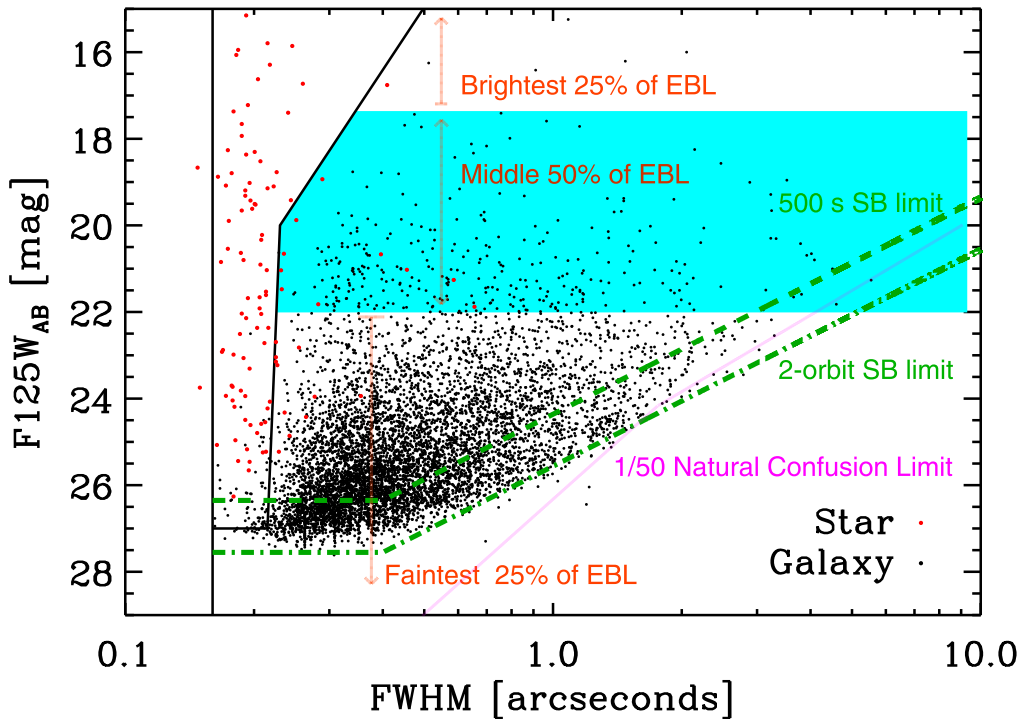


Figure 10. The star–galaxy separation procedure shown here for WFC3 F125W images (adapted from Windhorst et al. 2011; “W11”). Plotted are total AB-magnitude vs. SourceExtractor image diameter FWHM. Objects with image diameters less than the PSF-FWHM ($\approx 0''.14$; W11) are image defects and are discarded. Stars (thin vertical filament of red dots) and galaxies (black dots) are separated using cuts in FWHM and magnitude, similar to the black slanted line above from W11. This is effective at separating stars and galaxies in WFC3/IR data, which were separated using FWHM cuts in various filters. At $AB \approx 18$ mag, the star counts and galaxy counts reach similar surface densities at intermediate to high Galactic latitudes (Figure 11), and star–galaxy separation at these fluxes is straightforward at HST resolution. The star–galaxy separation becomes less reliable for fluxes fainter than $AB \approx 26$ mag. The red arrows indicate the F125W flux ranges where the brightest 25%, the middle 50%, and the faintest 25% of the discrete EBL level, respectively, are produced (Figure 2(d)). Green dashed lines indicate the SB-limits for an average single SKYSURF F125W exposure of $t_{\text{exp}} = 500$ s (Figure 5) and for the two-orbit F125W images of W11, whose data are plotted here. The pink line indicates the natural confusion limit derived from the integrated J -band counts in Figure 2(c) (represented here as a broken power law), as discussed in Section 4.7. Both of these limits are relevant for estimating whether a significant fraction of low-SB galaxies may have been missed at faint fluxes, to explain any significant diffuse EBL SKYSURF-2.

data set. Running ProFound on all images in the entire SKYSURF database takes one full month on AWS. Central storage space of 40 TB houses the different levels of data sets for processing and distribution at ASU, plus another 40 TB to store SKYSURF’s expanded data products. In total, 80 TB of disk space at ASU and ICRAR hosts the final SKYSURF database and products. These will be made available via MAST. Details on SKYSURF’s drizzle products as they become available, along with their applications, will be given by Carter et al. (2022).

4.7. Star–Galaxy Separation, Catalog Reliability, and Completeness

Our second main SKYSURF goal is to have highly reliable panchromatic HST object catalogs across the sky (Figures 3–4). SKYSURF therefore needs to define accurate, conservative completeness limits for each object catalog. We need to determine at what magnitude bin the counts in each filter and field start to turn over from the expected power-law slope (see Windhorst et al. 2011; Driver et al. 2016a; Figures 2 and 10–11 here). As a preliminary test, here we consider images taken as part of the WFC3/IR ERS program (W11). Because of SKYSURF’s large dynamic range in flux, we can afford to cut off each individual filter catalog in each HST field at rather high significance levels. From the deeper fields, we can then determine at which flux levels each shallower catalog becomes incomplete when we do the star and galaxy counts in

each field, typically at the $\gtrsim 5\text{--}6\sigma$ level for point sources. When all catalogs are combined, SKYSURF can provide accurate object counts for $16 \lesssim AB \lesssim 28$ mag. Details are given in Tompkins et al. (2022), Carleton et al. (2022b), and Goisman et al. (2022), including simulations to quantify incompleteness as a function of total flux, size, and SB.

Star–Galaxy Separation Method: The black slanted line in Figure 10 illustrates SKYSURF’s star–galaxy separation method of W11, where objects were classified as stars in at least three available filters from the 10-band filter set. The average SKYSURF field will have on average only \sim two filters available for star–galaxy separation (Table 4). Hence, SKYSURF’s star–galaxy separation process will be modified to work on fewer filters as the image drizzling, catalog production and object counting proceeds over all SKYSURF fields. The blue wedge in Figure 10 indicates the flux range $17.4 \lesssim AB \lesssim 22$ mag in F125W where galaxies contribute the central 50% of the EBL integral. The red arrows indicate the F125W flux ranges where the brightest 25%, the middle 50%, and the faintest 25% of the discrete EBL are produced, as determined from Figure 2(d) (Section 2.3).

Catalog Reliability: For $17.4 \lesssim AB \lesssim 22$ mag, a total of 37 objects were classified as stars (red dots) to the left of the black slanted–vertical line in Figure 10. To the right of the black slanted line, there are 328 objects (black dots) classified as galaxies for $17.4 \lesssim AB \lesssim 22$ mag, and 10 objects that were classified as stars in other filters but are misclassified in the

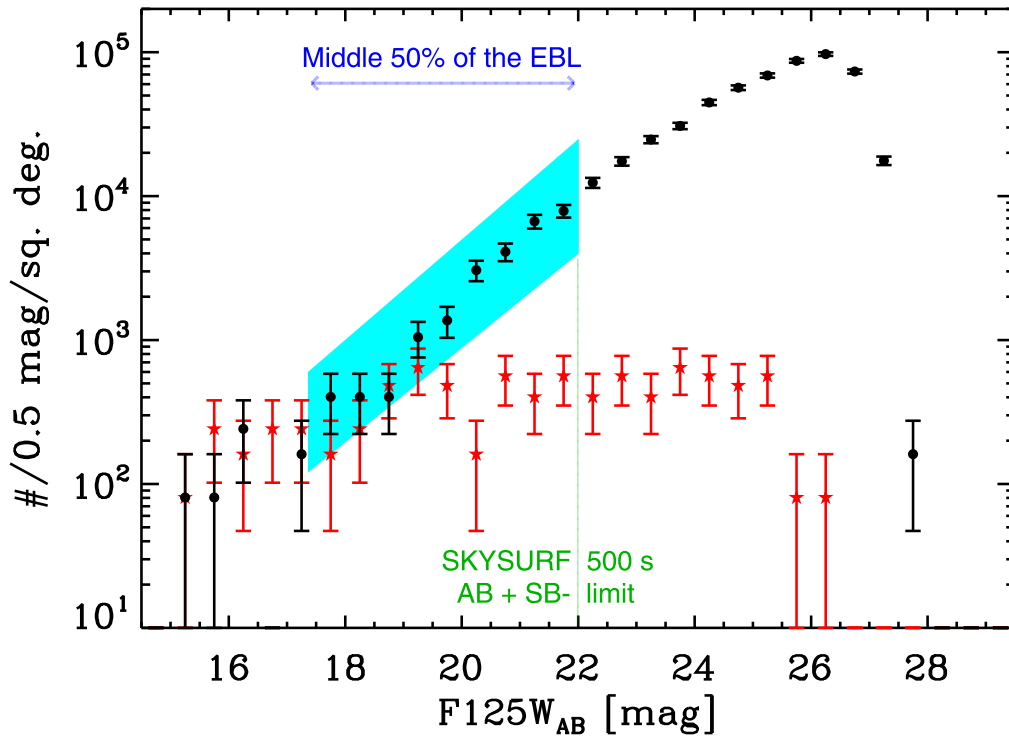


Figure 11. Differential star counts (red asterisks) and galaxy counts (black-filled circles) from the WFC3 ERS F125W images adapted from Windhorst et al. (2011), with the star–galaxy separation optimized from Figure 10. At $AB \simeq 18$ mag, the star counts and galaxy counts reach similar surface densities at intermediate to high Galactic latitudes, but star–galaxy separation at these fluxes is straightforward at HST resolution (Figure 10). The blue box indicates the $17.4 \lesssim J_{AB} \lesssim 22$ mag range where the *middle 50%* of the discrete EBL is produced in the J -band (Figure 2(d)). The vertical green line indicates the total flux level of $AB \simeq 22$ mag. Brighter than this limit, even shallow SKYSURF images with typical exposures times $t_{\text{exp}} \sim 500$ s are substantially complete for all galaxies with FWHM sizes $\lesssim 3''$ (Figure 10).

galaxy region in the F125W filter, although some of these could still be stars. Using such a star–galaxy separation method over this relatively bright magnitude range at HST resolution thus yields a fraction of objects misclassified as galaxies of $\sim 10/328 \simeq 3.0\%$. The ratio of classified stars-to-galaxies in this magnitude range is about $\sim 37/328 \simeq 11\%$. Because the star-to-galaxy ratio remains small at most Galactic latitudes with $|b_{\text{II}}| \gtrsim 30^\circ$, SKYSURF’s *galaxy* samples will thus in general be more reliable ($R \simeq 1 - (10/328) \simeq 97\%$) than its *stellar* samples (reliability $R \simeq 1 - (37/47) \simeq 78\%$).

Catalog Completeness: The two green dashed lines in Figure 10 show the SB limits for a typical single SKYSURF exposure of $t_{\text{exp}} = 500$ s and for a two-orbit exposure stack, which are ~ 25.6 and ~ 26.8 mag arcsec $^{-2}$, respectively. We use the distribution of points in Figure 10 to estimate the catalog completeness. In the average SKYSURF exposure time of ~ 2 orbits per filter, we expect the SKYSURF completeness limit for compact objects to be $AB \lesssim 26$ – 27 mag, depending on the filter used, and $\lesssim 28$ mag for the deeper HST fields. For many of the shallowest SKYSURF exposures, the completeness limit is $AB \lesssim 25.5$ – 26 mag (Tables 1–3 and Figure 11).

The pink line in Figure 10 indicates the “natural confusion” limit derived from the *integrated J*-band counts in Figure 2(c) (represented here as a broken power law). For galaxy FWHM sizes larger than the natural confusion limit at any given total flux, there is a $\gtrsim 2\%$ probability of objects overlapping *due to their own finite object sizes*, rather than due to the much smaller instrument PSF FWHM. Object-finding algorithms may start to have issues deblending a noticeable fraction of (lower-SB) objects at sizes larger than this limit, if such objects exist (Windhorst et al. 2008, 2021). Indeed, very few objects are

detected to the right of *either* the SB limit or the natural confusion limit in Figure 10. The most conservative of the two limits thus seems to be bounding the detected galaxy samples at any r_c value. (For deeper HST images, the natural confusion limit remains fixed, but the SB limit improves with image depth, so the natural confusion limit thus becomes as important as the SB limit). Together, these two limits are relevant for estimating whether a significant fraction of low-SB galaxies may have been missed at faint fluxes, to explain a significant excess of diffuse EBL (Figure 1 and SKYSURF–2). Further discussion is given by Windhorst et al. (2021) and Kramer et al. (2022).

We use the two-orbit F125W data in Figure 10 (lower green dashed lines) to estimate the incompleteness due to SB-selection in an average 500 s SKYSURF exposure (top green dashed lines) and natural confusion (pink line). This allows us to estimate the amount of discrete, integrated, and extrapolated EBL not yet subtracted from SKYSURF’s sky-SB measurements in SKYSURF–2. For this calculation, we assume that the fraction of faint low-SB objects missing in typical 500 s F125W exposures due to SB-selection is *mostly detected* in the deeper two-orbit data of W11 shown in Figure 10. This estimate thus does not yet include any population of faint, very low-SB objects that might be missing from the deepest HST images altogether to the right of these lines in Figure 10, which we address in SKYSURF–2. To assess the amount of possibly missing discrete, integrated, and extrapolated EBL in panels (b) and (d) of Figure 2, due to SB selection, we estimate the 500 s catalog incompleteness in each AB-magnitude slice from the fraction of objects *known* to exist in deeper HST images between the two green SB boundaries in Figure 10. This

incompleteness amounts to $\sim 1\%$ at $AB \simeq 22.0$ mag and increases to $\sim 26\%$ at $AB \simeq 26.0$ mag. For the eight 0.5 mag slices between $22 \lesssim J_{AB} \lesssim 26$ mag, the incompleteness correction due to SB selection is represented by:

$$\text{Incompleteness Correction} = 1.0 + [1.00 + 6.184 (J_{AB} - 22.0 \text{ mag})]/100\%, \quad (3)$$

where the quantity between square brackets is the best fit to the estimated percentage of *known* missing objects as a function of total AB-mag. For $AB \gtrsim 26.5$ mag, sample incompleteness is not considered here, because the average 500 s SKYSURF exposure does not reach fainter than this limit. We note that Equation (3) would imply an SB incompleteness of $\sim 45\%$ at $AB \lesssim 29$ mag. The SB incompleteness at $AB \lesssim 29$ mag could possibly be that large, given the much deeper HUDF data and SB limits plotted in Figure 2 of Windhorst et al. (2008) and Windhorst et al. (2021). Much deeper JWST images will be needed to address the SB incompleteness for objects with $AB \gtrsim 26\text{--}30$ mag. Further considerations of SB selection against ultra-diffuse low-SB galaxies in deep surveys are discussed in, e.g., the SMUDGES survey of Zaritsky et al. (2019), the Subaru Hyper Suprime-Cam survey of Greco et al. (2018), and future SKYSURF studies. For our average shallow SKYSURF exposures and catalogs, we adopt Equation (3) as the *minimum* SB-incompleteness correction that needs to be applied for $22.0 \lesssim J_{AB} \lesssim 26.5$ mag to the discrete integrated EBL for objects that are known to exist in deeper HST images, but that are missing in the average 500 s SKYSURF exposures. This correction is applied in SKYSURF-2, to fully estimate our iEBL+eEBL values.

4.8. Proof of Concept: HST–Kelsall 1.25 μm Sky-SB Difference versus Net Object SB in Each Image

It is possible that stray light from discrete objects may contaminate our sky-SB measurements even with the best algorithms of Section 4.2. This could be due to residual instrumental effects not recognized in Section 4.1, or due to stray light from or the extended light profiles of bright objects. While the HST cameras are in general well-baffled against stray light, there are known locations just inside or outside the detector FOV where light within the telescope can scatter back onto or within the detector, thus raising the measured sky-SB levels between the discrete objects (Section 4.1.3).

To provide a proof of concept for our methods in this paper, we therefore investigated whether the (sky-subtracted) total object brightness is correlated with levels of diffuse light that may be present or left in each image. We consider the total flux coming from objects in each image to be the mean pixel value of the *_flt* image minus the LES sky-SB level as measured in Section 4.2. For this test, we exclude images that may be contaminated by earthshine or sunlight scattered off the Earth by only considering Sun altitudes $\alpha_{\odot} \lesssim 0^{\circ}$ (Section 4.3). We also exclude images that are significantly saturated with objects, where more than 30% of the subregions are masked out in Figure 7.

We perform this test on the WFC3/IR F125W images for two reasons: (1) we use WFC3/IR’s ability to flag and remove most cosmic rays during each on-the-ramp exposure, so that each image mean-pixel value is not skewed by bright CRs, but instead traces the sky-SB plus the total object flux in the image;

(2) we can directly compare the LES sky-SB in each WFC3/IR F125W image to the Kelsall et al. (1998) COBE/DIRBE *J*-band zodiacal model prediction made in the *same direction and time of the year* (i.e., at the same R.A., decl., t). We assume here that the HST–Kelsall sky-SB differences are a measure of diffuse light that may be present in the F125W images. Details of the applied Kelsall et al. (1998) model and the analysis of the HST–Kelsall sky-SB differences are given in SKYSURF-2.

In essence, we are testing here if the darkest WFC3/IR F125W images—where we can measure LES values close to the zodiacal sky-SB—are largely free of residual object flux that affects the sky-SB. The results are shown in Figure 12, where the F125W HST–Kelsall sky-SB differences are nearly constant at ~ 0.0071 MJy sr^{-1} or ~ 17 nW $\text{m}^{-2} \text{sr}^{-1}$ over a factor of 100 in total object flux along the horizontal axis. Hence, Figure 12 shows no significant trend between the HST–Kelsall sky-SB difference in each image and its total sky-subtracted object brightness. This confirms the validity of our LES method to estimate sky-SB values that are largely free of residual object flux. We will return to this residual HST–Kelsall sky-SB difference in all three WFC3/IR filters in SKYSURF-2.

In summary, it is unlikely that a residual diffuse light level is affected significantly by instrumental effects where light from discrete objects scatters back into image pixels that are part of the foreground sky-SB. This suggests that discrete objects (i.e., extended stellar or galaxy light profiles) can be ruled out as a major source of diffuse light.

5. Discussion

In this section, we briefly summarize how SKYSURF’s methods and the error budget of Section 4 propagate into the constraints on diffuse light that HST may see in excess of zodiacal models. We confine ourselves to the WFC3/IR F125W filter used as an example throughout this paper. We refer to Carleton et al. (2022a; or “SKYSURF-2”) for a detailed discussion of any diffuse light signal HST may see—or limits thereto—at 1.25–1.6 μm in excess of the Kelsall et al. (1998) and Wright (1998) zodiacal models.

The F125W filter has 6810 full on-the-ramp exposures (Table 3), of which 2337 survive the subselection in Section 4.8. Figure 12 suggests an average HST–Kelsall sky-SB difference of $+0.0071 \pm 0.0138$ (rms) MJy sr^{-1} , or $\sim 17 \pm 33$ (rms) nW $\text{m}^{-2} \text{sr}^{-1}$. These are the values *before* subtraction of the WFC3/IR thermal dark signal and the DGL for each exposure. SKYSURF-2 discusses in detail the corrections that need to be made to the total HST WFC3/IR diffuse sky signal, which include subtracting the best-fit TD signal from a variety of HST component temperatures, and the DGL level as estimated for each image location in the sky.

The discussion of the HST calibration, zero-point, sky-SB measurements, and TD signal errors in Sections 4.1–4.2 and Table 5 suggest a $\sim 2.7\%$ total error in our ability to estimate the F125W sky-SB. Subtraction of the DGL has its own errors, as does the comparison to any of the zodiacal light models. For instance, the error in the Kelsall et al. (1998) ZL model prediction is 15 nW $\text{m}^{-2} \text{sr}^{-1}$ at 1.25 μm and 6 nW $\text{m}^{-2} \text{sr}^{-1}$ at 2.2 μm . This amounts to $\sim 3\%$ of their average *predicted* zodiacal sky-SB. In SKYSURF-2, we thus need to add these ZL model errors in quadrature to the total sky-SB estimation error of Table 5—appropriately interpolated for the F140W and F160W filters—before constraints can be placed on diffuse

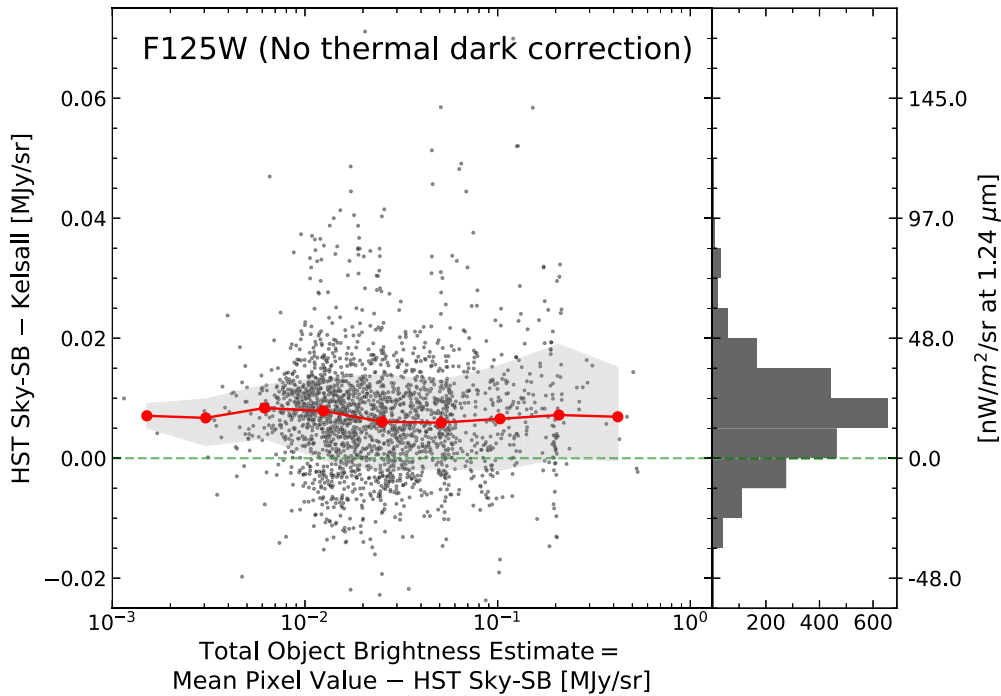


Figure 12. Difference in observed HST WFC3/IR F125W sky-SB and the Kelsall et al. (1998) model prediction vs. total *residual object brightness* after subtracting from each image the best sky-SB estimate of Section 4.2. We only include images taken with a Sun altitude less than 0° and where no more than 30% of the subregions are masked in Figure 7. To estimate the total *residual object brightness*, we calculate the mean pixel value of every image and then subtract the measured LES sky-SB level of that image. The average $1.25 \mu\text{m}$ HST–Kelsall sky-SB difference amounts to $\sim 0.0071 \text{ MJy sr}^{-1}$ or $\sim 17 \text{ nW m}^{-2} \text{ sr}^{-1}$. We find no significant trend between the HST–Kelsall sky-SB in each image and its total sky-subtracted object brightness. This confirms the validity of our LES method to measure sky-SB values that are largely free of residual object flux.

light that HST may see in excess of the zodiacal light models. We now have all the tools in place to do so.

Last, we return to the most recent diffuse light limits that have been placed on the visual–near-IR wavelength range, as summarized in Section 2 and Figure 1. The CIBER spectra of Matsuura et al. (2017) suggest a diffuse light component in excess of the *discrete* EBL of $25.6 \pm 12.9 \text{ nW m}^{-2} \text{ sr}^{-1}$ at $1.1 \mu\text{m}$ and $29.7_{-9.9}^{+15.9} \text{ nW m}^{-2} \text{ sr}^{-1}$ at $1.6 \mu\text{m}$ compared to the Kelsall et al. (1998) model prediction as seen from 1 au. Sano et al. (2020) reanalyze the weekly COBE/DIRBE data and suggest the existence of a total (isotropic) diffuse light component of $\sim 45 \pm 10 \text{ nW m}^{-2} \text{ sr}^{-1}$ in excess of the Kelsall et al. (1998) model at $1.25 \mu\text{m}$, which amounts to $\sim 34 \pm 10 \text{ nW m}^{-2} \text{ sr}^{-1}$ after subtracting the iEBL+eEBL component of $11.2 \pm 0.9 \text{ nW m}^{-2} \text{ sr}^{-1}$ (Koushan et al. 2021; Carleton et al. 2022a). We plot these constraints as the purple symbols in Figure 1. Korngut et al. (2022) use spectra from three recent CIBER rocket flights to estimate the Equivalent Width (EW) of the Ca triplet around 8542 \AA , extrapolate their result to the Kelsall et al. (1998) model prediction at $1.25 \mu\text{m}$, and find a diffuse light component of $46 \pm 19 \text{ nW m}^{-2} \text{ sr}^{-1}$ at $1.25 \mu\text{m}$. This estimate has a larger error, but because it is based on the Ca triplet, they suggest a residual (spheroidal) zodiacal component that is not present in the Kelsall et al. (1998) model. Lauer et al. (2021, 2022) present $0.608 \mu\text{m}$ object counts and sky-SB measurements from New Horizons images taken at 43–51 au (blue points with error bars in Figure 1), where their single image obtained at 51 au from the Sun suggests a much dimmer diffuse light signal of $\sim 8.1 \pm 1.9 \text{ nW m}^{-2} \text{ sr}^{-1}$ at $0.608 \mu\text{m}$. They discuss a number of explanations for such a signal.

SKYSURF-2 will discuss the HST diffuse light constraints at $1.25\text{--}1.6 \mu\text{m}$ from SKYSURF in the context of this recent work. In O’Brien et al. (2022), we will present the sky-SB in the broadband ACS/WFC, WFC3/UVIS, and WFC3/IR filters of Tables 1–3, and compare these results to various zodiacal light models at $0.2\text{--}1.7 \mu\text{m}$. Tables 1 and 2 show that the full SKYSURF data set will have $\sim 49,000$ images in the F606W filter alone that use all three HST cameras, ACS/WFC, WFPC2, and WFC3/UVIS, allowing us to check for camera-dependent systematics. SKYSURF’s goal is then to use all these results to better constrain the zodiacal light models and how much diffuse light may exist at $0.2\text{--}1.7 \mu\text{m}$ as seen from low Earth orbit.

6. Summary and Conclusions

In this paper, we present an overview and describe the rationale, methods, and first results from the Hubble Space Telescope Archival project “SKYSURF.” The following are our main highlights and results:

1. SKYSURF uses HST’s unique capability as an *absolute photometer* on timescales of decades to measure the $0.2\text{--}1.7 \mu\text{m}$ all-sky surface brightness from 249,861 WFPC2, ACS, and WFC3 exposures. Of these, 220,657 exposures have $t_{\text{exp}} \geq 200 \text{ s}$ and cover 16,822 HST FOVs that are being drizzled in, on average, ~ 8 exposures per filter and ~ 1.8 filters per target.
2. Among these, ~ 1400 constitute independent HST fields spread across the sky that are suitable for galaxy counts that average over cosmic variance, and cover an area of $\lesssim 10 \text{ deg}^2$. For object detection and catalogs, our zero-

point errors are $\lesssim 1.5\%$, while for sky-SB estimates, our total errors are $\lesssim 3\%$ – 4% of the zodiacal sky-SB.

3. SKYSURF’s panchromatic Legacy data set is designed to constrain the diffuse UV-near-IR sky-SB components: zodiacal light (inner solar system), Kuiper Belt Objects (outer solar system), Diffuse Galactic Light, integrated and extrapolated discrete Extragalactic Background Light (iEBL/eEBL), and the diffuse Extragalactic Background Light (dEBL).
4. Many of SKYSURF’s goals require a nonstandard reprocessing of these HST images that we summarize, which includes, e.g., monitoring the instrument zero points over 11–18 yr, identifying and removing image gradients where needed, using wider object apertures to remove the outskirts of stars and galaxy images as well as trails from CRs and charge transfer inefficiency effects, and restoring into each drizzled image footprint the lowest estimated sky level from each visit in a given image/filter combination.
5. We present simulations of HST WFC3/IR images with known sky values and sky gradients, as well as realistic CR distributions and star plus galaxy counts. We test nine different algorithms that measure the LES in each image away from the discrete objects and identify the best algorithm that recovers the inserted LES values to within 0.2% when there are no image gradients, and within 0.2%–0.4% in the presence of 5%–10% image gradients. Images with larger gradients are flagged for SKYSURF sky-SB analysis. Sky-SB values and image gradients are checked against the Earth limb angle, Sun altitude, Sun angle, and Moon angle, to help identify the cleanest and darkest subset of the SKYSURF images.
6. Our WFC32/IR sky-SB estimates in the F125W, F140W, and F160W filters have errors of $\sim 2.7\%$ – 3.8% of the average sky-SB, respectively. We compare our WFC3/IR F125W sky-SB estimates to the Kelsall et al. (1998) *J*-band zodiacal model prediction for the same direction and time of the year. We find no significant trend between the $1.25\ \mu\text{m}$ HST–Kelsall sky-SB difference for each image and its total sky-subtracted object brightness. This confirms the validity of our LES method to estimate sky-SB values that are largely free of residual object flux.
7. Last, we will release to MAST our SKYSURF’s panchromatic legacy products with the publication of the respective sequel papers: optimized object catalogs, absolute calibrated panchromatic sky-SB data, and models of the ZL, DGL, and EBL, with pointers and documentation at the SKYSURF website at ASU (<http://skysurf.asu.edu>). Through this first SKYSURF paper, we invite community feedback, so we may further improve our methods as the entire SKYSURF database gets reprocessed.

We dedicate this paper to Dr. Jan Hendrik Oort, who during his long and very productive life predicted the existence of the Oort Cloud, which he sometimes doubted could be observed (Dr. M. J. A. Oort, private communication).

We thank the referee for thoughtful suggestions that helped improve the presentations of this paper. We thank Annalisa Calamida, Susana Deustua, Sylvia Baggett, Jay Gallagher, Phil Korngut, Tod Lauer, John Mather, Peter McCullough, Marc Oort, Marc Postman, Michael Tompkins, and Meenakshi Wadhwa for helpful suggestions. We thank Dr. Larry Petro

for help in the early stages of this project. We thank Javier Calunga for help in setting up our SKYSURF servers, and Mark Stevens for continuous help in maintaining the SKYSURF server website. We thank HST Archive staff at STScI for getting a very large amount of HST Archival data to us without any major hiccups, and for their expert advice on HST component temperatures. All of the data presented in this paper were obtained from the Mikulski Archive for Space Telescopes (MAST). This project is based on observations made with the NASA/ESA Hubble Space Telescope and obtained from the Hubble Legacy Archive, which is a collaboration between the Space Telescope Science Institute (STScI/NASA), the Space Telescope European Coordinating Facility (ST-ECF/ESA), and the Canadian Astronomy Data Centre (CADM/NRC/CSA). Some image simulations were based on observations taken by the 3D-HST Treasury Program (GO 12177 and 12328) with the NASA/ESA HST, which is operated by the Association of Universities for Research in Astronomy, Inc., under NASA contract NAS5-26555. Work by R.G.A. was supported by NASA under award number 80GSFC21M0002.

We thank Ms. Desiree Crawl, Prof. Thomas Sharp, and the NASA Space Grant Consortium in Arizona for consistent support of our many undergraduate SKYSURF researchers at ASU during the pandemic. We acknowledge support for HST programs AR-09955 and AR-15810 provided by NASA through grants from the Space Telescope Science Institute, which is operated by the Association of Universities for Research in Astronomy, Incorporated, under NASA contract NAS5-26555.

We also acknowledge the indigenous peoples of Arizona, including the Akimel O’odham (Pima) and Pee Posh (Maricopa) Indian Communities, whose care and keeping of the land has enabled us to be at ASU’s Tempe campus in the Salt River Valley, where this work was conducted.

Facility: Hubble Space Telescope Mikulski Archive <https://archive.stsci.edu>; Hubble Legacy Archive (HLA) <https://hla.stsci.edu>; Hubble Legacy Catalog (HLC) <https://archive.stsci.edu/hst/hsc/>

Software: Astropy: <http://www.astropy.org> (Astropy Collaboration et al. 2013, 2018); IDL Astronomy Library: <https://idlastro.gsfc.nasa.gov> (Landsman 1993); Photutils: <https://photutils.readthedocs.io/en/stable/> (Bradley et al. 2020); ProFound: <https://github.com/asgr/ProFound> (Robotham et al. 2017); ProFit: <https://github.com/ICRAR/ProFit> (Robotham et al. 2018); SourceExtractor: <https://www.astromatic.net/software/sextractor/> or <https://sextractor.readthedocs.io/en/latest/> (Bertin & Arnouts 1996).

Appendix A

HST Orbital Parameters and Orbital Stray light

In Appendices A.1–A.2, we give a summary of the calculation of HST’s orbital parameters, as well as of stray light from the Earth, Sun, and Moon across HST’s orbital phases. In Appendix A of SKYSURF–2, we also give summary of HST’s known thermal behavior as documented in its telemetry data.

A.1. Calculation of HST Orbital Parameters

The Earth’s Limb Angle (LA) is recorded in the *jit*-files every few seconds during an exposure. SKYSURF retrieves this information for all ACS/WFC3, WFPC2, and WFC3/UVIS

and IR images. The run of LA's across a WFC3/IR exposure has to be recomputed using the post-observing ephemerides of HST. We developed code to generalize this, and obtain a good match to these *jit*-values compared to ephemerides. The LA-predicting software³⁰ calculates the exact *past* HST orbital parameters (in six-dimensional space \vec{s} + velocity \vec{v} coordinates: $(x, y, z; v_x, v_y, v_z)$) in the geocentric system for any time in the past, which can be retrieved from the NORAD database,³¹ where HST is satellite number 20580. The NORAD satellite archive returns a file that needs to be split into individual HST orbital files, which is done with IDL routine `split_hstorbits.pro`. The results are saved in a `.predict` folder, and the LA is calculated with `limbangle.pro`, which updates the `predict` files for each orbit. Together with the past HST ephemerides, these calculations also include the Illuminated Earth Fraction (IEF) as a parameter that can affect the amount of stray light in the individual SKYSURF images (Section 4.3). Because of Earth-limb stray light possibly reflecting differently off the HST OTA cover at different off-nominal roll angles (RAs), this code can also help trace the sky-SB as a function of off-nominal RA and IEF as needed (Caddy & Spitler 2021).

It should be noted that COBE's orbit is at an average Low Earth Orbit (LEO) altitude of 885 km, while HST is at an average orbital altitude of ~ 539 km. The HST orbital altitude was somewhat higher early in the mission, and it has slightly decayed during the 1991, 2002, and 2013 solar maxima, but some altitude was recovered due to reboosts from several of its five Shuttle Servicing Missions. Given the very low atmospheric emission at 539–885 km altitude in directions well away from the Earth (other than geocoronal lines such as Ly α at 1216 Å and He II at 1.083 μm), we will assume that the *orbital altitude difference* between the HST and COBE is *not* the main source of any differences in 1.25–1.6 μm sky-SB measurements between the two missions discussed in SKYSURF-2. This is supported by MSISE-90 Upper Atmospheric models of the Earth,³² which list the mean atmospheric pressure as being 2.27×10^{-7} Pa at 540 km, while it is 1.04×10^{-8} Pa at 885 km.

A.2. HST Orbital Stray light

This section gives further details on stray light due to proximity to the Earth's limb, the Sun altitude above the bright Earth and the Sun angle with respect to HST's pointing direction, as well as due to the Moon angle.

A.2.1. Earth's Limb Angle

Eliminating levels of scattered earthshine contamination in exposures used in deriving sky-SB levels is paramount to the core science goals of SKYSURF. All orbital parameters that may impact the earthshine intensity in exposures must be considered. SKYSURF thus needs to identify and flag all exposures impacted by earthshine or scattered light. To ensure that earthshine is limited to a minimum, one would need to select only those fields that were taken in orbital dark time, which meet the SHADOW or LOW-SKY Special Requirements. STScI developed these options for this purpose early in the HST mission, as can be seen in the

³⁰ <https://www.qsl.net/kd2bd/predict.html> (IDL) and <https://github.com/npirzkal/EarthPlot> (Python).

³¹ <http://www.celestrak.com/NORAD/archives/request.php>

³² <http://www.braeunig.us/space/atmos.htm>

current version of APT. However, not every HST observer who asked for orbital SHADOW or LOW-SKY time in their APT file did, in fact, receive it, nor did every observer who received orbital SHADOW or LOW-SKY time ask for it.

We flag all individual images that came too close to the Earth's limb ($\text{LA} \lesssim 40^\circ\text{--}60^\circ$), irrespective of whether the observer asked for orbital dark time or not. For WFC3/IR, we do this also using individual time samples *within* an exposure, as in Figures 9(a)–(b). Since the orbital dark time does not generally exceed ~ 1800 s per HST orbit, the simplest approach is to subselect only those exposures in the range 200–1800 s. Exposures longer than 2100 s often run into elevated sky, due to proximity to the Earth's limb. An example is given by the green 0.23 and 1.6 μm points in Figure 1, which are for these reasons higher than the expected zodiacal SB values that are normalized to the solar spectrum, as discussed in Windhorst et al. (2018).

Figure 9(a) shows the sky-SB as a function of Earth's limb angle. The orange line and model uncertainty wedge of Caddy & Spitler (2021) show the elevated sky-SB due to earthshine for Sun altitude $\alpha_\odot \simeq 90^\circ$ on the orbital day side with the SA fixed at $\sim 90^\circ$. The model cuts off at $\text{LA} \sim 20^\circ$ due to HST scheduling constraints. A strong exponential increase is seen for fields taken on the day side of the orbit with $\text{LA} \lesssim 40^\circ\text{--}45^\circ$, but even fields with $\text{LA} \lesssim 70^\circ\text{--}80^\circ$ on the day side have an elevated sky-SB. The blue line plus uncertainty error wedge indicates the Caddy & Spitler (2021) model on the night side for $\alpha_\odot \simeq -10^\circ$, and shows a marked decrease in sky-SB. The model extends to $\text{LA} \simeq 10^\circ$, due to scheduling constraints on the night side. Deviation from an otherwise flat relation is seen for fields with $\text{LA} \lesssim 20^\circ$ on the night side. Exposures that have $10 \lesssim \text{LA} \lesssim 20^\circ$ and also $\alpha_\odot \lesssim 0^\circ$ have reduced sky-SB, but with somewhat increased scatter due to the shallow limb angle.

In summary, earthshine increases strongly as a function of limb angle. This is also visible in FIGS WFC3/IR grism data (e.g., Pirzkal 2014; Brammer et al. 2015; Brammer 2016). The 1.083 μm geocoronal He II line can be quite bright and contaminate WFC3 near-IR images in the F105W and F110W filters and the G102 grism (Brammer et al. 2014; Pirzkal & Ryan 2020), so F105W and F110W images with increased sky-SB levels are also flagged for this reason. SKYSURF-2 shows that the HST WFC3/IR F125W and COBE/DIRBE *J*-band filters exclude the 1.083 μm geocoronal He II line, if it is present at low limb angles. The WFC3/IR filters F125W, F140W, and F160W used for our first SKYSURF results in Carleton et al. (2022a) are thus free of the brightest known geocoronal emission lines.

A.2.2. Sun Altitude and Sun Angle

In addition to the Earth's limb angle, the Sun altitude above the Earth's limb, the Sun angle, and the Moon angle (both measured from HST's pointing direction) over the duration of an exposure must be identified and constrained to minimize sunlight scattered off the bright Earth, or off the IPD cloud at angles too close to the Sun. The results of this analysis are shown in Figures 9(b) and (d).

Sun Altitude (α_\odot): The Sun altitude limit is found to be the most influential parameter in reducing earthshine contamination, followed by the limb angle limit. For SKYSURF data, the Sun altitude limit is chosen to be all exposures with $\alpha_\odot \lesssim -10^\circ$. Earthshine directly below the location of HST can be assessed

independently from surface flux measurements at 0.3–5 μm wavelengths by the CERES (Clouds and the Earth’s Radiant Energy System) satellite over the duration of *the same* low-Earth orbit (Wielicki et al. 1996). This enables us to monitor earthshine levels *in real time* on the day side of an HST orbit underneath the telescope, where the intensity of earthshine cannot be accurately predicted, due to the complex nature of the weather systems below (Caddy & Spitler 2021). This work suggests that higher earthshine levels are found to potentially contaminate HST fields with Sun altitudes values $\alpha_{\odot} \gtrsim -10^{\circ}$ or more on the day side of an orbit. Figure 9(b) shows the sky-SB as a function of Sun altitude α_{\odot} . The orange and blue lines plus model uncertainty wedges of Caddy & Spitler (2021) show that lower LAs result in steeper relationships for Sun altitudes $\alpha_{\odot} \gtrsim 10^{\circ}$ – 20° , due to the increased sunlight scattered off the bright Earth. In this CVZ data set—and in many others—the Sun altitude can be $\gtrsim 90^{\circ}$, and in GOODS-N up to 110° (Figure 9(b)), or $\sim 20^{\circ}$ toward HST’s aperture as seen from HST’s “local zenith.” Such angles almost certainly increase Solar stray light off the bright Earth, depending on HST’s roll angle and how its aperture door faces the illuminated Earth. For $\alpha_{\odot} \lesssim -10^{\circ}$, the sky-SB is lowest and remains approximately constant. As a result, no day-side exposures are used in the final SKYSURF sky-SB analysis. This constraint considerably reduces the amount of usable data in the archive, but is necessary to prevent significant earthshine contamination.

Sun Angle: Figure 9(d) shows that the minimum HST sky-SB levels increase for Sun angles $\lesssim 80^{\circ}$, including on the night side of an orbit, in part due to an increase in ZL intensity closer to the Sun. Standard HST scheduling constraints of $\text{SA} \gtrsim 50^{\circ}$ are observed. HST observations are often scheduled at or near $\text{SA} \simeq 90^{\circ}$ or “nominal roll” angle, to ensure optimal illumination of the solar array. Sun angles are therefore clustered corresponding to the date of the exposures. The large scatter in the sky-SB levels around each Sun angle is primarily due to the variation in Sun altitude and limb angle for each exposure. Due to the degeneracy between elevated ZL and scattered sunlight inside the HST telescope tube, it is not possible to identify the dominant cause of elevated sky-SB for Sun angles $\text{SA} \lesssim 80^{\circ}$. As a result, we will avoid Sun angles $\text{SA} \lesssim 80^{\circ}$ for our final SKYSURF sample.

A.2.3. Moon Angle

Figure 9(c) shows the sky-SB as a function of Moon angle. For the Moon, the HST avoidance angle is typically $\text{MA} \gtrsim 50^{\circ}$. At $\text{MA} \gtrsim 50^{\circ}$, the Moon angle is not the major driver of increased sky-SB.

Appendix B Specific SKYSURF Requirements for Image Drizzling and Image Filtering

In this section, we discuss the application of wider apertures for the removal of trails from cosmic rays (CRs) and charge transfer inefficiency effects during drizzling. We also give details on SKYSURF’s methods to identify and remove HST images with large artifacts, and HST images with large targets that overfill the FOV. In all cases, fields that are discarded during the flagging process in Appendix B.3 must have a known reason for their omission, to avoid biasing the remaining sample with galaxy counts in Appendix C that are

too low or too high. Further details are given in Tompkins et al. (2022).

B.1. Application of Wider-aperture Cosmic-ray Removal during Drizzling

SKYSURF has several unique aspects that optimize its CR rejection procedures: (a) performing wider-aperture CR rejection to get accurate sky-SB measurements; (b) drizzling images that mostly overlap; and (c) properly drizzling all targets with one ACS, WFPC2, or WFC3 exposure per filter. These latter steps are needed to increase the statistics for SKYSURF sky-SB measurements. The HLA does not process all HST images, and it does not drizzle HST targets with one exposure per filter, nor does it drizzle targets with partly overlapping images. SKYSURF needs to carry out both steps to increase the statistics for SKYSURF sky-SB measurements and apply the GDC to each output image in order to enable us to do faint object photometry across each FOV.

Nonstandard CR rejection is required for SKYSURF. For reliable discrete object counts, we need to remove CRs reliably during drizzling. Miles et al. (2018) and Miles et al. (2020) recovered more than 1.4 billion CRs that have hit ACS, WFC3, or STIS images, which took a few days on AWS to process. The CR flux varies by 10%–20% across the solar cycle, in a way that is anticorrelated with the solar maximum activity (Miles et al. 2018). SKYSURF uses the fact that CRs are usually sharper than the FWHM of the image PSF to remove them from images with only 1–2 exposures (e.g., van Dokkum 2001). For most targets with $\gtrsim 3$ –4 exposures per filter per target (Table 4), the CR filtering will work more reliably by comparing the sky flux in each aligned pixel (e.g., Windhorst et al. 1994a).

The CR rejection is customized in this processing, in particular ensuring that faint regions around bright CRs are accurately rejected and accounted for, so as not to impact the final surface brightness measurements. To make sure this is done correctly, we run the pipeline on both the `_flt` and the CTE-corrected `_flt` files (`_flc`), with two different CR rejection masks. We then use the `_flt` images for the sky histogram, and `_flc` images to get the best possible total fluxes (Appendix B.2). This uses wider apertures to optimize the CR masking, and is part of our modified SKYSURF pipeline. AstroDrizzle performs this process as follows: (a) all images, starting with single exposures per filter, get drizzled on a grid with a common Gaia DR2–based (Gaia Collaboration et al. 2021) World Coordinate System (WCS); and (b) `SourceExtractor` and `ProFound` are run on all images, including the single exposures per target, where typically 5%–10% of the pixels are affected by CRs. Most algorithms in Section 4.2 can nonetheless measure their sky-SB accurately, and `ProFound` (Robotham et al. 2017) has been tested to verify it can do so also. All multiple orbital—or multi-orbit—exposures per filter on a given target are then drizzled into a final mosaic for each filter on that target (Sections 3.2 and 4.5). The lowest sky-SB measurement is preserved for each visit during this drizzling process (Section 4.6), with sky gradients mapped and removed (unless they are part of the astrophysical scene). Both the removed sky gradients and the restored sky levels are preserved as separate FITS files or in the FITS header, respectively, for later diagnostics or other uses.

SKYSURF is processing all HST images with exposure times $t_{\text{exp}} \geq 200$ s (220,657 WFPC2, ACS, and WFC3 exposures in

16,822 HST FOVs (Table 4) through these special-purpose, nonstandard DrizzlePac steps on AWS, including the use of custom-measured sky values, and preserving the full information about any variation in sky between different exposures.

B.2. Application of Wider-aperture Removal of Charge Transfer Inefficiency Trails

To get the most reliable sky-SB measurements, SKYSURF also makes corrections for Charge Transfer Efficiency (CTE) degradation. We assess and correct biases due to the increase of CTE effects over time, i.e., trails behind bright point sources, including CRs. CTE trails that bleed into the sky-SB foreground are not removed in standard processing. The standard pipeline therefore applies the CTE-correction code of Anderson & Bedin (2010) to all images before drizzling. If not corrected, CTE trails may affect the sky pixel histogram, and may also accentuate read-noise artifacts. During the 90–100 s ACS and WFC3 readout times, CRs are also accumulated during readout; these CRs are harder to deal with. We therefore use the non-CTE-corrected *_flt* files to remove those CRs. SKYSURF then grows the standard CR masks a little larger than normal, to remove faint CTE trails in the final drizzled images. For a subset of the data per detector, we test our SB-measurements *before and after* removal of CTE trails (Anderson & Bedin 2010) as a check. We find no significant difference in the sky-SB estimates.

We use the *_flc* images to get the sky histograms and the best possible total object fluxes. With `SourceExtractor` or `ProFound`, we then define all objects on the *_flc* images, and next grow the CR, CTE, and object masks on the *_flt* images, to ensure that all of the CTE-trailed CR flux and object flux is included in the CR-, CTE-, and object-rejection apertures. Since SKYSURF’s data set has a large dynamic range in flux, we can afford to do wider-aperture removal of CRs: false negatives are acceptable (e.g., some faint point-like objects mistakenly removed as CRs in some images), but false positives are not (e.g., faint CRs left in the images). The optimal parameter settings for blind global CR masking for SKYSURF thus need to be done over more conservative, wider apertures than are used for default CR removal.

The CTE-correction code of Anderson & Bedin (2010) has been improved over the years (e.g., Anderson et al. 2021), and is now available under `calwfc3` pipeline version 3.6.0 and higher. Our WFC3/UVIS images were retrieved in spring 2020 using the latest available `calwfc3` version 3.5.0 at that stage, which implemented the 2016 version of the CTE correction. The primary differences between the 2016 and 2021 CTE corrections are a somewhat noisier sky image and perhaps somewhat overcorrected faint object fluxes using the 2016 CTE correction, and a somewhat smoother sky with somewhat undercorrected faint object fluxes using the 2021 CTE correction.³³ To quantify this for SKYSURF, we ran all WFC3/UVIS F850LP images with both `calwfc3` pipelines (versions 3.5.0 and 3.6.2 in early 2022) on AWS. We found indeed that the rms sky noise in object-free areas was $\sim 2.4\%$ lower, while the average object-free sky-SB was 0.8% higher with the 2021 pipeline. Details are given by O’Brien et al. (2022). The 0.8% uncertainty in sky-SB induced by the different CTE-correction methods is acceptable for SKYSURF and folded into the error budget of

Table 5 for WFC3/UVIS. The 2.4% higher average sky-rms values resulting from `calwfc3` version 3.5.0 are not of immediate concern, as they are easily offset by SKYSURF’s statistics from over 40,000 WFC3/UVIS images. Both the WFC3/UVIS 2016 and 2021 CTE corrections are preserved until it can be determined which one provides more reliable total fluxes and counts of faint objects across the sky, as that is the second main goal of SKYSURF. Details on this process are given by Tompkins et al. (2022).

B.3. Identifying and Removal of HST Images with Large Artifacts and Large Targets

To get reliable panchromatic object catalogs and sky-SB measurements, SKYSURF needs to reliably identify and remove all major image artifacts. These can be due to, e.g., scattered (star) light, satellite trails, “dragon’s breath,” edge glow, stray light from (brighter) stars just outside the FOV, and image persistence or crosstalk in the ACS, WFPC2, or WFC3 images (Section 4.1). Some examples are shown in, e.g., Gosmeyer (2017) and Dauphin et al. (2022). STScI has spent considerable effort to catalog these image artifacts in WFC3, and the ACS group has done the same mostly in F606W and F814W, which are used as a starting point and for guidance to do the flagging. Anomalies have been recorded since the launches of ACS and WFC3 in 2002 and 2009, respectively, in the QL database of “Visually Noted Anomalies” (VNAs). The VNA database is available for all nonproprietary data from the WFC3 and ACS archives in MAST.

The ability of SKYSURF to accurately carry out the zodiacal foreground measurements hinges on a robust, largely automated rejection algorithm of all images with known large and bright foreground objects. These objects are often, but not always, obvious from the title of the observing program or the Object Name in the FITS header. SKYSURF uses information in the HST FITS headers and Engineering telemetry (*jit* files), through catalogs on NED and SIMBAD, and/or by visual inspection of WFPC2, ACS, and WFC3 images to flag: (a) *large* targets that HST pointed at; (b) very large random objects that overflow the ACS or WFC3 FOV; or (c) known or unknown large image defects. Examples include large Galactic objects or star-forming regions, as well as nearby NGC and RC3 galaxies with a scale length r_e large enough to overflow the FOV. Either one of these can corrupt the SKYSURF source catalogs, and often also the SKYSURF sky-SB measurements, as illustrated in the top row of Figure 7. These large targets get flagged by SKYSURF collaborators in the same stage where the large artifacts and visual anomalies are found and flagged (e.g., Figure 3 and Figure 7).

After removing the fields with large artifacts and/or large HST targets, we expect that $\sim 30\%$ of the HST FOVs that are $\gtrsim 1^\circ$ apart on the sky, or ~ 1400 independent HST fields, will be usable for independent galaxy counts in a given filter that will significantly average over cosmic variance (Sections 2.5.2, 3.2, and 4.5). Further details are given in Tompkins et al. (2022).

Appendix C SKYSURF Panchromatic Object Catalogs and Star–Galaxy Separation

In this section, we summarize SKYSURF’s methods to generate object catalogs and perform star–galaxy separation, using both the `SourceExtractor` and the `ProFound`

³³ See, e.g., Figures 1 and 2 of <https://www.stsci.edu/hst/instrumentation/wfc3/performance/cte>.

packages, as well as SKYSURF’s method to correct for Galactic extinction for both galaxies and stars.

C.1. SKYSURF Object Catalogs

Reliable object catalogs are essential for SKYSURF’s goals. Hence, SKYSURF uses two independent object-finder algorithms on the drizzled ACS/WFC and WFC3/UVIS and IR images, as illustrated in Figure 3. For the SKYSURF source-finding process, we use traditional object finder `SourceExtractor` (Bertin & Arnouts 1996) and the more recent object-finding code `ProFound` (Robotham et al. 2017) and profile-fitting code `ProFit` (Robotham et al. 2018). Both packages were designed to deblend close objects and find the optimal object total fluxes. SKYSURF compares the `ProFound` source catalogs to those from `SourceExtractor` in order to quantify which algorithm yields the most robust object total fluxes and sky-SB measurements in between the discrete objects (e.g., Figures 3, 7, and 8).

C.1.1. Object Catalogs with `SourceExtractor`

For SKYSURF source finding, we first use the traditional `SourceExtractor` algorithm (Bertin & Arnouts 1996) that the astronomical community has been using for over 25 yr, but on our newly produced SKYSURF mosaics with CR-removal over wider apertures, while the lowest estimated sky-SB from each drizzle family is left in the drizzled images. Each catalog is manually inspected for quality control, as described in Appendix B.3. Object catalogs are then passed on to the star-galaxy separation module described in Section 4.7 and Appendix C.2. Questionable catalogs are flagged for either refinement of `SourceExtractor` parameters or removal from the survey, i.e., in the case of overcrowded fields. Once the best possible catalogs are obtained with `SourceExtractor` and visually verified, star-galaxy separation is performed by examining plots of source brightness versus spatial extent (i.e., magnitude versus full width at half maximum (FWHM); see Figure 10).

C.1.2. Object Catalogs with `ProFound`

The `ProFound` (Robotham et al. 2017) source finding and `ProFit` (Robotham et al. 2018) object profile-fitting codes are used for the source-finding and source-definition aspects of SKYSURF. These packages were designed to get the most reliable image sky surface, object light profiles, and *total magnitudes* for panchromatic object counts. `ProFound` is optimized to trace the shape of the object and then dilate around this shape to some convergence limit.

C.2. SKYSURF Star–Galaxy Separation and Galactic Extinction Corrections

SKYSURF requires accurate star–galaxy separation in each field, which must be highly reliable in order to get the best possible *galaxy* counts over ~ 1400 independent HST fields covering $16 \lesssim AB \lesssim 28$ mag. SKYSURF therefore needs to do accurate star–galaxy separation on all images in each filter in an optimized way that is both automatic and highly reliable. `ProFound` can do star counts reliably in ground-based images to $AB \lesssim 20$ mag, as confirmed by Gaia (see, e.g., Koushan et al. 2021). At HST resolution, reliable star counts can be done to $AB \lesssim 25$ – 26 mag (Figures 10–11 here; see also Windhorst

et al. 2011). At total fluxes fainter than $AB \sim 25$ mag, the galaxy counts clearly dominate the star counts by a factor of $\gtrsim 100$ (Figure 11) at intermediate to high Galactic latitudes, so we do not need to aim for very accurate star–galaxy separation for the purpose of galaxy counts at $AB \simeq 25$ – 26 mag.

The panchromatic magnitudes of all SKYSURF galaxies—and hence their galaxy counts—are corrected for Galactic extinction using Schlafly & Finkbeiner (2011) as a function of $(l^{\text{II}}, b^{\text{II}})$. The panchromatic galaxy counts will likely only be reliable and be done for Galactic latitudes $|b_{\text{II}}| \gtrsim 30^\circ$, where the extinction corrections are generally accurate and relatively small. No extinction correction has been applied to the star counts in Figure 11. As the SKYSURF catalogs proceed, bright stars ($AB \lesssim 19$ mag) are verified with the Gaia DR2 catalog (Gaia Collaboration et al. 2021). Given their Gaia parallax distance from the Sun, their Galactic extinction correction thus depends on where Gaia places the star compared to the 3D Galactic dust maps of Green et al. (2019), which are based on a joint analysis that combines Pan-STARRS, 2MASS, and Gaia data. Stars fainter than those measured with Gaia ($AB \gtrsim 20$ mag) are likely much closer than the brighter Gaia stars, with typical disk scale heights of a few 100 pc (e.g., Pirzkal et al. 2009; Ryan et al. 2011, 2017), and may not need a full extinction correction, as they are likely in front of most of the Galactic dust. Further details on SKYSURF’s star–galaxy separation methods, object catalogs, and Galactic extinction corrections made are given by Carleton et al. (2022b) and Tompkins et al. (2022).

Appendix D Acronyms Used in SKYSURF

For clarity, the Table below gives a list of acronyms used in SKYSURF.

Acronym	Explanation
AB-mag	$-2.5 \log(\text{Object Flux} / \text{Zero-point Flux})$
ACS	Advanced Camera for Surveys
AGN	Active Galactic Nucleus
APT	Astronomers Proposal Tool
ASU	Arizona State University
AWS	Amazon Web Services
CCD	Charge-coupled Device
CDM	Cold Dark Matter
CERES	Clouds and the Earth’s Radiant Energy System
CIB	Cosmic Infrared Background
COB	Cosmic Optical Background
COBE	Cosmic Background Explorer
COS	HST’s Cosmic Origins Spectrograph
CR	Cosmic Ray
CTE	Charge Transfer Efficiency
CV	Cosmic Variance
CVZ	Continuous Viewing Zone
DC	(Electronic) Dark Current
DGL	Diffuse Galactic Light
DIRBE	Diffuse Infra-Red Background Experiment
EBL	Extragalactic Background Light
dEBL	diffuse Extragalactic Background Light
eEBL	extrapolated Extragalactic Background Light
iEBL	integrated Extragalactic Background Light
ERS	(HST WFC3) Early Release Science Program
FOC	HST’s Faint Object Camera
FOS	HST’s Faint Object Spectrograph
FOV	Field of View
FWHM	Full Width at Half Maximum
GDC	Geometrical Distortion Corrections
GOODS	Great Orbiting Observatories Deep Survey

(Continued)

Acronym	Explanation
H_{AB}	<i>H</i> -band (1.6 μm) AB-mag
HDF	Hubble Deep Field
HLA	Hubble Legacy Archive
HLC	Hubble Legacy Catalog
HST	Hubble Space Telescope
HUDF	Hubble UltraDeep Field
HWHM	Half Width at Half Maximum (= $0.5 \times \text{FWHM}$)
ICL	Intra-Cluster Light
IEF	Illuminated Earth Fraction
IGL	Intra-Group Light
IPD	InterPlanetary Dust
IRAF	Image Reduction and Analysis Facility
ISM	Interstellar Medium
J_{AB}	<i>J</i> -band (1.25 μm) AB-mag
Jy	Jansky or Flux Density unit (= $10^{-26} \text{W m}^{-2} \text{Hz}^{-1}$)
KBOs	Kuiper Belt Objects
LA	Earth's Limb Angle
LEO	Low Earth Orbit
LES	Lowest Estimated Sky-SB
LFS	Lowest Fitted Sky-SB
MA	Moon Angle
MAST	Mikulski Archive for Space Telescopes
NED	NASA Extragalactic Database
NEP	North Ecliptic Pole
NICMOS	Near-Infrared Camera and Multi-Object Spectrograph
OCC	Oort Cloud Comets
OTA	Optical Telescope Assembly
PAM	Pixel Area Map
PSF	Point Spread Function
QSOs	Quasi-Stellar Objects
RA	HST Roll Angle
R.A.	R.A.
RC3	Third Reference Catalog of Bright Galaxies
SAA	South Atlantic Anomaly
SA	Sun Angle
SB	Surface Brightness
SDSS	Sloan Digital Sky Survey
SED	Spectral Energy Distribution
SEP	South Ecliptic Pole
SFR	Star Formation Rate
SF	Star-forming
SM	Servicing Mission
STIS	Space Telescope Imaging Spectrograph
STScI	Space Telescope Science Institute
TD	Thermal Dark <i>Signal</i>
TNOs	Trans-Neptunian Objects
UVIS	WFC3 UV-Visual channel
UV	Ultraviolet ($\sim 0.1\text{--}0.3 \mu\text{m}$)
WFC3	HST's Wide Field Camera 3
WFPC2	HST's Wide Field Planetary Camera 2
WF/PC	HST's Wide Field/Planetary Camera
ZL	Zodiacal Light

ORCID iDs

Rogier A. Windhorst  <https://orcid.org/0000-0001-8156-6281>
 Timothy Carleton  <https://orcid.org/0000-0001-6650-2853>
 Rosalia O'Brien  <https://orcid.org/0000-0003-3351-0878>
 Seth H. Cohen  <https://orcid.org/0000-0003-3329-1337>
 Rolf Jansen  <https://orcid.org/0000-0003-1268-5230>
 Scott Tompkins  <https://orcid.org/0000-0001-9052-9837>
 Richard G. Arendt  <https://orcid.org/0000-0001-8403-8548>

Sarah Caddy  <https://orcid.org/0000-0001-6990-7792>
 Norman Grogin  <https://orcid.org/0000-0001-9440-8872>
 Anton Koekemoer  <https://orcid.org/0000-0002-6610-2048>
 John MacKenty  <https://orcid.org/0000-0001-6529-8416>
 Luke J. M. Davies  <https://orcid.org/0000-0003-3085-0922>
 Simon P. Driver  <https://orcid.org/0000-0001-9491-7327>
 Eli Dwek  <https://orcid.org/0000-0001-8033-1181>
 Alexander Kashlinsky  <https://orcid.org/0000-0003-2156-078X>
 Scott J. Kenyon  <https://orcid.org/0000-0003-0214-609X>
 Nathan Miles  <https://orcid.org/0000-0001-8936-4545>
 Nor Pirzkal  <https://orcid.org/0000-0003-3382-5941>
 Aaron Robotham  <https://orcid.org/0000-0003-0429-3579>
 Russell Ryan  <https://orcid.org/0000-0003-0894-1588>
 Jessica Berkheimer  <https://orcid.org/0000-0001-6265-0541>
 Isabela Huckabee  <https://orcid.org/0000-0002-4031-6400>
 Darby Kramer  <https://orcid.org/0000-0003-0238-8806>
 Teerthal Patel  <https://orcid.org/0000-0003-0057-7603>
 Kaitlin Webber  <https://orcid.org/0000-0002-9762-4308>

References

- Alexander, D. M., Bauer, F. E., Chapman, S. C., et al. 2005, *ApJ*, **632**, 736
 Anand, G., Grogin, N., & Anderson, J. 2022, Revisiting ACS/WFC Sky Backgrounds, Instrument Science Report ACS 2022-1
 Anderson, J., Baggett, S., & Kuhn, B. 2021, Updating the WFC3/UVIS CTE model and Mitigation Strategies, Space Telescope WFC Instrument Science Report
 Anderson, J., & Bedin, L. R. 2010, *PASP*, **122**, 1035
 Andrews, S. K., Driver, S. P., Davies, L. J. M., et al. 2017, *MNRAS*, **464**, 1569
 Andrews, S. K., Driver, S. P., Davies, L. J. M., Lagos, C. d. P., & Robotham, A. S. G. 2018, *MNRAS*, **474**, 898
 Ashby, M. L. N., Willner, S. P., Fazio, G. G., et al. 2015, *ApJS*, **218**, 33
 Astropy Collaboration, Price-Whelan, A. M., Sipőcz, B. M., et al. 2018, *AJ*, **156**, 123
 Astropy Collaboration, Robitaille, T. P., Tollerud, E. J., et al. 2013, *A&A*, **558**, A33
 Avila, R. J., Hack, W., Cara, M., et al. 2015, in ASP Conf. Ser. 495, *Astronomical Data Analysis Software and Systems XXIV (ADASS XXIV)*, ed. A. R. Taylor & E. Rosolowsky (San Francisco, CA: ASP), 281
 Bajaj, V. 2019, WFC3/IR Photometric Repeatability, Space Telescope WFC Instrument Science Report 2019-07
 Beckwith, S. V. W., Stiavelli, M., Koekemoer, A. M., et al. 2006, *AJ*, **132**, 1729
 Bernstein, R. A. 2007, *ApJ*, **666**, 663
 Bernstein, R. A., Freedman, W. L., & Madore, B. F. 2002, *ApJ*, **571**, 56
 Berta, S., Magnelli, B., Nordon, R., et al. 2011, *A&A*, **532**, A49
 Bertin, E., & Arnouts, S. 1996, *A&AS*, **117**, 393
 Béthermin, M., Le Floc'h, E., Ilbert, O., et al. 2012, *A&A*, **542**, A58
 Biretta, J. 2009, *WFPC2 Handbook v9.2* (Baltimore, MA: STScI)
 Biretta, J., & Baggett, S. 2013, WFC3 Post-Flash Calibration, Space Telescope WFC Instrument Science Report
 Biretta, J., Ritchie, C., & Rudloff, K. 1995, A Field Guide to WFPC2 Image Anomalies, Space Telescope WFPC2 Instrument Science Report
 Biteau, J., & Williams, D. A. 2015, *ApJ*, **812**, 60
 Bohlin, R. C., Ryon, J. E., & Anderson, J. 2020, Update of the Photometric Calibration of the ACS CCD Cameras, Instrument Science Report ACS 2020-8
 Borlaff, A., Trujillo, I., Román, J., et al. 2019, *A&A*, **621**, A133
 Bradley, L., Sipőcz, B., Robitaille, T., et al. 2020, *astropy/photutils*: 1.0.0, Zenodo, doi:[10.5281/zenodo.4044744](https://doi.org/10.5281/zenodo.4044744)
 Brammer, G. 2016, Reprocessing WFC3/IR Exposures Affected by Time-Varying Backgrounds, Space Telescope WFC Instrument Science Report 2016-16
 Brammer, G., Pirzkal, N., McCullough, P., & MacKenty, J. 2014, Time-varying Excess Earth-glow Backgrounds in the WFC3/IR Channel, Space Telescope WFC Instrument Science Report 2014-03
 Brammer, G., Ryan, R., & Pirzkal, N. 2015, Source-dependent Master Sky Images for the WFC3/IR Grisms, Space Telescope WFC Instrument Science Report 2015-17
 Budavári, T., & Lubow, S. H. 2012, *ApJ*, **761**, 188

- Bushouse, H. 2008, WFC3 IR Ground P-Flats, Space Telescope WFC Instrument Science Report
- Caddy, S., & Spitler, L. 2021, in 43rd COSPAR Scientific Assembly (Washington, DC: NASA), 1534
- Caddy, S. E., Spitler, L. R., & Ellis, S. C. 2022, *AJ*, **164**, 52
- Calamida, A., Mack, J., Medina, J., et al. 2021, New time-dependent WFC3 UVIS inverse sensitivities, Space Telescope WFC Instrument Science Report
- Cambrésy, L., Reach, W. T., Beichman, C. A., & Jarrett, T. H. 2001, *ApJ*, **555**, 563
- Carleton, T., Windhorst, R. A., MacKenty, J. W., et al. 2022b, in preparation
- Carleton, T., Windhorst, R. A., O'Brien, R., et al. 2022a, arXiv:2205.06347
- Carter, D., Carleton, T., Koekemoer, A., et al. 2022, in preparation
- Casertano, S., de Mello, D., Dickinson, M., et al. 2000, *AJ*, **120**, 2747
- Cohen, Y., Grogin, N. A., & Bellini, A. 2020, Post-SM4 ACS/WFC L-Flats and Photometric Errors from Observations of Stellar Fields, Instrument Science Report ACS 2020-1
- Cowley, W. I., Lacey, C. G., Baugh, C. M., et al. 2019, *MNRAS*, **487**, 3082
- Dauphin, F., Montes, M., Easmin, N., Bajaj, V., & McCullough, P. R. 2022, WFC3/UVIS Figure-8 Ghost Classification using Convolutional Neural Networks, Instrument Science Report WFC3 2022-3, 41
- Davies, L. J. M., Driver, S. P., Robotham, A. S. G., et al. 2015, *MNRAS*, **447**, 1014
- Desai, A., Helgason, K., Ajello, M., et al. 2019, *ApJL*, **874**, L7
- Deustua, S., Long, K. S., McCullough, P., et al. 2010, *Proc. SPIE*, **7731**, 77313C
- Deustua, S. E., Mack, J., Bowers, A. S., et al. 2016, UVIS 2.0 Chip-dependent Inverse Sensitivity Values, Space Telescope WFC Instrument Science Report
- Dole, H., Lagache, G., Puget, J. L., et al. 2006, *A&A*, **451**, 417
- Domínguez, A., Primack, J. R., Rosario, D. J., et al. 2011, *MNRAS*, **410**, 2556
- Dressel, L. 2012, Wide Field Camera 3 Instrument Handbook, Version 5.0 (Baltimore, MA: STScI)
- Dressel, L. 2016, Wide Field Camera 3 Instrument Handbook, Version 8.0 (Baltimore, MA: STScI)
- Dressel, L. 2021, Wide Field Camera 3 Instrument Handbook, Version 13.0 (Baltimore, MA: STScI)
- Driver, S. P., Andrews, S. K., Davies, L. J., et al. 2016a, *ApJ*, **827**, 108
- Driver, S. P., Hill, D. T., Kelvin, L. S., et al. 2011, *MNRAS*, **413**, 971
- Driver, S. P., & Robotham, A. S. G. 2010, *MNRAS*, **407**, 2131
- Driver, S. P., Windhorst, R. A., Ostrander, E. J., et al. 1995, *ApJL*, **449**, L23
- Driver, S. P., Wright, A. H., Andrews, S. K., et al. 2016b, *MNRAS*, **455**, 3911
- Dwek, E., & Arendt, R. G. 1998, *ApJL*, **508**, L9
- Dwek, E., Arendt, R. G., Hauser, M. G., et al. 1998, *ApJ*, **508**, 106
- Dwek, E., & Krennrich, F. 2013, *Aph*, **43**, 112
- Fermi-LAT Collaboration, Abdollahi, S., Ackermann, M., et al. 2018, *Sci*, **362**, 1031
- Finke, J. D., Razzaque, S., & Dermer, C. D. 2010, *ApJ*, **712**, 238
- Fixsen, D. J., Dwek, E., Mather, J. C., Bennett, C. L., & Shafer, R. A. 1998, *ApJ*, **508**, 123
- Fruchter, A. S., & Hook, R. N. 2002, *PASP*, **114**, 144
- Gaia Collaboration, Brown, A. G. A., Vallenari, A., et al. 2021, *A&A*, **649**, A1
- Giavalisico, M., Ferguson, H. C., Koekemoer, A. M., et al. 2004, *ApJL*, **600**, L93
- Goisman, Z., Carleton, T., & Cohen, S. H. 2022, in preparation
- Gonzaga, S., & Biretta, J. 2010, WFC3 Handbook v5.0 (Baltimore, MA: STScI)
- Gosmeyer, C. M. 2017, WFC3 Anomalies Flagged by the Quicklook Team, Instrument Science Report WFC3 2017-22
- Greco, J. P., Greene, J. E., Strauss, M. A., et al. 2018, *ApJ*, **857**, 104
- Green, G. M., Schlafly, E., Zucker, C., Speagle, J. S., & Finkbeiner, D. 2019, *ApJ*, **887**, 93
- Grogin, N. A., Kocevski, D. D., Faber, S. M., et al. 2011, *ApJS*, **197**, 35
- Hathi, N. P., Ryan, R. E. J., Cohen, S. H., et al. 2010, *ApJ*, **720**, 1708
- Hauser, M. G., Arendt, R. G., Kelsall, T., et al. 1998, *ApJ*, **508**, 25
- Hauser, M. G., & Dwek, E. 2001, *ARA&A*, **39**, 249
- HAWC Collaboration 2022, arXiv:2204.12166
- H.E.S.S. Collaboration, Abramowski, A., Acero, F., et al. 2013, *A&A*, **550**, A4
- Holtzman, J. A., Burrows, C. J., Casertano, S., et al. 1995, *PASP*, **107**, 1065
- Hopkins, A. M., Driver, S. P., Brough, S., et al. 2013, *MNRAS*, **430**, 2047
- Hopwood, R., Serjeant, S., Negrello, M., et al. 2010, *ApJL*, **716**, L45
- Ilbert, O., Tresse, L., Zucca, E., et al. 2005, *A&A*, **439**, 863
- Jauzac, M., Dole, H., Le Floc'h, E., et al. 2011, *A&A*, **525**, A52
- Kalirai, J. S., Baggett, S., Borders, T., & Rajan, A. 2010, The Photometric Performance of WFC3/UVIS: Temporal Stability Through Year 1, Space Telescope WFC Instrument Science Report 2010-14
- Kashlinsky, A. 2005, *PhR*, **409**, 361
- Kashlinsky, A., & Odenwald, S. 2000, *ApJ*, **528**, 74
- Kawara, K., Matsuoka, Y., Sano, K., et al. 2017, *PASJ*, **69**, 31
- Keenan, R. C., Barger, A. J., Cowie, L. L., & Wang, W. H. 2010, *ApJ*, **723**, 40
- Kelsall, T., Weiland, J. L., Franz, B. A., et al. 1998, *ApJ*, **508**, 44
- Khaire, V., & Srianand, R. 2015, *ApJ*, **805**, 33
- Koekemoer, A. M., Ellis, R. S., McLure, R. J., et al. 2013, *ApJS*, **209**, 3
- Koekemoer, A. M., Faber, S. M., Ferguson, H. C., et al. 2011, *ApJS*, **197**, 36
- Kornut, P. M., Kim, M. G., Arai, T., et al. 2022, *ApJ*, **926**, 133
- Koushan, S., Driver, S. P., Bellstedt, S., et al. 2021, *MNRAS*, **503**, 2033
- Kramer, D. M., Carleton, T., Cohen, S. H., et al. 2022, arXiv:2208.07218
- Lagache, G., Abergel, A., Boulanger, F., Désert, F. X., & Puget, J. L. 1999, *A&A*, **344**, 322
- Lagache, G., Puget, J.-L., & Dole, H. 2005, *ARA&A*, **43**, 727
- Landsman, W. B. 1993, in ASP Conf. Ser. 52, Astronomical Data Analysis Software and Systems II, ed. R. J. Hanisch, R. J. V. Brissenden, & J. Barnes (San Francisco, CA: ASP), 246
- Lauer, T. R. 1999, *PASP*, **111**, 227
- Lauer, T. R., Postman, M., Spencer, J. R., et al. 2022, *ApJL*, **927**, L8
- Lauer, T. R., Postman, M., Weaver, H. A., et al. 2021, *ApJ*, **906**, 77
- Leinert, C., Bowyer, S., Haikala, L. K., et al. 1998, *A&AS*, **127**, 1
- Liske, J., Baldry, I. K., Driver, S. P., et al. 2015, *MNRAS*, **452**, 2087
- Long, K. S., Baggett, S., Deustua, S., & Riess, A. 2010, WFC3/IR Persistence as Measured in Cycle 17 using Tungsten Lamp Exposures, Space Telescope WFC Instrument Science Report 2010-17
- Long, K. S., Baggett, S. M., MacKenty, J. W., & Riess, A. G. 2012, *Proc. SPIE*, **8442**, 84421W
- Lorentz, M., Brun, P., & Sanchez, D. 2015, in Proceedings of the 34th International Cosmic Ray Conference (ICRC2015) (Trieste: SISSA), 777
- Mack, J., Olszewski, H., & Pirzkal, N. 2021, WFC3/IR Filter-Dependent Sky Flats, Space Telescope WFC Instrument Science Report
- Mack, J., Rajan, A., & Bowers, A. 2015, Spatial Accuracy of the UVIS Flat Fields, Instrument Science Report WFC3 2015-18
- Madau, P., & Dickinson, M. 2014, *ARA&A*, **52**, 415
- Madau, P., & Pozzetti, L. 2000, *MNRAS*, **312**, L9
- Magnelli, B., Popesso, P., Berta, S., et al. 2013, *A&A*, **553**, A132
- Matsumoto, T., Matsuura, S., Murakami, H., et al. 2005, *ApJ*, **626**, 31
- Matsumoto, T., Seo, H. J., Jeong, W. S., et al. 2011, *ApJ*, **742**, 124
- Matsuura, S., Arai, T., Bock, J. J., et al. 2017, *ApJ*, **839**, 7
- Matsuura, S., Shirahata, M., Kawada, M., et al. 2011, *ApJ*, **737**, 2
- Mattila, K. 2006, *MNRAS*, **372**, 1253
- Mattila, K., Väisänen, P., Lehtinen, K., von Appen-Schnur, G., & Leinert, C. 2017, *MNRAS*, **470**, 2152
- McMaster, M., & Whitmore, B. 2002, Updated Contamination Rates for WFC2 UV Filters, Space Telescope WFC2 Instrument Science Report
- McVittie, G. C., & Wyatt, S. P. 1959, *ApJ*, **130**, 1
- Medina, J., Mack, J., & Calamida, A. 2022, WFC3/UVIS Encircled Energy, Instrument Science Report WFC3 2022-2
- Miles, N. D., Deustua, S., & Tancredi, G. 2020, HSTCosmicrays: Analyzing Cosmic Rays in HST Calibration Data, Astrophysics Source Code Library, ascl:2011.021
- Miles, N. D., Lim, P.-L., Bellini, A., & Grogin, N. A. 2018, Updates to the CALACS Cosmic Ray Rejection Routine: ACSREJ, Instrument Science Report ACS 2018-05
- Moster, B. P., Somerville, R. S., Newman, J. A., & Rix, H.-W. 2011, *ApJ*, **731**, 113
- O'Brien, R., Carleton, T., & Windhorst, R. A. 2022, in preparation
- Odehahn, S. C., Burstein, D., & Windhorst, R. A. 1997, *AJ*, **114**, 2219
- Odehahn, S. C., Windhorst, R. A., Driver, S. P., & Keel, W. C. 1996, *ApJL*, **472**, L13
- Oke, J. B., & Gunn, J. E. 1983, *ApJ*, **266**, 713
- Olszewski, H., & Mack, J. 2021, WFC3/IR Blob Flats, Space Telescope WFC Instrument Science Report
- Partridge, R. B., & Peebles, P. J. E. 1967a, *ApJ*, **147**, 868
- Partridge, R. B., & Peebles, P. J. E. 1967b, *ApJ*, **148**, 377
- Pirzkal, N. 2014, ISR WFC3 2014-11 (STScI), Space Telescope WFC3 Instrument Science Report
- Pirzkal, N., Burgasser, A. J., Malhotra, S., et al. 2009, *ApJ*, **695**, 1591
- Pirzkal, N., Mack, J., Dahlen, T., & Sabbi, E. 2011, Sky Flats: Generating Improved WFC3 IR Flat-fields, Space Telescope WFC Instrument Science Report
- Pirzkal, N., & Ryan, R. 2020, The Dispersed infrared background in WFC3 G102 and G141 observations, Space Telescope WFC Instrument Science Report
- Pirzkal, N., Viana, A., & Rajan, A. 2010, The WFC3 IR 'Blobs', Space Telescope WFC Instrument Science Report

- Planck Collaboration, Ade, P. A. R., Aghanim, N., et al. 2016, *A&A*, **594**, A13
- Puget, J. L., Abergel, A., Bernard, J. P., et al. 1996, *A&A*, **308**, L5
- Rafelski, M., Teplitz, H. I., Gardner, J. P., et al. 2015, *AJ*, **150**, 31
- Rajan, A., & Baggett, S. 2010, WFC3 SMOV Proposal 11432: UVIS Internal Flats, Space Telescope WFC Instrument Science Report
- Riess, A. G. 2010, First On-orbit Measurements of the WFC3-IR Count-rate Non-Linearity, Space Telescope WFC Instrument Science Report
- Riess, A. G., Narayan, G., & Calamida, A. 2019, Calibration of the WFC3-IR Count-rate Nonlinearity, Sub-percent Accuracy for a Factor of a Million in Flux, Space Telescope WFC Instrument Science Report
- Robotham, A. S. G., Davies, L. J. M., Driver, S. P., et al. 2018, *MNRAS*, **476**, 3137
- Robotham, A. S. G., Taranu, D. S., Tobar, R., Moffett, A., & Driver, S. P. 2017, *MNRAS*, **466**, 1513
- Ryan, R. E., Thorman, P. A., Yan, H., et al. 2011, *ApJ*, **739**, 83
- Ryan, R. E. J., Deustua, S., Sosey, M., et al. 2016, The Updated Calibration Pipeline for WFC3/UVIS: a Reference Guide to calwf3 (version 3.3), Space Telescope WFC Instrument Science Report 2016-01
- Ryan, R. E. J., Thorman, P. A., Schmidt, S. J., et al. 2017, *ApJ*, **847**, 53
- Ryon, J. E. 2022, ACS Instrument Handbook (Baltimore, MA: STScI)
- Saldana-Lopez, A., Domínguez, A., Pérez-González, P. G., et al. 2021, *MNRAS*, **507**, 5144
- Sano, K., Matsuura, S., Yomo, K., & Takahashi, A. 2020, *ApJ*, **901**, 112
- Schlafly, E. F., & Finkbeiner, D. P. 2011, *ApJ*, **737**, 103
- Skelton, R. E., Whitaker, K. E., Momcheva, I. G., et al. 2014, *ApJS*, **214**, 24
- Smith, B. M., Windhorst, R. A., Cohen, S. H., et al. 2020, *ApJ*, **897**, 41
- Smith, B. M., Windhorst, R. A., Jansen, R. A., et al. 2018, *ApJ*, **853**, 191
- Smith, R. W., Hanle, P. A., Kargon, R. H., & Tatarewicz, J. N. 1993, The Space Telescope. A study of NASA, science, technology, and politics
- Somerville, R. S., Lee, K., Ferguson, H. C., et al. 2004, *ApJL*, **600**, L171
- Suchkov, A., & Baggett, S. 2012, WFC3/UVIS Crosstalk and Crosstalk Correction, Space Telescope WFC Instrument Science Report 2012-02
- Sunnquist, B., Baggett, S., & Long, K. S. 2017a, An Exploration of WFC3/IR Dark Current Variation, Space Telescope WFC Instrument Science Report 2017-04
- Sunnquist, B., Baggett, S., & Long, K. S. 2017b, A Predictive WFC3/IR Dark Current Model, Space Telescope WFC Instrument Science Report 2017-24
- Sunnquist, B., McKay, M., & Baggett, S. 2019, Time-dependent WFC3/IR Superdarks, Space Telescope WFC Instrument Science Report 2019-04
- Teplitz, H. I., Rafelski, M., Kurczynski, P., et al. 2013, *AJ*, **146**, 159
- Tompkins, S., Driver, S. P., Windhorst, R. A., et al. 2022, in preparation
- Totani, T., Yoshii, Y., Iwamuro, F., Maihara, T., & Motohara, K. 2001, *ApJL*, **550**, L137
- Trenti, M., & Stiavelli, M. 2008, *ApJ*, **676**, 767
- Tsumura, K., Matsumoto, T., Matsuura, S., Sakon, I., & Wada, T. 2013, *PASJ*, **65**, 121
- Vaiana, A. C., & Baggett, S. 2010, WFC3 TV3 Testing: IR Crosstalk, Space Telescope WFC Instrument Science Report 2010-02
- van der Wel, A., Bell, E. F., Häussler, B., et al. 2012, *ApJS*, **203**, 24
- van Dokkum, P. G. 2001, *PASP*, **113**, 1420
- Whitmore, B. C., Allam, S. S., Budavári, T., et al. 2016, *AJ*, **151**, 134
- Wielicki, B. A., Barkstrom, B. R., Harrison, E. F., et al. 1996, *BAMS*, **77**, 853
- Williams, R. E., Blacker, B., Dickinson, M., et al. 1996, *AJ*, **112**, 1335
- Windhorst, R., Mathis, D. F., & Keel, W. C. 1992, *ApJL*, **400**, L1
- Windhorst, R. A., Carleton, T., Cohen, S. H., et al. 2021, arXiv:2106.02664
- Windhorst, R. A., Cohen, S. H., Hathi, N. P., et al. 2011, *ApJS*, **193**, 27
- Windhorst, R. A., Franklin, B. E., & Neuschaefer, L. W. 1994a, *PASP*, **106**, 798
- Windhorst, R. A., Hathi, N. P., Cohen, S. H., et al. 2008, *AdSpR*, **41**, 1965
- Windhorst, R. A., Keel, W. C., & Pascarella, S. M. 1998, *ApJL*, **494**, L27
- Windhorst, R. A., Schmidtke, P. C., Pascarella, S. M., et al. 1994b, *AJ*, **107**, 930
- Windhorst, R. A., Timmes, F. X., Wyithe, J. S. B., et al. 2018, *ApJS*, **234**, 41
- Wright, E. L. 1998, *ApJ*, **496**, 1
- Xu, C. K., Donas, J., Arnouts, S., et al. 2005, *ApJL*, **619**, L11
- York, D. G., Adelman, J., Anderson, J. E. J., et al. 2000, *AJ*, **120**, 1579
- Zaritsky, D., Donnerstein, R., Dey, A., et al. 2019, *ApJS*, **240**, 1
- Zemcov, M., Immel, P., Nguyen, C., et al. 2017, *NatCo*, **8**, 15003